Three-dimensional reconstruction of intragranular strain and orientation in polycrystals by near-field X-ray diffraction

Péter Reischig, Wolfgang Ludwig

Link to formal publication:

Péter Reischig, Wolfgang Ludwig
Three-dimensional reconstruction of intragranular strain and orientation in polycrystals by near-field X-ray diffraction
Current Opinion in Solid State and Materials Science, Volume 24, Issue 5, 2020, 100851, ISSN 1359-0286

https://doi.org/10.1016/j.cossms.2020.100851
(http://www.sciencedirect.com/science/article/pii/S1359028620300498)

Submitted 19 February 2020, Revised 27 July 2020, Accepted 31 July 2020, Available online 6 October 2020.

Three-dimensional reconstruction of intragranular strain and orientation in polycrystals by near-field X-ray diffraction

Péter Reischig[a,b,d], Wolfgang Ludwig[c,a,*]

[a] *European Synchrotron Radiation Facility (71, avenue des Martyrs, CS 40220, 38043 Grenoble CEDEX 9, France)*
[b] *InnoCryst Ltd (CTH, Daresbury Laboratory, Sci-Tech Daresbury, Keckwick Lane, Daresbury, Warrington, WA4 4AD, United Kingdom)*
[c] *Laboratoire Materiaux, Ingenierie et Science, INSA Lyon, Universite de Lyon (92, rue Pasteur, CS 30122, 69361 Lyon Cedex 07, France)*
[d] *Karlsruhe Institute of Technology, Institute for Photon Science and Synchrotron Radiation, Hermann-v.-Helmholtz-Platz 1, 76344 Eggenstein-Leopoldshafen, Germany*

Abstract

A theoretical framework is proposed for simultaneous reconstruction of the three-dimensional grain shapes, intragranular strain and orientation fields inside polycrystals from near-field X-ray diffraction images, using box beam illumination. The approach, named Iterative Tensor Field (ITF) reconstruction, uses a tensor field representation and a kinematical forward simulation model to reproduce the measured diffraction signal from individual grains. The framework establishes a link between the local deformation components inside the grains and the intensities of the diffraction signal in the measured images by forming a local linear problem. This is solved using a large scale linear optimisation method in every main iteration of the underlying non-linear problem. The optimisation enforces smooth gradients and the objective function may include regularisation constraints of static equilibrium or input from a Crystal Plasticity FEM simulation. The method has modest computational requirements and enables efficient scanning of millimetre or sub-millimetre sized specimens. Results on experimental data measured on a Gum metal specimen are presented, which demonstrate convergence and the feasibility of the approach. The mathematical formulation, data representation and challenges in the reconstruction and validation are discussed. The physical aspects of the contrast phenomenon, the deformation sensitivity of the technique, and potential means of error assessment are described. A number of alternative concepts for a polycrystalline deformation model and potential solvers are also presented.

1. Introduction

1.1. Relevance of mesoscale characterisation of polycrystals

In order to gain a better understanding of the multiscale processes involved in the plastic deformation and failure of polycrystalline structural materials, a variety of advanced experimental characterisation tools, primarily electron and X-ray microscopy, are deployed. These experimental observations are then often coupled to modelling efforts (dislocation dynamics, crystal plasticity) carried out on realistic microstructure instantiations, for a recent detailed review see (Shade et al.,2019)[1] and references therein. As pointed out by Sangid (Sangid, 2019)[2], the comparison

*Corresponding author
Email address: ludwig@esrf.fr (Wolfgang Ludwig)

between experiment and simulation using emerging machine learning and optimisation techniques offer powerful leverage for improving materials models and can be expected to advance our capabilities for predictive modelling of this kind of processes.

The mesoscale is of high relevance when studying the effects of crystallography, grain interactions and grain boundaries on elasticity, plasticity, damage initiation, propagation, and phase transformations. Our experimental focus is on the scale of millimetre to sub-millimetre sized polycrystalline specimens consisting of 100s or 1000s of grains. This is a length scale which delivers a wealth of information and unites a series of advantages: (1) the investigated microstructures - typically tens of grains across the specimen width - are representative for bulk behaviour and exhibit grain to grain interactions; (2) micromechanical experiments with well controlled macroscopic loading conditions are fairly easily implemented; (3) X-rays have the capability to provide high-resolution non-destructive crystallographic information of the bulk; (4) Crystal Plasticity FEM simulations are well adapted to this scale. Therefore, it is an outstanding opportunity to directly compare in-situ experimental data with simulations on a fully detailed three-dimensional mechanical model, i.e. a "digital twin" of the real specimen. For a complete mechanical model, highly detailed three-dimensional information on the crystal phases, crystal boundaries, local crystal orientations and the full local strain tensors are required.

1.2. 3D strain mapping methods

The experimental determination of local strains (and stresses derived thereof) can be divided into the following categories, reflecting the length scale and resolution of the measurement with respect to the grain size. While the rest of the article describes new opportunities for intragranular strain retrieval, in this overview we cover recent advances in experimental and theoretical abilities to characterise the deformation state, i.e. the orientation and strain distributions, of the crystalline lattice in 3D in the bulk of polycrystalline materials by means of synchrotron X-ray diffraction techniques. As more sophisticated tools are being developed, mapping grain structures in 3D via X-ray diffraction has been providing data sets with increasingly rich information content. While diffraction is sensitive to the actual elastic strain state of the crystal lattice, digital image correlation can track the overall (elastic and plastic) deformation between two or more measured states at various scales when suitable markers are present within the material (Maire & Withers, 2014; Sutton & Hild, 2015; Mao, 2019)[3, 4, 5].

1.2.1. Ensemble average strain (Type I stresses)

In a far-field powder diffraction type experiment (using monochromatic X-rays or neutrons) the detector is far from the sample (e.g. 50mm+) and the pixel size is much larger than the average grain size. Debye-Scherrer rings are formed on the detector from a quasi-infinite number of grains of the polycrystal that diffract simultaneously, like a powder. These rings provide the basis of the analysis, and the information in the large number of pixels that constitute a ring in a single image is reduced to a few geometric parameters in a pre-processing step before the structure or strain (Type I stress) analysis. The rings change smoothly and are only very slightly sensitive to fine rotations (e.g. 0.1°) of the sample, during which the actual grains and sub-regions of grains, that happen to be in the diffraction condition for the wavelength of the incident beam, change. The

macroscopic strain is equivalent to an average stretch of the lattice perpendicular to a diffracting lattice plane, which manifests itself in a change of Bragg angle and hence a change in the local effective radius (or radial moment of intensities) of the Debye-Scherrer rings.

In the field of classical strain scanning, a location in the specimen is measured directly and controlled by apertures. It is often carried out at the component scale with macroscopic sampling volumes (Withers & Webster, 2001) (Staron et al., 2017)[6, 7]. In a more recent approach, and where the sample geometry allows, utilising 2D area detectors and a pencil beam, the diffraction signal is processed (data reduction) and the information is localised via a scanning and reconstruction procedure, following established principles of computed tomography (Álvarez-Murga et al., 2012)[8]. We note that both techniques can also utilise neutrons, with the added capability of Bragg edge imaging (Lionheart & Withers, 2015) (Hendriks et al., 2019) (Gregg et al., 2020) [9, 10, 11].

1.2.2. Grain average strain (Type II stresses)

Grain average strain tensors can be obtained by recording reflections from individual grains, i.e. diffraction spots or peaks, instead of the Debye-Scherrer rings. The far-field (detector pixel size 50...200μm) grain tracking methods are known as 3D X-Ray Diffraction (3DXRD) (Lauridsen et al., 2001) (Henning Friis Poulsen, 2004) (Schmidt et al., 2011) (Sørensen et al., 2012) (Sharma et al., 2012) (Jensen & Poulsen, 2012) (Schmidt, 2014)[12, 13, 14, 15, 16, 17] or High Energy Diffraction Microscopy (HEDM) (Shade et al., 2019)(Lienert et al., 2011) (Bernier et al., 2011) (Barton & Bernier, 2012) [1, 18, 19, 20]. After considerable initial efforts to achieve hardware stability, distortion correction, reliable indexing and geometry calibration via software, grain average strain measurements on 100s or 1000s of grains became standard in far-field at strain resolutions of 10^{-4} and beyond (Paciorek et al., 1999) (H. F. Poulsen et al., 2001) (Oddershede et al., 2010) (Bernier et al., 2011; Edmiston et al., 2011, 2012) (Borbely et al., 2014) (Sedmák et al., 2016)[21, 22, 23, 19, 24, 25, 26, 27]. Determination of grain average strains from near-field diffraction data obtained with DCT has been demonstrated (Reischig, 2008) (Reischig et al., 2013) (Proudhon et al., 2016) (Reischig & Ludwig, 2019) [28, 29, 30, 31] and can achieve a strain resolution of a few times 10^{-4}.

1.2.3. Intragranular strain (Type III stresses)

A robust, although time-consuming, technique for the local measurement of intra-granular strains in the bulk at micrometre spatial and 10^{-4} strain accuracy is Differential Aperture X-ray Microscopy (DAXM) (Larson et al., 2002; Levine et al., 2006; Robach et al., 2013; Tardif et al., 2016)[32, 33, 34, 35], a variant of polychromatic X-ray Laue micro-diffraction. More recently, using monochromatic micro-beam scanning, a far-field detector and an established 3DXRD indexing procedure (ImageD11) (Wright, 2017)[36], Hektor et al. has shown local sensitivity of the method to hydrostatic strain (Hektor et al., 2019)[37], and Hayashi et al. has demonstrated mapping the full strain tensor over a region containing 37^3 voxels at 1.2 μm spacing deep inside a steel specimen (Hayashi et al., 2019)[38].

Dark Field X-ray Microscopy focuses on a single reflection of an embedded grain and uses compound refractive lenses to achieve 100...200nm spatial, 0.001rad orientation and 10^{-5} strain resolution along that scattering vector (H. Simons et al., 2015; H. F. Poulsen et al., 2017; Hugh

Simons et al., 2018)[39, 40, 41]. Combining more than one (hkl) reflection on the current setup at ID06, ESRF is problematic due to the lengthy scanning time and limitations of the sample goniometer.

Operating at a spatial resolution of tens of nanometres, and focusing on an individual crystal, nanoscanning and coherent X-ray diffraction techniques (Coherent Bragg Diffraction Imaging, CBDI) are capable of mapping the strain component along a scattering vector in single crystals (see (Schulli & Leake, 2018)[42] for a recent review). Mapping several reflections in an isolated nano-crystal (Newton et al., 2010)[43] or in embedded grains (Cherukara et al., 2018)[44] enables quantification of the full strain tensor and has recently been used to characterise the full 3D strain tensor field around individual dislocations (Hofmann et al., 2020)[45].

1.2.4. Intragranular misorientation

All techniques mentioned in Section 1.2.3 use a far-field detector and intrinsically provide access to intragranular misorientation fields. Intragranular misorientation can also be characterised using a near-field setup. A variety of reconstruction techniques have been proposed to extract local orientation from line and box-beam near-field diffraction signal (see Poulsen, 2012)[46]. Forward modelling based approaches typically employ line beam illumination and naturally include subgrain misorientations in a 2D section of the specimen (Suter et al., 2006; S. F. Li & Suter, 2013; Renversade et al., 2016; Menasche et al., 2020)[47, 48, 49, 50]. High quality 3D volumes with a spatial resolution down to one micrometre and an orientation resolution within 0.1° can be constructed by scanning and stacking multiple 2D sections.

Extended beam (box beam) acquisition techniques complement the existing portfolio of X-ray orientation microscopy techniques. For instance, DCT can account for and resolve a misorientation distribution within the grains using a "6D solver", still preceded by an indexing step (see Section 1.3 for further details, and Fig. 21 for an overview of data representation). "6D" stands for the combined representation of three real space and three orientation space dimensions, and it has been demonstrated to provide accurate grain maps with micrometre resolution when the mosaicity of the crystal lattice is moderate (Poulsen, 2003; Nicola Viganò et al., 2014; Nicola Viganò, Tanguy, et al., 2016; N. Viganò & Ludwig, 2018)[51, 52, 53, 54, 55].

1.3. Representation of 3D deformation fields in polycrystals

The local deformation of the crystal lattice in the most simple case is described by a 9-component deformation tensor, or three (mis)orientation and six strain parameters over all (x,y,z) locations within the sample (see Appendix). Complementing it with a scalar that represents the local diffracting power, this $\mathcal{F}(x, y, z) : \mathbb{R}^3 \mapsto \mathbb{R}^{1+9}$ 10-component tensor field constitutes the ultimate information which can reasonably be extracted from the typical grain resolved 3D polycrystal diffraction methods under consideration. For deformations at a smaller scale and using a suitably narrow energy bandwidth ($dE/E < 10^{-4}$), rocking curve imaging techniques apply [56, 57].

As intragranular misorientation and strain can be treated as small local deviations from a mean, in a more intricate model, a distribution of small deformations at each location may be considered. The kind of diffraction data at hand does not contain enough information to uniquely resolve random distributions at this level of detail, however, sparse distributions (i.e. voxel average

orientations) can be reliably inferred. With full beam illumination, the complete solution space for misorientations only, without strain, is a six-dimensional space, the outer product of 3D real space and 3D orientation space. Such a representation was described by Poulsen (H. F. Poulsen, 2003)[51], and a grain-by-grain solver, named a "6D solver" was demonstrated by Viganò et al. using simulated (Viganò N. et al., 2014)[52] and real data sets (Viganò N., Nervo, et al., 2016; Nicola Viganò, Tanguy, et al., 2016)[53, 54]. The main advantage of discretising deformation space is that the multidimensional reconstruction can be formulated as a linear problem in a rigorous mathematical framework. In this framework, each pixel of the obtained image stack represents one linear equation, and the pixel intensity is the sum of the contributions from those elements of the six-dimensional space that project into the pixel. As in this model the projection directions are fixed, the projection contributions can be expressed as one large constant matrix, the "A matrix". The diffracting power of the elements are the unknown parameters sought, and a sparse solution can be found with established iterative schemes. An extension to include the extra six dimensions of strain would quickly render the solution space enormous and the framework impractical (Fig. 21).

Instead, as a feasible alternative, a vector representation uses a tensor field throughout the solution process that assigns nine deformation components to a location within the grain represented by a finite voxel element over a regular grid. The amount of data storage required for a medium sized grain is in the megabyte range, and a highly-detailed deformation map of a complete sample volume still easily fits in the RAM of a high-end desktop computer. However, the vector representation results in a non-linear problem with less obvious solution strategies, as discussed in Section 3 and Section 4.

1.4. Acquisition modes and spatial sensitivity in mapping local deformation

High spatial sensitivity in the maps is obtainable either via a small pencil beam cross-section (down to 0.1μm) when using a far-field detector (pixel size $50...250\mu$m) or a small pixel size ($0.5...5\mu$m) with a near-field detector. In the latter case, the beam has a line or a rectangular ("full" or "box") cross-section. Fig. 22 summarises the scanning approaches and the dimensionality of the reconstruction problem.

Common in the monochromatic beam 3DXRD/HEDM/DCT methods is that the sample is rotated continuously around a single axis over typically 180° or 360° while integrating the images of a 2D area detector over small angular intervals of $\omega_{step} = 0.025...1°$. The diffracted beams from the grains are recorded in the dark beam area of the detector. The image stack is filtered and diffraction spots originating from the grains are segmented from the background as 2D images in the (u, v) detector space, or 3D image stacks in a (u, v, w) space, where $w = \omega/\omega_{step}$ is the image stack dimension. w is a real number, and the $w = 0$ position corresponds to $\omega = 0°$ rotational position. Although w is measured in number of images, its unit is equally referred to as a "pixel" within the (u, v, w) space of a diffraction spot. Grain centroids or voxels, their orientation, corresponding diffraction spots and (hkl) Miller indices are found in an indexing routine or by a forward simulation scheme. The data processing assumes kinematical diffraction conditions and a parallel beam geometry. Since the spatial, orientation and strain information are convoluted in the (u, v, w) diffraction spots, the spatial, orientation and strain resolution in all of these methods

are interdependent. They are also dependent on the grain size and intragranular misorientation and strain gradients in the polycrystal. Consider a grain of thickness l_g that is intersected along vector $\mathbf{v}$ by a microbeam of cross-sectional area s_b and a narrow energy bandwidth dE, while the sample is scanned with $d\omega$ rotational intervals. We will assume a constant curvature ξ of the lattice around an arbitrary axis. The curvature is linearly proportional to $(\nabla \boldsymbol{D})\mathbf{v}$, i.e. to the gradient components of the local deformation gradient tensor $\boldsymbol{D}$ along $\mathbf{v}$. There are three different conditions which limit the δ_{sub} sub-volume of the grain that simultaneously diffracts in a (hkl) diffraction spot within the $d\omega$ interval (i.e. in a single image):

I) If the deformation state varies little across the grain, the entire illuminated line section diffracts and δ_{sub} is proportional to the grain size.

$$\delta_{sub}^{I} \sim l_g \, s_b \tag{1}$$

II) If only a sub-region of the grain diffracts at a time, then, as an approximation, δ_{sub} is inversely proportional to the lattice curvature. The gradient components may create an out-of-plane curvature of the lattice and a gradient of the lattice spacing along the beam. The higher the intragranular misorientation and strain gradients the less volume diffracts simultaneously. Furthermore, δ_{sub} is approximately linearly proportional to dω.

$$\delta_{sub}^{II} \sim \frac{d\omega \, s_b}{\xi} \tag{2}$$

III) If dE results in an effective reflection curve which is wider than dω (typically not the case):

$$\delta_{sub}^{III} \sim \frac{dE \, s_b}{\xi} \, . \tag{3}$$

A small microbeam illumination much reduces the number of simultaneously diffracting grains and volume, hence it can tolerate much larger deformation levels in the sample before overlapping diffraction spots become critical. Along the rotation axis direction, the spatial resolution equals the beam size, and laterally it can theoretically approach the beam size, if a suitable 2D tomographic reconstruction algorithm is applied. A rigorous 2D or 3D reconstruction of the deformation field theoretically allows for utilising the fundamental spatial sensitivity of the setup. i.e. the microbeam size or the detector pixel size.

In the monochromatic scanning method in (Hektor et al., 2019)[37] and (Hayashi et al., 2019)[38], the 2D deformation reconstruction problem is circumvented and reduced to an indexing problem. The local strain values represent a weighted mean of the total volume contributing to the indexed reflections for one voxel. Either condition I or II may be determining the orientation and strain accuracy, and, counter-intuitively, they may increase with higher deformations, according to condition II.

In the case of box beam illumination, as in DCT and Near-Field HEDM, s_b covers the entire grain. In conventional (3D) DCT reconstructions the grains are assumed to have zero deformation, i.e. condition I applies, and the spatial resolution is limited by the detector pixel size and tomographic reconstruction theory. When assessing deformed grains, condition II applies and, again, results in increased input data (3D diffraction spot volumes instead of 2D projections) for the reconstruction problem that couples real space (shape) and deformation.

Grain boundaries are step functions in the (mis)orientation tensor, where the gradient is infinite, and provide the most obvious and robust means to define a spatial resolution for those methods which can map multiple grains. E.g. the spatial resolution of grain-by-grain processing methods can be quantified by the gaps or overlaps of the reconstructed grain volumes. Internal grain boundaries or grain boundaries on a free surface in this sense are analogous to high contrast features with a sharp interface in resolution standards for absorption tomography. When well defined features are absent within the grain volume and deformation gradients are smooth, spatial resolution cannot be inferred from the reconstructed deformation field. The accuracy of a 3D diffraction scanning method is best described by an expected or mean error of the following quantities: 1) location of grain or domain boundaries; 2) location of grain or domain centroids; 3) each orientation and strain tensor component; 4) each orientation and strain tensor gradient.

The angular range covered by a detector pixel as viewed from the sample is similar in both a typical far-field and near-field detector setup ($1...2\times10^{-4}$rad). The far-field 3DXRD/HEDM setup generally provides a better orientation and strain resolution due to a smaller point spread function, less susceptibility to mechanical instability due to the larger pixels, and more indexed families and reflections as a result of reduced overlap and higher signal-to-noise ratio.

1.5. Strain mapping with a near-field DCT setup

The full beam approach can utilise most photons from the synchrotron source of all scanning techniques, hence it has an inherent advantage in speed, simplicity of the setup, and easy switching to absorption or phase contrast imaging mode. These are exactly the advantages that allowed the DCT method to be transferred from the synchrotron to a laboratory-based instrument (King et al., 2013; McDonald et al., 2015; Sun et al., 2019; Bachmann et al.,2019)[58, 59, 60, 61]. A further advantage in time-resolved scans is described in Section 4.9. The efficiency of other scanning methods on the synchrotron is adversely affected by: the efficiency of the focusing optics, speed of positioning motors, overall setup stability, detector readout time. It should be noted that these constraints have been gradually being eliminated, e.g. by state-of-the-art detectors which have negligible dead time.

In the problem at hand, the "near-field" imaging detector is a few millimetres away from the sample, and the detector pixel size is much smaller than the average grain size. Debye-Scherrer rings are not formed on the detector at all, instead, individual diffraction spots are observed, typically well-separated (see Fig. 5). The experimental setup in the current paper (or in routine DCT at present) does not utilise the direct transmitted beam behind the sample but utilises the diffracted beams only. These form several unconnected diffraction spots from each grain and are segmented out from the image stack along the (u, v, w) directions. Subsequently, they are indexed according to their grain and (hkl) lattice plane of origin. Since a given (hkl) plane normal diffracts multiple times (maximum four times) over a 360-degree rotation, the observed and indexed diffraction spots of a specific grain are referred to with the linear index k instead. Several such (u, v, w) diffraction spots from a given grain are used as the input data for the 3D shape and strain reconstruction of that one grain.

The DCT indexing process is described in (Reischig et al., 2013)[29], the setup calibration and the mean grain position, orientation and strain fitting are outlined in (Reischig & Ludwig,

2019)[31]. Including a distortion correction of the raw images, the achievable accuracy in the simulated diffraction spot centroid positions can be significantly smaller than one pixel in (u, v) and often even better in w (i.e. smaller than the typical 0.05° stepping interval).

The diffraction spots are highly sensitive to the ω rotation. In case of zero intragranular deformation the projection is a parallel projection of the grain volume with limited extent along ω (defined by the energy bandpass and divergence of the incoming beam), as the entire grain volume diffracts at the same rotational position (Fig. 2a). A hypothetical state of constant deformation throughout the grain volume would result in small shifts of the projection directions and spot positions (Fig. 2b). Although the case of negligible intragranular orientation spread may be encountered in recrystallised and annealed materials, most structural materials exhibit some degree of local deformation, which is apparent as a spread in w. Within one integrated ω rotational step (e.g. $\omega_{step} = 0.05°$), only a sub-region of the grain would diffract and contribute to the intensity (Equation (2)). Over the entire ω range of the diffraction spots (typically 0.1...2°), in theory, all sub-regions of the grain would diffract at some point. The exact (u, v) and w position where a sub-region (or reconstructed voxel) diffracts on the detector within a given diffraction spot depends on the intragranular orientation and strain distribution within that grain. Any orientation or strain component in the sample reference that translates into either a stretch perpendicular to the (hkl) lattice planes or a tilt of those planes will result in a (u, v, w) offset in the diffraction peak position of a voxel (Fig. 2c). The intensity distribution inside the diffraction spots is typically a slowly varying continuous field, spread over (u, v, w). The grain shapes, the misorientation fields and the strain fields are highly convoluted, and cannot be simplified to an azimuthal and radial spread as in the case of Debye-Scherrer rings.

For a given voxel, the offset in this (u, v, w) projected peak position relative to a (u^*, v^*, w^*) reference projected position is computed in the diffraction model. The reference (u^*, v^*, w^*) position is where the voxel would project if it had the pre-determined grain average orientation and strain. The pixel size is comparable to the reconstruction voxel size, which is the basis for the spatial sensitivity. The thousands of active voxels which make up a grain all project somewhere within each indexed diffraction spot of the grain. This results in a cloud of intensities in the 3D (u, v, w) space of each diffraction spot, which is a distorted projection of the grain volume (Fig. 2c). In the near-field setup, this sensitivity to the offsets in u, v, w separately is the basis for the local (mis)orientation and strain (Type 3 stress) analysis. However, this orientation sensitivity combined with the box beam illumination also constitute the limiting conditions of the near-field setup. Namely, the diffraction spots start to severely overlap for increasing values of intragranular orientation spread, as observed in metallic materials which have been subjected to several per cent of plastic deformation.

The motivation of the current study is to present a model and a solver to explore the possibility of maximising information available from such full-beam illumination, while exploiting its photon efficiency. The data processing method is also adapted to line and pencil beam illumination, and it reconstructs not only the grain shapes but also the orientation and strain fields at the sub-grain level. The proposed algorithm, named Iterative Tensor Field (ITF) Reconstruction, is based on a vector representation of the 3D distribution of diffracting power and a 3D intragranular deformation

field, and aims to reconstruct this $\mathcal{F}(x, y, z) : \mathbb{R}^3 \mapsto \mathbb{R}^{1+9}$ tensor field on a grain-by-grain basis in the deformed state. It builds on the principles of kinematical diffraction and ray tracing, and employs an iterative solver.

The diffraction model is described in Section 2, and the ITF algorithm in Section 3. Based on similar principles, potential alternative models and solvers are set out in Section 4, although these are not applied or discussed in detail. The ITF solver is demonstrated on experimental data, as reported in Sections 5 and 6. The results and applicability of the solver and the approach are discussed in Section 7.

2. Diffraction model

2.1. Diffraction signal

The pixel intensities in an image frame are the summed contribution of the X-ray diffraction signal I_d and elements of the background noise, such as inelastic scattering $I_{inelastic}$ and fluorescence $I_{fluorescence}$ from the sample, the sample environment device, the beam defining aperture, and a dark current signal from the imaging sensor. The contribution of the photons arriving at the detector is modulated by the detector function, which is usually simplified to a point spread function convoluting the contributions from a small neighbourhood around a pixel:

$$I = F(I_d + I_{inelastic} + I_{fluorescence} + I_{sensor}) \,. \tag{4}$$

To model the diffraction signal, the grains within the sample volume are assumed to be "ideally mosaic", i.e. an ensemble of kinematically scattering crystallites, each contributing to the diffraction signal when passing through the diffraction condition of an (hkl) reflection while being illuminated with a monochromatic beam and rotated at a rotational speed ω_s around the rotation axis. An analytical solution of this total integrated diffracted intensity (or diffracting power) I_{cryst} exists for a free-standing deformation-free crystallite, using the "small crystal" approximation (see Warren, 1990 [62]):

$$I_{cryst} \sim \frac{I_0 \, \lambda^3 \, F_{hkl}^2}{\omega_s \, \delta_{cell}^2} \, L_{hkl} \, \delta_{cryst} \ , \tag{5}$$

where I_0 is the intensity of the incident X-ray beam, $\lambda = hc/E$ is the photon wavelength, E is the photon energy, h is Planck's constant, c is the speed of light, F_{hkl} is the structure factor of the crystal lattice, δ_{cell} is the volume of the crystal unit cell, δ_{cryst} is the volume of the small crystallite, and L_{hkl} is the Lorentz-polarisation factor that depends on the relative orientations of the (hkl) plane normal, the rotation axis and the polarisation vector of the (synchrotron) X-ray beam.

In a kinematical diffraction model, the phases and interference of the elastically scattered photons are neglected, and the real-valued intensity contributions from different parts of the sample are added up. Extinction of the transmitted beam due to diffraction along its path is neglected. For monochromatic beams the use of intensity at a specific rotational position w is not practical, instead, the integrated intensity is employed. To model the integrated intensity I_{uvw} diffracted from a 3D polycrystalline sample volume into a pixel region Ω_p in (u, v, w) of an image frame exposed during the scan, a real-valued integral needs to be computed over the surface area of the

pixel in (u, v), over the rotational step interval in w (during which the exposure is continuous), and over the 3D real space Ω_s covering the sample volume in (x, y, z) in the sample reference, taking into account the orientation and strain fields across the volume:

$$I_{uvw} = \iiint_{\Omega_p} \iiint_{\Omega_s} I_0 \, \mathcal{C} \, \mathcal{S} \, \mathcal{D} \; dx \, dy \, dz \, du \, dv \, dw \; ; \tag{6}$$

where I_0 is the intensity distribution of the incident beam:

$$I_0 = I_0(x, y, z, w, E) \; . \tag{7}$$

The incident beam and rotation axis directions are fixed and dependence on them is not shown. $\mathcal{C}$ represents the local crystallography, diffracting power and any potential (hkl) reflections of the lattice:

$$\mathcal{C} = \mathcal{C}(x, y, z, u, v, w, E, F_{hkl}, \boldsymbol{B_0}, \boldsymbol{U}(x, y, z), \boldsymbol{D}(x, y, z)) \; , \tag{8}$$

where $\boldsymbol{B_0}$ is the reciprocal basis matrix of the undeformed reference unit cell, $\boldsymbol{U}$ represents the local crystal orientation and $\boldsymbol{D}$ the local deformation, as defined in the Appendix.

$\mathcal{S}$ is an attenuation factor due to absorption and scattering inside the sample along the incident and diffracted beam path:

$$\mathcal{S} = \mathcal{S}(x, y, z, u, v, w, E) \; . \tag{9}$$

$\mathcal{D}$ is the detection efficiency of the detector and a scalar to transform intensity into detector units:

$$\mathcal{D} = \mathcal{D}(E) \; . \tag{10}$$

We use a grain-by-grain approach where the diffraction signal from the indexed individual grains are concentrated into a finite number of segmented and indexed diffraction spots that are treated independently, assuming no contribution (overlap) from other grains. Voxel elements of a grain volume are assumed to diffract as a "small crystal" when exposed and rotated around the rotation axis through a reflection k with the Miller indices (hkl), and each gives rise to the integrated intensity I_k. The strength of a reflection is characterised by the scalar intensity modulus κ_k which comprises all relevant effects:

$$\kappa_k = \delta_{vox} \, I_0 \, \mathcal{D} \, \mathcal{C}_{hkl} \, \mathcal{S}_k \, L_k \tag{11}$$

$$C_{hkl} \sim \frac{\lambda^3 \, F_{hkl}^2}{\delta_{cell}^2 \, \omega_s} = const \; . \tag{12}$$

A parallel beam geometry is assumed for the synchrotron beam, the incident beam direction, intensity and photon energy is considered constant everywhere in the laboratory reference frame and during the scan: $I_0 = const$ and $\lambda = const$. Alternatively, the intensity profile across the beam cross-section can easily be monitored by moving the sample and beam stop out of the beam and recording reference images. The detector response is also assumed to be constant over the field of view of the system: $\mathcal{D} = const$. Due to the typically small grain size compared to the sample cross-section, and the changes in diffracted beam directions as a result of deformation being small,

one can reasonably assume that the total self-attenuation the rays are subject to on their paths are constant across the volume of a grain and across the entire w range of a reflection: $\mathcal{S}_k = const.$ The same argument stands for the geometric factor $L_k = const.$ Using fixed size cubic voxels, the voxel volumes are also constant, when a grain completely fills in the volume of a voxel. These assumptions, in an ideal case, yield the same integrated intensity for each voxel of a grain within a diffraction spot.

To account for the case when the voxel is not completely occupied by the crystal and to allow for local variations in the reconstruction, the following product is used for the integrated intensity I_{jk} of a voxel j in diffraction spot k:

$$I_{jk} = p_j \, \kappa_k \,, \tag{13}$$

where p_j is the scalar diffracting power of voxel j and is the same for each reflection k. The p_j values define the shape of a grain. They are not known initially and allowed to change from voxel to voxel during the shape reconstruction. Using binary values for p_j allows for a simple representation of grain volumes – as commonly used in DCT.

The intensity modulus κ_k may be precomputed and calibrated for the specific hardware and sample material or fitted during the iterations, as shown in Section 3.4. We further make the assumption that p_j and κ_k are not directly dependent on the deformation state of a voxel. This appears to be a workable simplification for metals, although more experimental data and studies on the consistency and error of the reconstructions will be required to justify it. It is, nevertheless, reasonable to expect that the intensity modulus varies sufficiently slowly with the deformation components, and that its behaviour could be characterised by a fairly simple function. Having an adequately calibrated function in relation to deformation, the intensity modulus of each voxel could be updated during the iterative solution without significantly perturbing the local linear behaviour of the solver proposed in the following sections.

2.2. Intensity distribution function

The integrated intensity from a voxel is distributed over an area of a small number of pixels in the (u, v) image plane, and over a narrow range of w rotational intervals, according to an intensity distribution function. An accurate description of how the intensity is precisely distributed would need to take into account intricacies of the detector elements: the scintillator that transforms the X-rays into visible light, the visible light optics and the imaging sensor. In particular, the following aspects play an important role:

- precise shape of the finite voxel element and the diffracted wave front;
- absorption conditions and visible light generation from X-ray photons in the scintillator;
- incident angle between the impinging beam and the scintillator;
- afterglow (light emission delay) of the scintillator;
- propagation and internal reflections of the visible light inside the optics;
- detection of visible light photons and cross-talk between the pixels of the imaging sensor;

- read-out and digital conversion characteristics of the imaging sensor.

For faster computation of the model, this complex process is approximated by a combination of an intensity distribution function that describes the peak shape of each voxel, and a point spread function that describes a blurring of the total combined deposited intensity from the voxels. The intensity distribution function is sensitive to small changes in the deformation state of a voxel, and is a crucial element of the model that should be chosen with consideration, as it can significantly affect the fidelity of simulated diffraction spots and the processing time.

Each diffraction spot k of a grain is stored as a 3D array of pixel intensity values, and ordered in memory contiguously as the vector where the order of dimensions are (v, u, w). Pixels within a diffraction spot are identified with the linear index i, which normally only lists active pixels, i.e. those which receive an intensity contribution.

In the model, one diffracted ray j initiates from the centroid position $\mathbf{x}_j = (x, y, z)$ of voxel j in the sample reference, and it intersects the detector plane at (u, v) at rotational position w. This $\mathbf{u}_{jk}(\mathbf{x}_j, \mathbf{d}_j) = (u, v, w)$ projection position represents the centre or the peak of the intensity distribution of that voxel in diffraction spot k, and it is a function of the nine deformation components $\mathbf{d}_j = d_{jm}$ of the voxel, where $m = 1...9$. Bragg's law and the setup geometry determines $\mathbf{u}_{jk}$, see Appendix for the computation. Ray j deposits its intensity in a small neighbourhood of $\mathbf{u}_{jk}$ over N_t number of detector pixels which are denoted by $n = 1...N_t$. The look-up table $i = \psi_{jkn}$ returns pixel index i, where intensity is deposited from voxel j in diffraction spot k which has the list index n, and it is used in the forward projection (simulation) of the pixel intensities.

The intensity distribution function $t_n(\mathbf{u})$ determines the peak shape, i.e. what fraction of the intensity is assigned to an affected pixel n. The same function is used for all voxels, reflections and grains. Normally the further away the centroid of a pixel is from the ray position $\mathbf{u}$, the lower its value. A suitable intensity distribution function should meet the criterion that the integral sum of the intensity over all affected pixels must be one.

$$\sum_{1}^{N_t} t_n = 1 \tag{14}$$

The set of voxels j that contribute intensity to a given (i, k) pixel with list index n are stored and returned in the look-up table $j = \phi_{ikn}$. This look-up table ϕ_{ikn} is used in the backprojection operation during the iterations, and can be regarded as the "inverse" of ψ_{jkn}.

The intensity of pixel i in diffraction spot k is denoted with q_{ik}. Considering kinematical diffraction conditions, the resulting intensity of a pixel is the sum of the intensity contributions from all rays that affect that pixel:

$$q_{ik} = \kappa_k \sum_{n=1}^{N_t} \sum_{j \in \phi_{ikn}} p_j \, t_{n(\mathbf{u}_{jk}(\mathbf{x}_j, \mathbf{d}_j))} \, . \tag{15}$$

Once computed, the list of pixel intensities can be reassigned into the original (u, v, w) 3D array format of the diffraction spot. The centroids of the pixels are at integer numbers of (u, v, w), which are equal to the pixel integer indices (uvw) within the spot. The linear pixel index i is an equivalent notation of the 3D indices (uvw).

The value of p_j may change from voxel to voxel, or it can be forced to be a binary value for a discrete grain shape reconstruction. Prior to discretisation, nevertheless, it is treated as a floating

point value during the reconstruction. The most simple form of t_n would be to assign the total intensity of the ray to one single pixel, the nearest pixel to the ray position (u, v, w). However, this would mean that the pixel intensity would remain constant for a small deformation change, and it would abruptly drop to zero, once the ray position is closer to another pixel. The pixel intensity as a function of the deformation components would not be continuous or differentiable. Instead, we choose to use a simple and feasible form of the intensity distribution function, which is advantageous for the linearisation and effective computation of the pixel intensities, and their derivatives w.r.t. the deformation components. We use a linear interpolation, where the intensity diffracted from a voxel is distributed among the 8 nearest neighbouring pixels in (u, v, w), i.e. a $2 \times 2 \times 2$ pixel neighbourhood. In order for this interpolation to be valid, it is necessary that there is no gap in the sample rotation, exposure and integration of the intensities in consecutive images by the detector. Such integration gap may arise, for example, when the read-out time of the detector (during which the signal accumulation is interrupted) is non-negligible compared to the exposure time per image, or due to synchronisation problems.

When applying t_n to a projected ray position (u, v, w), the $2 \times 2 \times 2$ pixel neighbourhood is defined by the indices $(u^* v^* w^*)$, which correspond to the coordinates (u^*, v^*, w^*) of the first corner pixel $(n = 1)$ of the neighbourhood:

$$u^* = floor(u) \qquad v^* = floor(v) \qquad w^* = floor(w)\,. \tag{16}$$

Six linear interpolation coefficients c describe the distance of the ray position from the lower and upper voxels in the $2 \times 2 \times 2$ neighbourhood:

$$c_u^+ = u - u^* \qquad c_v^+ = v - v^* \qquad c_w^+ = w - w^* \tag{17}$$

$$c_u^- = 1 - c_u^+ \qquad c_v^- = 1 - c_v^+ \qquad c_w^- = 1 - c_w^+\,. \tag{18}$$

The t_n intensities deposited into the 8 neighbouring voxels ψ_n are a linear combination of those six coefficients:

$$\begin{aligned}
\psi_1 &= (u^*, v^*, w^*) & t_1 &= c_u^- c_v^- c_w^- \\
\psi_2 &= (u^*, v^*, w^* + 1) & t_2 &= c_u^- c_v^- c_w^+ \\
\psi_3 &= (u^*, v^* + 1, w^*) & t_3 &= c_u^- c_v^+ c_w^- \\
\psi_4 &= (u^*, v^* + 1, w^* + 1) & t_4 &= c_u^- c_v^+ c_w^+ \\
\psi_5 &= (u^* + 1, v^*, w^*) & t_5 &= c_u^+ c_v^- c_w^- \\
\psi_6 &= (u^* + 1, v^*, w^* + 1) & t_6 &= c_u^+ c_v^- c_w^+ \\
\psi_7 &= (u^* + 1, v^* + 1, w^*) & t_7 &= c_u^+ c_v^+ c_w^- \\
\psi_8 &= (u^* + 1, v^* + 1, w^* + 1) & t_8 &= c_u^+ c_v^+ c_w^+
\end{aligned} \tag{19}$$

The total diffracted and deposited intensity from a voxel is preserved, $\sum_1^8 t_n = 1$, which means that this t_n is an adequate intensity distribution function.

A variety of other types of intensity distribution functions can be considered. There is an obvious benefit of a smaller spread where a lower number of pixels are affected by the ray and have to be included in the computation. A high-fidelity function would depend on the mosaicity

and strain state of the grains, and the divergence and energy bandwidth of the incident beam. A commonly used relative energy bandwidth dE/E in experiments is 10^{-4} to 10^{-3}, which is adapted to a typical ω_{step} of 0.05°. The intensity distribution function proposed above appears to be a good approximation when deformation is apparent through extended diffraction spots in w. It should be noted, however, that for grains with small deformation gradients the reflection curve may be sharp and fall within one rotational step, so the linear interpolation along w leads to a discrepancy.

The 3D intensity distributions of the diffraction spots are convoluted with the point spread function $s(u, v)$ of the detector in two dimensions over (u, v) to simulate a blurring effect.

2.3. Link between voxel deformations and pixel intensities

The deformation gradient tensor field $\boldsymbol{D}(x, y, z)$ in the current framework is compatible with finite strain theory, i.e. not restricted to small strains, and applied as defined in the Appendix. It is solved for each voxel in the deformed state, thus local displacements in the underlying displacement field are irrelevant. The deformation field is defined directly by its nine deformation components $\mathbf{d} = d_{jm}$ in the sample reference, rather than by the unit cell parameters, which contributes to faster forward simulations. A $\boldsymbol{D}$ solution can be decomposed into misorientation and strain (see Appendix), or optionally, $\boldsymbol{D}$ can account for misorientation only. For alternative treatments of the link between lattice deformations and diffraction, see (Oddershede et al., 2010, Bernier et al., 2011, Edmiston et al., 2011)[23, 19, 24].

The link between the pixel intensities q_{ik}, the diffracting power (grain shape) p_j and the deformation tensor components d_{jm} is established via computing their derivatives $\frac{\partial \mathbf{q}}{\partial \mathbf{t}}$, $\frac{\partial \mathbf{t}}{\partial \mathbf{u}}$, $\frac{\partial \mathbf{u}}{\partial \mathbf{d}}$ during the iterations. The forward derivatives of the peak shifts w.r.t. the deformation components can be computed with finite differences by forward simulating all peak positions for a small change in each deformation component m, i.e. nine forward simulations in total.

An explicit formula can be derived for the derivatives, nevertheless there may not be a gain in computation time, and reusing the forward simulation code to compute the finite differences allows for a more straightforward and reliable implementation. Given that the peak shifts are close to linear, these derivatives change slowly with the deformation state, so they can be kept constant and stored over several iterations. Depending on the grain size and diffraction geometry, their change across the voxels of a grain is also moderate, and may potentially be considered constant (not the case in our current implementation). The $\frac{\partial \mathbf{u}}{\partial \mathbf{d}}$ derivatives are a useful measure of how sensitive the peak shifts are to small deformation:

$$\frac{\partial \mathbf{u}}{\partial \mathbf{d}} = \left(\frac{\partial u_{jk}}{\partial d_{jm}}, \frac{\partial v_{jk}}{\partial d_{jm}}, \frac{\partial w_{jk}}{\partial d_{jm}} \right) . \tag{20}$$

The *deformation sensitivity* χ_m indicates the average change in a deformation component m that can be detected with a one pixel peak shift along u or v, or a one image shift along w. It refers to a specific orientation in the sample (and location, to a lesser extent) or to a grain.

$$\chi_m = \left(\frac{1}{\mathrm{mean}\left|\frac{\partial \mathrm{u_k}}{\partial \mathrm{d_m}}\right|}, \frac{1}{\mathrm{mean}\left|\frac{\partial \mathrm{v_k}}{\partial \mathrm{d_m}}\right|}, \frac{1}{\mathrm{mean}\left|\frac{\partial \mathrm{w_k}}{\partial \mathrm{d_m}}\right|} \right) \tag{21}$$

The *peak deformation sensitivity* χ_m^+ indicates the smallest change in a deformation component m that can be detected in any of the reflections with a one pixel peak shift along u or v, or a one

image shift along w.

$$\chi_m^+ = \left(\frac{1}{\max\left|\frac{\partial \mathrm{u_k}}{\partial \mathrm{d_m}}\right|}, \frac{1}{\max\left|\frac{\partial \mathrm{v_k}}{\partial \mathrm{d_m}}\right|}, \frac{1}{\max\left|\frac{\partial \mathrm{w_k}}{\partial \mathrm{d_m}}\right|} \right) \tag{22}$$

The deformation sensitivity can also be determined for an entire experiment (a combination of the setup and the material) by computing the mean sensitivity of all grains and all observed reflections.

The derivative of the intensity distribution function w.r.t. the peak shifts can be expressed with a linear combination of the c coefficients computed beforehand. With an example of the first two pixels in the $2 \times 2 \times 2$ neighbourhood:

$$\frac{\partial t_1}{\partial u} = -c_v^- c_w^- \qquad \frac{\partial t_1}{\partial v} = -c_u^- c_w^- \qquad \frac{\partial t_1}{\partial w} = -c_u^- c_v^- \tag{23}$$

$$\frac{\partial t_2}{\partial u} = -c_v^- c_w^- \qquad \frac{\partial t_2}{\partial v} = -c_u^- c_w^- \qquad \frac{\partial t_2}{\partial w} = +c_u^- c_v^- \qquad etc. \tag{24}$$

The derivatives exist, and are continuous monotonic functions over the range of one pixel in u, v and w, i.e. as long as the ray projects into the same $2 \times 2 \times 2$ pixel region. When the ray reaches the boundary of the $2 \times 2 \times 2$ neighbourhood, the derivatives abruptly change sign or become zero outside the neighbourhood region. This is the main reason why the problem at hand is non-linear.

If the influence of the convolution with the detector point spread function is neglected, the derivative of a given pixel intensity w.r.t. the intensity distribution function is:

$$\frac{\partial q_{ik}}{\partial t_{jkn}} = \begin{cases} p_j \, \kappa_k & for \quad j \in \phi_{ikn} \\ 0 & for \quad j \notin \phi_{ikn} \ . \end{cases} \tag{25}$$

A voxel j contributes only once to a pixel i in a reflection k with its corresponding neighbourhood index n according to a symbolic look-up table $n = \eta_{ijk}$, which is not explicitly stored or used. Combining the above derivatives yields the expression for the derivative of a given pixel intensity q_{ik} w.r.t. a deformation component m of a contributing voxel $j = \phi_{ikn}$ and neighbourhood index $n = \eta_{ijk}$:

$$\mathbf{A}_d = \left.\frac{\partial q_{ik}}{\partial d_{jm}}\right|_{j \in \phi_{ikn}} = p_j \, \kappa_k \left(\frac{\partial t_{jkn}}{\partial u_{jk}} \frac{\partial u_{jk}}{\partial d_{jm}} + \frac{\partial t_{jkn}}{\partial v_{jk}} \frac{\partial v_{jk}}{\partial d_{jm}} + \frac{\partial t_{jkn}}{\partial w_{jk}} \frac{\partial w_{jk}}{\partial d_{jm}} \right) \ . \tag{26}$$

Similarly, the derivative of a given pixel intensity w.r.t. the diffracting power p_j of a given voxel:

$$\mathbf{A}_p = \left.\frac{\partial q_{ik}}{\partial p_j}\right|_{j \in \phi_{ikn}} = \kappa_k \, t_{jkn} \ . \tag{27}$$

The derivatives are zero for all other pixel-voxel (i, j) combinations. Only the non-zero elements are computed and stored as matrices, offering a relatively memory-efficient sparse representation.

In the implementation of the solver algorithm the $\frac{\partial \mathbf{u}}{\partial \mathbf{d}}$ derivatives are the most expensive to compute, however, these can then be stored and used over a number of iterations while kept constant. The c coefficients are recomputed in each iteration, from which the t_{jkn} values, the $\frac{\partial \mathbf{t}}{\partial \mathbf{u}}$ derivatives and the $\boldsymbol{A}$ matrices can be generated by a few multiplication and addition operations, resulting in fast computations.

3. Solution by local linear optimisation

3.1. Inferring shape and deformations as a linear optimisation

Starting from an adequate initial approximate shape and deformation state, small corrections are applied to the diffracting power (shape) and deformation components of all voxels simultaneously in an iterative manner (Fig. 4). In the current implementation one grain is processed at a time, entirely independently from the others, hence the grains in the volume can easily be dealt with in independent parallel processes.

The pixel intensities and the above derivatives are computed for all voxels of a grain that are active for a given shape and deformation field. For the sake of simplicity in this description, all active pixels in all diffraction spots are contained in a single vector $\mathbf{q} = q_{ik}$, and all deformation components (misorientation and/or strain) of all active voxels are contained in a single vector $\mathbf{d} = d_{jm}$.

The difference between the measured $\mathbf{q}^{mes}$ and simulated $\mathbf{q}$ pixel intensities is computed in each iteration:

$$\Delta\mathbf{q} = \mathbf{q}^{mes} - \mathbf{q} \ . \tag{28}$$

This difference is to be minimised as far as possible in every iterative step of the solution by finding an adequate set of corrections in diffracting powers and/or deformation components. Utilising the derivatives above, a local linear problem at the current solution can be formulated as:

$$\Delta\mathbf{q} = \begin{bmatrix} \boldsymbol{A}_d & \boldsymbol{A}_p \end{bmatrix} \begin{bmatrix} \Delta\mathbf{d} \\ \Delta\mathbf{p} \end{bmatrix} = \boldsymbol{A}\,\Delta\mathbf{c} \ , \tag{29}$$

where $\Delta\mathbf{d}$ is the corrections to be applied to the deformation components, $\Delta\mathbf{p}$ is the corrections to the diffracting powers, both either positive or negative, and contained in a single vector $\Delta\mathbf{c}$ for simplicity. The $\boldsymbol{A}$ matrices contain the intensity contributions to each pixel (one row per pixel) from all deformation components and diffracting powers (one column per component).

Since the linear system typically contains more unknown parameters than equations, an objective function is constructed to be minimised by a solver. Several algorithms are known to handle such large linear systems and approximate a solution. The system at hand is analogous to a computed tomography problem, where a Simultaneous Iterative Reconstruction Technique (SIRT) or a Conjugate Gradient (CG) method provides effective means of solution (Sluis & Vorst, 1990) (Gregor & Fessler, 2015)[63, 64]. SIRT is routinely used for the shape reconstruction of moderately deformed grains in DCT (Ludwig et al., 2009)[65], and its discrete counterpart, DART has also been demonstrated to be very effective (Batenburg et al., 2010)[66]. SIRT and CG have also been used for determining the orientation distribution function of a single grain (Hansen et al., 2009)[67]. More robust algorithms, for example the Chambolle-Pock method (Chambolle & Pock, 2011) (Sidky et al., 2012)[68, 69], that have been used in 6D shape and orientation reconstructions (Viganò et al., 2014)[52], could also be considered.

Since the components of the linear system change as the deformation components and diffracting powers change, a linear solver which does not require much computation to initialise (preconditioning) and which does not heavily build on previous iteration steps are the best suited to the

problem. SIRT and CG are prime candidates for their simplicity, and have shown convergence in preliminary simulation tests. One can choose to keep the current linear system for a number of sub-iterations, if that provides the best overall convergence rate for the non-linear problem. CG may need restarting after a certain number of main iterations, as the corrections do depend on prior steps.

Translated into a least squares problem, the solver tries to minimise the objective function Γ_0 which is the square of the L2 norm (denoted by $\|.\|_2$) of the residual vector.

$$\Gamma_0 = \|\Delta\mathbf{q} - \boldsymbol{A}_d\Delta\mathbf{d} - \boldsymbol{A}_p\Delta\mathbf{p}\|_2^2 = \|\Delta\mathbf{q} - \boldsymbol{A}\,\Delta\mathbf{c}\|_2^2 \tag{30}$$

$$\Delta\mathbf{c}^* = \underset{\Delta\mathbf{c}}{\operatorname{argmin}}(\Gamma_0) \tag{31}$$

In SIRT the corrections in each iteration α are computed as a backprojection operation, using the transpose matrix $\boldsymbol{A}^T$. The initial values of $\Delta\mathbf{c}^*$ at the start of the iteration are zero: $\Delta\mathbf{c}_{(\alpha=0)} = \mathbf{0}$. The backprojection distributes the residual errors of the pixels among the contributing parameters, here the deformation components and/or diffracting powers, with a given weight. The weights can be chosen within some limits, e.g. based on the L1 or the L2 norm of the intensity contributions to a pixel, where the model would be expected to converge (Sluis & Vorst, 1990)[63].

We choose to use the L2 norm weighting as, for example, in (Kak & Slaney, 2001)[70]. In the following formulae, the index i covers all active pixels in all diffraction spots, the index j covers all deformation components and diffracting powers in all active voxels, and the look-up tables have the corresponding form: ϕ_i and ψ_j. The SIRT solution of a given deformation component or diffracting power j after iteration $\alpha + 1$ is:

$$\Delta c_{j(\alpha+1)} = \frac{1}{\sum_{i\in\psi_j}\|\boldsymbol{A}_{ij}\|}\sum_{i\in\psi_j}\frac{\boldsymbol{A}_{ij}\left(\Delta q_i - \sum_{j\in\phi_i}\boldsymbol{A}_{ij}\Delta\mathbf{c}_{(\alpha)}\right)}{\sum_{j\in\phi_i}\|\boldsymbol{A}_{ij}\|^2} + \Delta c_{j(\alpha)}\ . \tag{32}$$

In practice, the correction may be computed in only one step, without iterations. If the $\boldsymbol{A}$ matrix is kept constant, a small number of further iteration steps can be computed. Although this does not any more accurately represent the geometry due to the change in deformation state, it may be a more efficient way of approximating the solution.

After the SIRT iterations α, the deformation components and diffracting powers are updated with the SIRT correction in each main iteration β:

$$\mathbf{c}_{(\beta+1)} = \mathbf{c}_{(\beta)} + \Delta\mathbf{c}^*\ . \tag{33}$$

The exact projection geometry is recomputed with the updated deformation components, and the $\boldsymbol{A}$ matrix is regenerated to repeat the SIRT steps in a next iteration loop (Fig. 4). Note that, although the simultaneous correction of the deformation components and the diffracting powers is formally possible, the solution might only converge close to the true solution.

3.2. Regularisation and mechanical constraints

The objective function Γ can naturally include additional mechanical constraints ($\Gamma_1(\mathbf{d})$) or physical criteria regarding the shape or diffracting power ($\Gamma_2(\mathbf{p})$) in the solution space to improve the well-posedness and convergence rate. For example, in a formulation using the L2 norm of the

deviation of the deformation components from zero, from the grain mean values or from some other reference value $\mathbf{f}_1$, the objective function becomes:

$$\Gamma = \Gamma_0 + \gamma_1\Gamma_1 + \gamma_2\Gamma_2 + etc. \tag{34}$$

$$\Gamma_1 = \|\mathbf{f}_1 - \boldsymbol{A}_1\Delta\mathbf{d}\|_2^2 \qquad \Gamma_2 = \|\mathbf{f}_2 - \boldsymbol{A}_2\Delta\mathbf{p}\|_2^2 \ . \tag{35}$$

The linearised system to be approximated using SIRT can be formulated as:

$$\begin{bmatrix} \Delta\mathbf{q} \\ \sqrt{\gamma_1}\,\mathbf{f}_1 \\ \sqrt{\gamma_2}\,\mathbf{f}_2 \\ \cdots \end{bmatrix} = \begin{bmatrix} \boldsymbol{A}_d & \boldsymbol{A}_p \\ \sqrt{\gamma_1}\,\boldsymbol{A}_1 & \mathbf{0} \\ \mathbf{0} & \sqrt{\gamma_2}\,\boldsymbol{A}_2 \\ \cdots & \cdots \end{bmatrix} \begin{bmatrix} \Delta\mathbf{d} \\ \Delta\mathbf{p} \end{bmatrix} \ . \tag{36}$$

The physical criteria or mechanical constraints would typically refer to the magnitude or gradients of the diffracting powers and/or the deformation components. The L2 norm is adapted to a SIRT solver, however, depending on the nature of the objective function, e.g. when L1 norms are involved, another suitable algorithm should be selected. Examples of potentially useful regularisation criteria include:

a) The L1 or L2 norm of the parameters in an absolute sense.

b) The L1 or L2 norm of the parameters relative to their deviation from predetermined grain mean values.

c) L1 or L2 norm of the gradients to enforce smoothness in the solution.

d) Strain compatibility: assuming that the grains would have zero orientation spread in their stress free state. It is normally not the case in polycrystals, in particular, metal grains tend to have a considerable mosaic spread according to their dislocation content even at very low residual stresses.

e) Static stress equilibrium: assuming linear elasticity, if the single crystal elastic moduli and the zero stress lattice parameters of the material are known, the stress tensor $\boldsymbol{\sigma}$ can be computed from the strain tensor for each voxel from Hooke's law (see Appendix). Using small strain theory, the strain components in the sample reference, with a good approximation, are a linear function of the deformation tensor components. The small body forces can be neglected, hence the divergence of the stress tensor field should be zero everywhere. The stress imbalance, i.e. the deviation from the static equilibrium condition, can be described locally for each voxel as the divergence of the stress tensor, which can be treated as a linear function of the stress or deformation components (see Appendix). The volume integral of the L2 (or L1) norm of the local deviations from static equilibrium across all voxels in the grain volume can be used as the objective function:

$$\Gamma(\mathbf{d}) = \|div(\boldsymbol{\sigma}(\mathbf{d}))\|_2^2 \ . \tag{37}$$

f) Elastic strain energy minimised: if the single crystal elastic moduli are known, the elastic strain energy density of the lattice can be computed as a quadratic function of the strain

components. Applying small strain theory, the strain components in the sample reference can be approximated as a linear function of the deformation tensor components. The integral of the local strain energy density ϑ across the grain volume can be used in the objective function:

$$\Gamma(\mathbf{d}) = \delta_{vox} \sum_j \vartheta(\mathbf{d}_j) \,. \tag{38}$$

3.3. Iterative Tensor Field (ITF) reconstruction based on SIRT

This section describes the implementation and use of a SIRT-based solver (named Iterative Tensor Field reconstruction) in detail, which was also used to produce the experimental results reported in Section 6. Initial tests of the simultaneous reconstruction of diffracting power and deformation components from the 3D diffraction spots did not show satisfactory convergence in our simulations. This is presumably due to the fact that if the current deformation field is far from the true solution, many of the voxels project into empty pixels, and the grain shape becomes corrupted during the iterations. This effect is much eliminated when the shape reconstruction is based on the 2D diffraction spots that are integrated over w, just like in a regular DCT reconstruction. Therefore, in our current approach, the shape reconstruction is separated from the deformation reconstruction, and is performed from the 2D diffraction spots with the current deformation field fixed, before the first and then after every I_{def} number of main deformation iteration cycles. In each main deformation iteration cycle, the exact projection geometry is recomputed. Each main iteration may contain multiple SIRT sub-iterations, however, in the current implementation only one single SIRT step is used per main iteration cycle. When inferring the deformation components, the shape, i.e. the active voxels, are fixed (Fig. 4).

The grain average orientation and strain values are fitted beforehand using the diffraction spot centroids (Fig. 3). The deformation components are sought as an additional deformation to the grain average state. In the deformation solver demonstrated in this study, we use the following objective function in the linear problem in each main iteration, without applying any mechanical constraints:

$$\Gamma = \|\Delta\mathbf{q} - \boldsymbol{A}_d \Delta\mathbf{d}\|_2^2 + \gamma \, \|\mathbf{d} + \Delta\mathbf{d}\|_2^2 \,, \tag{39}$$

where $\mathbf{d}$ is the current deformation solution. The first term aims at eliminating the pixel intensity deviations and the second one is a Tikhonov regularisation term which prefers deformation components closer to the initial grain average values.

In every iteration there is a possibility to apply additional corrections to the SIRT solution, although such constraints should ideally be included as an extra term in the objective function or included in the model. In the current implementation, we apply a smoothing operation to the deformation field in every main iteration by applying a $3 \times 3 \times 3$ mean filter (box filter) including the 26 nearest neighbours of a voxel. The actual resulting field is a linear combination of the mean filter (with weight W_s) and the current solution (with weight $1 - W_s$). This smoothing is analogous to including a spatial gradient term in the objective function. From an implementation perspective this way is beneficial because such smoothing functions are available in code libraries.

A weighting factor is applied to the backprojection contributions of the reflections. The angle of incidence onto lattice planes with a normal closer to the rotation axis changes slower w.r.t. ω. Hence, they sweep through their reflection curve slower, resulting in a higher integrated intensity, i.e. a larger L_k and κ_k in Equation (11), and a higher signal-to-noise ratio. These diffraction spots are also more spread out in w, and they constitute higher deformation sensitivity, although they are also more susceptible to diffraction spot overlap. To account for these higher quality reflections, the backprojection contribution of the reflections are weighted with their $\sqrt{\kappa_k}$ value.

Furthermore, an additional weighting factor ξ_{ik} is applied to each pixel in each diffraction spot. ξ_{ik} is normally one but it allows for further fine-tuning of the pixel contributions in the backprojection. Noise in the images may get magnified in the backprojection, especially near the edges of a diffraction spot, where few voxels project and the denominator in Equation (32) is small. In these areas, background noise and under- or over-segmentation of the spots has a significant effect, hence ξ is set to zero. More abrupt disturbance may arise from spot overlaps, scintillator defects and faulty detector pixels, etc. Thus, the absolute values of the $\mathbf{\Delta d}$ corrections from each reflection and of the combined $\mathbf{\Delta d}$ correction are forced within preset limits. Since typically tens of diffraction spots are used per grain, any suppressed contribution is averaged out in the backprojection, and such fine-tuning of the pixel contributions helps convergence.

Control over weighting factors ξ_{ik} also provides the option to include or exclude diffraction spots from the analysis. For example, as the iteration progresses it may become more apparent if any of the spots are corrupted by overlap. We currently apply an automatic preselection of the reflections before the iterations, where outliers are excluded based on their mean (u, v, w) positions, and this set is kept fixed during the iterations.

The final deformation d_{final} state of the voxels is a combination of the initial grain average and the local corrections found by the iterative solver (see Appendix).

The SIRT algorithm provides not only the direction but also the magnitude of the deformation corrections. Alternatively, a fixed step size (10^{-4} to 10^{-5} in the deformation components) can be applied to increase the convergence rate, while preserving the direction (sign) of the corrections.

Several figures of merit can be used to describe the fidelity of a solution and track convergence. Monitoring which pixels are active in the observed and simulated diffraction spots and the level of overlap between the two sets ("pixel hit rate") is an informative measure, given the unique 3D shapes of the spots from a deformed grain. In practice, the utility of this approach somewhat diminishes when the segmentation of the spots is too relaxed or too conservative.

Figures of merit can include, for example:

a) The L1 norm, the L2 norm, the mean or the median of the residual errors in the pixel intensities;

b) Voxel hit rate: the fraction of voxels which project into an active pixel, and not into a zero pixel;

c) Pixel hit rate: the fraction of active pixels which are reached by at least one ray from the voxels;

d) Deviation from mechanical constraints, such as static equilibrium (if the elastic moduli are known), etc.

Furthermore, to monitor the rate of convergence and stability, the value and rate of change of the norm, mean and standard deviation of the deformation parameters and their corrections can be employed. The condition to stop the iterations may be based on a combination of the above measures. We currently simply apply a fixed number of iterations. The final deformation field $\boldsymbol{D}$ in the solution is decomposed into an absolute orientation (3-component Rodrigues vector) and a 6-component strain tensor for each voxel in a post-processing step (see Appendix).

The complete grain maps are assembled from the individual grain volumes, similarly to standard DCT (Ludwig et al., 2009)[65]. Overlapping voxels are first removed, then filled in by the closest grain according to the 3D Euclidean distance of its nearest voxel to the overlap voxel. Filling in missing voxels around the grain boundaries (dilation) can be performed, in which case the orientation and strain fields are extrapolated linearly in 3D.

3.4. Grain shape reconstruction

In the current implementation, the deformation and shape reconstruction cycles are separate and interlaced. The shape reconstruction is carried out as the initial step, then after every I_{def} number of main iterations. It is performed from the 2D diffraction spots integrated over w, with the deformation field (thus also the diffraction geometry) fixed, and aims at reproducing the pixel intensities by optimising $\mathbf{p}$ in a regular SIRT problem:

$$\mathbf{q}^{mes,2D} = \boldsymbol{A}_p \, \mathbf{p} \ . \tag{40}$$

An initial shape reconstruction envelope is defined as the convex region in which more than 50% of the pixels (not all, to account for segmentation errors) backproject at zero deformation, plus an extra margin of a few voxels that takes potential deformation into account. The shape reconstruction cycle consists of a SIRT reconstruction of the real-valued diffracting powers in I_{real} number of iterations, which is interrupted with a thresholding and discretisation procedure, based on the assumption that the diffracting power varies little across the grain and is independent from the deformation state. Negative voxel values are set to zero and the solution is smoothed with a 3D filter in each SIRT iteration.

Discretisation has been previously shown to be effective in the shape reconstruction of undeformed grains by Batenburg et al. (Batenburg et al., 2010). In their 2D method, following an initial reconstruction, only the grain boundaries are corrected during the iterations. In our case, all grain voxels are allowed to change for the next set of I_{real} iterations, so that the grain boundaries do not need to be determined, which allows for a more simple and coherent implementation, although potentially less efficient. The binary threshold for determining the grain shape from the real-valued SIRT reconstruction is found iteratively similar to the approach described in (Der Sarkissian et al., 2018)[71]. A lower threshold results in a larger binary grain volume. In each iteration step, for a given binary threshold, its corresponding κ_k values and the mean absolute residual error (the L1 norm) over all simulated versus measured pixels in all diffraction spots are computed. The threshold and its corresponding κ_k values (see Section 2.1) with the lowest error are chosen as

solution. The threshold search is a single parameter optimisation, where the error function is fairly smooth and usually has a well defined minimum.

For a given binary threshold and the resulting grain shape, the intensity modulus κ_k as a single scalar determines the diffracted intensity from a voxel or from the entire grain in diffraction spot k. For each diffraction spot, an estimate of the κ_k value is computed from each pixel as the ratio of the measured ($q_{ik}^{mes,2D}$) and forward projected q_{ik} intensities. From this set, the median value is taken as a robust estimate of κ_k of that reflection.

$$\kappa_k = \text{median}\left(\frac{q_{ik}^{mes,2D}}{q_{ik}}\right) \tag{41}$$

We use the median value of κ_k, rather than the mean, for each reflection as this provides a robust estimator even in case a diffraction spot is affected by an overlap up to 50% of its area. Currently, κ_k is estimated independently for each reflection. If the structure factors, self-attenuation, etc. are modelled correctly (Equation (11)) and the relative intensities of the reflections can be trusted, then they can also be taken into account when computing κ_k, eliminating the discrepancies caused by spot overlaps.

In each shape reconstruction cycle a new grain reconstruction envelope is determined with an extension around the current grain volume region to allow the grain volume to grow. The deformation components are extrapolated linearly over the extension region in 3D.

Accounting for knowledge of the microstructure, morphological constraints to the grain shape can be applied during the iterations. In the current solver, the binary grain volume is enforced to be a single connected region, holes in the volume are filled in, grain boundaries are smoothed, and spikes protruding from the volume are removed in a dilation-erosion (retaining only a connected region in the volume). For annealed microstructures these are usually safe assumptions.

A pseudo code of the grain shape reconstruction cycle is as follows:

AFTER every I_{def} number of main iterations DO SHAPE RECONSTRUCTION:

- Keep deformation field and projection geometry fixed
- Determine new grain reconstruction envelope
- Extrapolate deformation components
- FOR I_{shape} number of iterations DO:
    - DO I_{real} number of real-valued SIRT ITERATIONS
    - Set negative voxels to zero; smooth solution with a 3D filter
    - DO BINARY THRESHOLDING
        - Set new appropriate threshold based on previous values
        - Make binary grain volume by thresholding
        - Apply morphological corrections to volume
        - Forward project 2D diffraction spots
        - Compute median κ_k for each diffraction spot

```
        - Compute combined L1 norm of pixel errors
        - Stop, if number of grain voxels changed is lower than limit
    - Choose threshold (volume and κ_k) with lowest error
- Update active voxels in binary grain shape and deformation grid.
```

3.5. Spatial grids

The shape and deformation reconstruction are performed on two separate 3D grids in real space, with the shape grid having a smaller spacing – usually the pixel size of the detector. This ensures the maximum spatial resolution in the shape reconstruction and adequate sampling for smooth forward projected diffraction spots that are free from aliasing. The (u, v, w) values over the shape grid points are linearly interpolated in (x, y, z) based on the forward mapping of the deformation grid points $(x, y, z) \mapsto (u, v, w)$. These (u, v, w) ray positions, now with a higher concentration of points, are then accumulated into a 3D array to generate a diffraction spot. A weighting scheme for the intensities ensures consistency between the two grids for grid points that are near the boundary of the grain volume. Alternative supersampling methods in the forward projection may be considered to ensure smoothness of the diffraction spot intensities.

The backprojection is performed using the deformation grid and the intensity weighting scheme that is applied in the forward projection. The deformation grid is less dense than the shape grid, so that less deformation parameters need to be computed in the backprojection, which greatly benefits processing time. Its spacing is chosen to be adequate for the highest underlying spatial frequencies of the deformation field as observed in the images, or e.g. 1/2 to 1/3 of the spacing interval of the shape grid. Although the fact that the forward projection and backprojection happens on different spatial grids breaks the original linear formula used for SIRT (Equation (29)), the increased smoothness and continuity of the intensity distribution improves the underlying model and does not compromise the solution.

3.6. Well-posedness and initialisation

The original reconstruction problem combining the deformation field and the diffracting powers is inherently ill-posed because voxels with zero diffracting power can have any orientation and strain. Establishing the number of equations and number of unknown parameters is problematic at the start. For a better insight, it is useful to consider the linear form (Equation (29)) at the true solution, rather than the initial solution. At or very close to the true solution, the number of equations (known parameters) in (Equation (29)) is the number of detector pixels into which at least one ray projects. This is the same as the number of measured non-zero detector pixels, which is known from the input. However, due to the difficulty of segmenting the diffraction spots from a noisy background, the number of measured active pixels depends on the segmentation threshold, thus is not evident.

The more complex the deformation field and the larger the misorientation and strain gradients at the scale of observation (e.g. with variations over 2...10 times the detector pixel size), the more spread out the diffraction spots are (condition II, Equation (2)). Thus, the number of active pixels and equations in the linear form (Equation (29)) is also higher for essentially the same number of

unknowns, so the linear problem is less ill-posed. Note that in a rigorous 12D description of the problem (Section 1.3, and Fig. 21), with the same number of spatial voxels, the initial number of unknowns (the space of possible deformation combinations, consisting of three misorientation and six strain components) would increase proportionally to n_d^{3+6}, where n_d is the number of possible discrete values per deformation component considered, leading to a much more underdetermined problem.

The exact number of unknown parameters per grain in the present vector representation is also problematic to determine at the start, as the grain shapes are unknown. The number of voxels in the initial shape reconstruction envelope constitute the initial number of unknows (with one diffracting power value and nine deformation components each), which is also a fair approximation of the refined volume in the final solution.

3.7. Error estimation

The forward derivative $\boldsymbol{P}$ and the pseudoinverse $\boldsymbol{T}$ relate peak shifts to deformation components (see Section 4.3), and can be used as a basis for estimating the errors of a solution in the deformation components. However, in a real measurement, there is no way to pinpoint the true (u, v, w) projection positions of a single voxel within an extended diffraction spot, which could then be transformed into an error in the deformation components. As an alternative, an error assessment based on simulated data sets mimicking the real conditions could be produced.

A measure of the quality of the solution can, nevertheless, be computed for an entire grain using the figures of merit proposed in Section 3.3. On a voxel-by-voxel basis, an error figure can be produced by combining the residual pixel errors at the locations in $\mathbf{u}_j$ where a voxel projects.

A more exact way to estimate the local errors is analysing local deviations from static equilibrium in the measured stress field (as in Equation (37)), if the single crystal elastic constants of the sample material are known. The analysis can be extended to a larger scale by computing the total forces and moments acting on cuboid regions that include several voxels under a sliding window over the volume, which theoretically should be zero. However, these stress conditions will not detect any error that is present as a constant field of normal stresses (e.g. a hydrostatic stress state), unless they include a free surface where the stresses are known to be zero. Such analysis can also be performed on multiple grains, or at the grain boundaries, or over the entire grain map.

Another informative error estimate applying equilibrium at the macroscopic level can be the deviation of the total force through a complete cross-section of the sample from the externally applied force or from zero. For example, if the sample is loaded along the rotation axis, the surface integral of the stresses in the direction of the rotation axis through any complete section of the sample must be equal to the external force. Similar considerations apply to shear forces and the balance of moments.

4. Alternative models and solvers

In addition to the SIRT/CG-based Iterative Tensor Field Reconstruction method proposed in Section 3.3, alternative ways of inferring grain shapes and a deformation field inside grains of polycrystals can be considered. Building on the key concepts of kinematical diffraction, a vector

representation of the solution space and an iterative solution utilising local linearity, we propose a number of potential approaches that utilise a full beam (box beam) illumination for future consideration. In the following sections concepts 1 to 5 assume that the mean grain positions and orientations are known initially from indexing within some accuracy, while concepts 6 to 8 outline indexing-free methods. Concept 9 describes how time can be introduced in the reconstructions as the 4th dimension.

4.1. Concept 1: Global ITF

This concept is an extension of the ITF method presented in detail in Section 3.3 and in Section 6. As the memory requirements are feasible, it has the potential to be performed simultaneously on all grains, instead of grain-by-grain, while assuming or enforcing a single orientation per voxel. Voxel orientations near the grain boundaries could be checked and corrected or refined regularly during the iterations. If a sophisticated forward simulation is used that takes into account self-absorption in the sample and other contributions to Equation (11), the intensity in overlapping diffraction spots from two or more grains could be handled rigorously. Overlaps in the diffraction spots pose a major limitation to the current indexing and grain-by-grain processing, which could be much eliminated this way, and enable a more robust handling of twins, subgrains and small angle grain boundaries.

4.2. Concept 2: Omega-ITF

At small deformation levels (in the order of 10^{-4} to 10^{-3}), the peak shifts in (u, v) are typically a few pixels, which is small compared to the typical grain sizes of tens or 100s of pixels, leading to only a moderate deviation from the case of fixed parallel projections. This results in small (u, v) peak shifts and diffraction spots that are only moderately deformed in (u, v). The deformations are inferred only from the Δw_k peak shifts that are defined as a deviation from a reference w_0 position (w_0 refers to zero strain or the grain average strain).

From each measured 3D (u, v, w) diffraction spot two 2D (u, v) projection images are computed: 1) integrated image: each (u, v) pixel contains the integrated intensity of the diffraction spot along w; 2) moment image: each (u, v) pixel contains the deviation of the first moment (centre of mass) of the intensities along w (positive or negative). This moment should correspond to the sum of the Δw peak shifts of all voxels that project into the (u,v) pixel, i.e. the equivalent of a line integral of the Δw peak shifts. Since the Δw values can be approximated as a linear function of the deformation components (see Section 4.3.1), and the projection geometry can be regarded fixed, the deformation components can be found in a quasi-linear problem. It is analogous to regular tomography with the distinction that for each voxel several unknowns are sought. An approximation of the 3D grain shape can be reconstructed by SIRT, as it is routinely done in DCT. Using the reconstructed grain shape, the deformation components can be inferred with a regular SIRT, Conjugate Gradient or other methods from the moment images.

The approach may also be applicable to single crystals in X-ray topography and rocking curve imaging, when several (hkl) reflections are recorded and combined. Furthermore, the approach may be adapted to infer deformation fields from extinction contrast in the transmitted beam that occurs as shadows of diffracting grains in the alternative "direct beam" version of DCT, where only

a small number of grains are present in the sample cross-section (Johnson et al., 2008) (Ludwig et al., 2008)[72, 73]. The extinction spots can be treated similar to diffraction spots but with a negative intensity modulus and no peak shifts in (u, v). The moment images would be computed from the extinction peak shifts along w, and would constitute a projection geometry identical to regular computed tomography.

In light of the analysis regarding the uniqueness of 3D strain fields based on line integrals presented in [11], it should be noted that considering the w peak shifts only, without the shifts in (u, v), might not lead to a unique solution for the local deformation components.

4.3. Concept 3: Deformations from gradient intensity flow

This method builds upon the concepts of "peak shift inversion" and "intensity flow field", which we briefly introduce below.

4.3.1. Peak shift inversion

Small deformations have a quasi-linear effect on the peak shifts in (u, v, w) on the detector. For the moment, we put aside the problem of how to determine those peak shifts from projection images, discussed in the next subsection (Section 4.3.2). Assuming a linear relationship allows for a simple approximate inversion, i.e. obtaining a small correction of deformation components from peak shifts. Although this concept is not applied in the SIRT solver presented in Section 3.3, we speculate that this concept offers potential alternative solutions where, instead of the collective corrections as in SIRT/CG, more localised corrections are applied in solution space, and it also enables some means of error estimation.

A peak shift $\Delta\mathbf{u}_{jk}$ of a ray from diffracting volume element j in diffraction spot k can be approximated as a linear function of the deformation components $\mathbf{d}_j$ and the position $\mathbf{x}_j$ of the element in the sample reference frame. Combining the peak shifts and partial derivatives of a voxel from all diffraction spots into one $\mathbf{u}_j$ vector, the $\boldsymbol{P}$ matrix is defined:

$$\boldsymbol{P}_j = \begin{bmatrix} \frac{\partial \mathbf{u}_j}{\partial \mathbf{d}_j} & \frac{\partial \mathbf{u}_j}{\partial \mathbf{x}_j} \end{bmatrix} . \tag{42}$$

The peak shifts of an element in all diffraction spots can be written as the matrix-vector product:

$$\Delta\mathbf{u}_j = (\Delta u_j, \Delta v_j, \Delta w_j)^T = \boldsymbol{P}_j \begin{bmatrix} \Delta\mathbf{d}_j \\ \Delta\mathbf{x}_j \end{bmatrix} . \tag{43}$$

In the inverse relation, to find a suitable deformation and voxel position correction for a set of measured or assumed peak shift values, a generalised inverse (Ben-Israel & Greville 2003)[74] of matrix $\boldsymbol{P}$ can be utilised. In particular, the Moore-Penrose pseudoinverse is unique and provides a least squares fit for an input vector of peak shift values (which are necessarily subject to errors of the measurement or the estimate). There are typically tens of indexed diffraction spots available for a grain, of a variety of (hkl) indices, with non-coplanar scattering vectors substantially spanning 3D real space in the sample reference. The number of peak shift components combined from all observed diffraction spots is significantly higher than 12, hence the nine deformation components and the three spatial parameters can be reliably fitted. The Moore-Penrose pseudoinverse of $\boldsymbol{P}$

$$\boldsymbol{T}_j = (\boldsymbol{P}_j^T \boldsymbol{P}_j)^{-1} \boldsymbol{P}_j^T \tag{44}$$

can be computed as a matrix product, including a 12×12 matrix inversion, or by singular value decomposition or they can be derived analytically. An explicit least squares estimate of an adjustment in the deformation components $\Delta\mathbf{d}_j^*$ and voxel position $\Delta\mathbf{x}_j^*$ can be obtained for a set of estimated peak shift values $\Delta\mathbf{u}_j^*$:

$$\begin{bmatrix} \Delta\mathbf{d}_j^* \\ \Delta\mathbf{x}_j^* \end{bmatrix} = \boldsymbol{T}_j \Delta\mathbf{u}_j^* \ . \tag{45}$$

In more simple cases, $\boldsymbol{P}$ and $\boldsymbol{T}$ may exclude the spatial coordinates $\mathbf{x}$ and/or strain, and only include crystal orientation. A valuable property of theirs is that they vary relatively slowly w.r.t. the deformation components and the spatial position in the sample. Hence, once they are computed, they can be kept constant for a number of iterations, and, in case of small grains, one matrix may be a suitable approximation to be used for all voxels. Furthermore, the components in $\boldsymbol{P}$ and $\boldsymbol{T}$ themselves provide an estimate of what deformation and spatial resolution we may expect from the experimental setup.

A potentially useful variant of $\boldsymbol{P}$ and $\boldsymbol{T}$ is one that only takes into account the $\mathbf{w}_j$ shifts within the diffraction spots:

$$\boldsymbol{P}_{w,j} = \frac{\partial \mathbf{w}_j}{\partial \mathbf{d}_j} \qquad\qquad \boldsymbol{T}_{w,j} = (\boldsymbol{P}_{w,j}^T \boldsymbol{P}_{w,j})^{-1} \boldsymbol{P}_{w,j}^T \tag{46}$$

and from an estimate $\Delta\mathbf{w}_j^*$ of those provides a best fit correction for the deformation components (for details on its potential application, see Section 4.2):

$$\Delta\mathbf{w}_j = \boldsymbol{P}_{w,j} \Delta\mathbf{d}_j \qquad\qquad \Delta\mathbf{d}_j^* = \boldsymbol{T}_{w,j} \Delta\mathbf{w}_j^* \ . \tag{47}$$

4.3.2. Intensity flow field

The 12-parameter fitting using $\boldsymbol{T}$, used in a single step or iteratively, is essentially the same procedure as the one used for refining the grain mean (i.e. not a voxel) position, orientation and strain from the diffraction spot centroids (Reischig, 2008; Bernier et al., 2011; Oddershede et al., 2010; Reischig & Ludwig, 2019)[28, 23, 19, 31].

As opposed to fitting the spot centroid positions, the challenge at hand is that a grain is not represented by a single centroid but as a point cloud (a set of voxels). Knowing the $\boldsymbol{T}$ pseudoinverse in itself does not provide a solution, as we are faced with the original problem of not knowing which voxel contributes to a given pixel in the diffraction spots. We assume that a reasonable guess can be made of how the intensities within an entire diffraction spot could be rearranged to decrease or eliminate the pixel residual errors. This guess has the form of a physically meaningful displacement field which assigns a $(\Delta u^*, \Delta v^*, \Delta w^*)$ peak shift to each ray (each voxel). We will refer to such a vector field defined for each diffraction spot, as the intensity flow $\varphi_k(\mathbf{u}_k) : (u_k, v_k, w_k) \mapsto (\Delta u_k^*, \Delta v_k^*, \Delta w_k^*)$. It essentially provides a local driving force for a ray to move into a certain more preferable direction within the diffraction spot. It can also be regarded as the gradient of a potential field where lower energy potential corresponds to lower pixel errors locally. The mappings $\varphi_k(\mathbf{u}_k)$ from all diffraction spots are combined into one function $\varphi(\mathbf{u}) \mapsto \Delta\mathbf{u}$. Pseudoinverse $\boldsymbol{T}$ can be applied to transform these effective guesses of the peak shifts

into a deformation and position correction for each voxel:

$$\begin{bmatrix} \Delta \mathbf{d}_j^* \\ \Delta \mathbf{x}_j^* \end{bmatrix} = \boldsymbol{T}_j \, \varphi(\mathbf{u}_j) \ . \tag{48}$$

4.3.3. Gradient intensity flow as a deformation solver

The outlined concepts can be employed in a solver that aims to find the deformation field for fixed voxel positions and a fixed grain shape, treating the voxels independently. One would perform forward projection with the parameters $\mathbf{d}$ and $\mathbf{x}$, and compute $\varphi(\mathbf{u})$ to obtain and apply a correction to them. $\boldsymbol{T}$ may only need infrequent update, as argued previously. The intensity flow field $\varphi_k(\mathbf{u})$ is defined as the gradient of the measured minus the simulated pixel intensities in a diffraction spot. This essentially directs intensities (i.e. rays of the voxels) to shift towards (u, v, w) regions where there is a lack of intensity, and away from (u, v, w) regions where there is a surplus of intensity. Thus, it helps to eliminate the pixel residual errors on a very local scale. A partial initial overlap between the observed and simulated deformation fields in (u, v, w) is a prerequisite.

4.4. Concept 4: Deformations from collective intensity flow

Similar to gradient intensity flow, but the field $\varphi_k(\mathbf{u})$ is constructed in a way that it aims to completely eliminate the pixel residual errors in a diffraction spot. Suitable flow fields could be determined by employing principles of, e.g. optical flow algorithms, fluid dynamics of a gas flow or machine learning. While such fields would only provide an estimate, we speculate that the consistency of these estimates across multiple diffraction spots may well drive the deformation solution towards the real values.

4.5. Concept 5: Coupling with CP-FEM solvers

Close coupling of the diffraction solver with a crystal plasticity FEM solver may be considered by sharing the same finite element grid or mesh and defining a suitable objective function (Equation (34), Equation (37)). It would need to balance error measures from the diffraction model and the mechanical model of the polycrystalline volume in each iteration. Alternatively, mechanical constraints could be fully enforced in the model. FFT based FEM solvers may be best adapted for the task as they are based on a regular grid (Lebensohn, 2001)[75].

4.6. Concept 6: Sub-grain deformation based on free elements

Rather than a conventional grain representation where diffracting elements are fixed on a regular, space-filling 3D grid, in this concept the diffracting elements of one grain are free to move in (x, y, z) in the sample reference, resulting in three extra degrees of freedom. The grain shape is gradually built up in the iteration from a cloud of elements as their position and orientation converges to the true local orientations. The diffracting power of each element is constant, and their number and local density determines the grain shape and local diffracting powers, hence this degree of freedom is eliminated from the reconstruction problem. The total number of elements to use may be predetermined based on the observed diffraction spot intensities. A figure of merit for an element may be based on completeness (the fraction of detected vs expected (hkl) reflections)

or the local pixel intensity errors where the element projects. New elements may be created based on indexed grain centroids, orientation distribution functions, or near other elements with a high figure of merit, or in a random manner. Elimination of the elements may be based on heuristic rules, e.g. according to their figure of merit and/or after a fixed number of iterations. The elements may be ordered in space relative to one another, while still allowed to change position and orientation, analogous to a rubber or sponge-like object.

The diffraction spots are forward simulated as detailed in Section 2.1. The positions and deformations of the elements are either updated independently using the "intensity flow" concept or in a collective manner like the SIRT/CG based approach. The advantage is that a persistent vector model can be used with simple computation and a high degree of parallelisation, well suited to GPUs. The model avoids treating the diffracting powers separately, and the problem of their inherently ill-posed representation. Regularisation may compensate for the higher degree of freedom and unknowns. A disadvantage is that it is more complicated to consider smoothness and real space gradients of diffracting power, deformation or stresses.

4.7. Concept 7: Grain map reconstruction based on free elements

Following the concept of free elements, and accounting for orientation only and no strain, entire 3D grain maps could potentially be reconstructed simultaneously. As a first step, the entire recorded (u, v, w) image stack (typically 7200 images with 2048x2048 pixels, 60GB at 16bit integer representation) is thresholded to a binary stack to segment the diffraction signal and zero the background noise. A 3D Euclidean distance transform is computed for each pixel in (u, v, w) to obtain its distance from the nearest segmented diffraction spot, which results in a map of identical size to the raw image stack. The map is zero inside the diffraction spots. A pixel value in this map can be seen as an energy component for an element that projects there, with the analogy that the total energy of any element should be zero at the true orientation solution. The negative (u, v, w) gradient of this distance map is then computed, resulting in a field that points towards the nearest active pixel (segmented diffraction spot) at every (u, v, w) pixel in the image stack. This gradient map is used as the intensity flow $\varphi(\mathbf{u})$ and is not changed in the iteration.

Using the product of pseudoinverse $\boldsymbol{T}$ (which here excludes strain) and $\varphi(\mathbf{u})$, a correction of position and orientation of a free element can be computed directly to improve its fit to the nearest observed diffraction spots, even if the spots are actually far in (u, v, w). If most of the closest diffraction spots belong to the same grain, then even a single or just a few of such corrections should be sufficient to shift the element to the true grain position and orientation. We speculate that grain shapes would be reproduced with this approach as the elements settle in a "low energy" state. Intragranular information probably cannot be inferred in 3D accurately using the binary signal.

The elements can be updated independently and the diffraction signal is not simulated, which offers fast parallel computing with no random memory writes. The convergence rate is expected to scale with the sparsity of diffraction spots, as the orientation and real space need less dense initial (random) sampling. The initial knowledge of orientations present in the sample, e.g. from indexing or an orientation distribution reconstruction from far-field diffraction data (Barton & Bernier, 2012;

Kazantsev et al., 2009; Schmidt et al., 2011)[76, 14, 20] would greatly help convergence. A sufficient number of elements for a detailed map, each having their individual $\boldsymbol{T}$ matrices, would require 100s of GB of RAM, which is available in state-of-the-art desktop computers. Furthermore, sub-regions of the sample can be treated independently. The adaptive orientation mapping algorithm by Li et al. for a 2D section (Li & Suter, 2013)[48] provides reliable grain maps and is somewhat similar to this concept.

4.8. Concept 8: Grain and deformation map based on free elements

Concepts 6 and 7 would naturally combine and a compound $\varphi(\mathbf{u})$ flow field (energy gradient field) could be defined over the entire detector space. The field $\varphi(\mathbf{u})$ would be based on the negative gradient of the distance map where the measured diffraction signal is zero, and on the difference between observed and forward simulated intensities where the measured diffraction signal is larger than zero (these regions would need to be updated in each iteration). Although there is no proof or guarantee for convergence, this theoretical approach creates a consistent framework for inferring the local orientation, strain state and diffracting power over the entire 3D sample volume without an indexing step. Bypassing the indexing has the advantage that significant spot overlaps, twins, and sub-grains might be handled adequately. The approach appears to be within reach with regard to processing power and RAM available in a small computer cluster.

4.9. Concept 9: Sliding interval time-resolved scans

The single-axis scanning procedure in DCT has the unique advantage that a series of w rotational positions represent a linear time series, and a 3D reconstruction from a set of images over an w range represents the mean deformation state in the corresponding time window. By continuing scanning several times around 360°, and performing reconstructions from the images within a sliding time window, the 3D deformation fields can be obtained as a function of time in a very effective way with any of the above reconstruction methods, maximising time resolution. The algorithm would take the reconstructed grain map and deformation field from the previous time window as the initial state and refine that result by excluding the first w frame and including the latest frame in the input data. This, of course, assumes sufficiently slow changes in the sample, so that the input data under any time window is consistent enough for reconstruction. It probably also requires active control of the sample positioning during acquisition and additional data processing steps to ensure that the same gauge volume is being scanned and any sample drifts are tracked or corrected accurately. If the sample drifts are known accurately, their effects are straight forward to include in the forward projection model.

5. Experimental

5.1. Material - Gum Metal under tensile load

For testing the model and the ITF solver at considerable strain levels, DCT scans were performed on an annealed polycrystalline Gum Metal sample with a composition of Ti-36Nb-2Ta-3Zr-0.3O wt% and mean grain diameter of 61μm under uniaxial tensile load. Gum Metal is a family of beta-Ti alloys, with a body-centred cubic (bcc) lattice, which exhibit superelasticity, and

can sustain exceptional elastic elongation well beyond 2% nominal strain, due to its low elastic modulus and high yield strength (Kamimura et al., 2016)[77]. Its mechanical behaviour is strongly influenced by the low value of its shear modulus $C' = (C_{11} - C_{12})/2$ (Furuta et al., 2013)[78], and it can undergo a reversible stress-induced martensitic phase transformation (Talling et al., 2009)[79]. The lattice planes in single and polycrystals of the alloy of Ti-36Nb-2Ta-3Zr-0.3O wt% composition exhibit linear elastic behaviour up to $\sim 0.7\,\%$ uniaxial strain (350...450 MPa) (Hara et al., 2009; Talling et al., 2008)[80, 81] beyond which the elastic behaviour is progressively non-linear. The specimen had a strong {110} texture in the loading direction (Fig. 10).

5.2. DCT acquisition parameters

The dog bone shaped sample was prepared by spark cutting from a 3 mm rod, and had a rectangular cross-section of $\sim 540 \times 570\,\mu$m at the gauge volume. The sample was mounted into a small tensile device (Gueninchault et al., 2016)[82], in which the gauge section could be irradiated with an X-ray beam around 360° perpendicular to the loading axis through its glass walls. The device was mounted on the rotation stage of a diffractometer, with the loading and the rotation axes aligned vertical. Two identical DCT scans were recorded at different load levels: 1) a low load of ∼34 MPa was exerted to stabilise the sample in the strain device; 2) a high load of ∼345 MPa was applied near the end of the linear elastic regime of the material. The tensile force was determined by a strain gauge integrated into the tensile device, and calibrated to ∼0.1 N accuracy. The scans were not started for several minutes after applying the load, during which the force showed some relaxation. The vertical position of the sample was adjusted before the high load scan to ensure that approximately the same volume was scanned in both cases.

The specimen was scanned using a quasi-parallel monochromatic synchrotron beam of 40 keV energy and $\frac{\Delta E}{E} \simeq 10^{-3}$ relative energy bandwidth from an in-vacuum undulator and a double bent silicon crystal Laue monochromator. The beam was collimated to about 1×1 mm area inserting a series of compound refractive lenses in the optics hutch located 60 m from the experiment (Vaughan et al., 2011)[83]. The scan consisted of a continuous rotation through an angular interval of $\omega_{step} = 0.05°$ for each image (angular step size), integrating the diffraction signal for 1.5 sec per image (exposure time), which resulted in 7200 images over a 360° rotation. To allow for the detector read-out time, the rotation stage was rotated back to the correct starting position for each image, so that gaps in the integration were avoided. Including this regular back rotation, the total scan time was 5h. Had a state-of-the-art sensor been used with negligible read-out time, the scan would have taken 3h – the total net exposure time. The detector consisted of a transparent luminescent screen (a scintillator crystal), a 10x microscopy objective, a mirror and a Frelon sensor, providing 2048×2048 pixels and an effective pixel size of 1.4 μm in the recorded images. The rotation axis to detector distance was 7 mm. A rectangular beam stop, slightly larger than the direct beam footprint, was placed in front of the scintillator to absorb the direct beam and reduce background scatter noise in the dark field area.

5.3. Data processing algorithm, solver parameters

5.3.1. Indexing and grain average properties

The image stack was preprocessed, the diffraction spots segmented and the grains indexed according to the procedure described in (Reischig et al., 2013)[29]. The setup geometry parameters and the mean position, orientation and strain components of all indexed grains were fitted simultaneously in an iterative routine optimising the least squares deviation in the (u, v, w) spot centroid positions (Reischig & Ludwig, 2019)[31]. With the setup parameters fixed, the centroid position, mean orientation and mean strain state (altogether 12 parameters) of each grain were refitted in a simple robust fit using Siegel's repeated median method (Siegel, 1982)[84] to eliminate the effect of outliers due to spot overlap, thus providing an improved estimate. Outlier diffraction spots were identified as having a (u, v, w) deviation from their simulated centroid position beyond twice the median error. These spots were excluded from the local deformation and shape analysis. Grains with less than 15 remaining diffraction spots or with scattering vectors that were all coplanar (in such case the full strain tensor cannot be inferred) were discarded in the local deformation analysis.

5.3.2. Shape reconstruction

The grain median orientations and strain tensors were used as the initial reference state for the SIRT-based ITF deformation solver described in Section 3.3. The solver was run independently on each grain. The shape and deformation reconstructions were separate and interlaced using $I_{def} = 100$, $I_{shape} = 10$ and $I_{real} = 20$ number of cycles. The shape reconstruction grid had a spacing of 1.4 μm, the same as the detector pixel size. The 2D diffraction spots, integrated in w, were used as projections. The intensity distribution function t_n assigned all intensity to the nearest pixel in (u, v), rather than the four nearest neighbours, for speed. The objective function of the SIRT solver in the shape reconstruction was based on the pixel intensities only (Equation (40)). A smoothing operation was performed using a 3D Gaussian filter over a $3 \times 3 \times 3$ neighbourhood with a standard deviation of one voxel. It was followed by morphological operations on the binary shape: 1) filling in enclosed holes inside the grain volume; 2) erosion and dilation of 1 voxel over the 26 nearest neighbours; 3) any unconnected regions other than the one that contains the volume centroid was removed. The shape reconstruction loop was stopped early if the number of binary voxels that changed versus the previous step was smaller than 0.5% of the volume. At the beginning of each shape reconstruction cycle, the reconstruction envelope was the previous grain volume dilated with 5 voxels.

5.3.3. Deformation reconstruction

The deformation reconstruction grid had a spacing of 5 μm, which seemed to suit the intensity variations in the 3D diffraction spots. The intensity distribution function described in Equation (19) and a point spread function of Gaussian shape with 1.5 pixels standard deviation over a 11×11 pixel (u, v) region was used. The objective function of the SIRT solver was based on the pixel intensities and the deviation of the deformation components from the median grain values, as in Equation (39). A smoothing 3D mean filter (box filter) was applied to the deformation field over the active voxels in a $3 \times 3 \times 3$ neighbourhood, and the result combined the filtered and the unfiltered solution to provide a smoother deformation gradient, with 5% and 95% contribution,

respectively. The $\partial\mathbf{u}/\partial\mathbf{d}$ derivatives were recomputed at every 10 iterations. $I_{main} = 5000$ main iterations were used, and one sub-iteration ($I_{sub} = 1$), i.e. in this case there was no difference between main and sub-iteration, and the forward projection was always performed without linear approximation. No additional stopping criterion was enabled. The backprojection correction contribution to a deformation component from each reflection was limited to $\pm 1 \times 10^{-4}$, and the total correction from all reflections to $\pm 5 \times 10^{-4}$ in each step. The individual grain results were combined into a grain map, with the overlaps removed, but no space-filling or dilation operation was performed. All strain values were corrected retrospectively with an offset in hydrostatic strain to compensate for the originally inaccurate nominal lattice parameter and X-ray wavelength. The grain and deformation maps presented here were not treated any further.

5.3.4. Implementation

The deformation solver has been implemented in the MATLAB environment (version R2017a, MathWorks, 2017), adapted to the existing DCT MATLAB library (Ludwig et al., `https://sourceforge.net/projects/dct/`), with a highly optimised MATLAB code that was compiled for execution on a Linux platform. The code makes no use of GPU-s, but utilises the built-in CPU multithreading of Matlab. The compiled code was run on the computer cluster of the ESRF, where grains were processed independently using 4 processor cores each. The cluster computers have 16...28 Intel Xeon E5-2680 processor cores each, running multiple jobs simultaneously. The execution used 160 cores in total, and the execution time was approximately 24 hours for each of the low load and the high load data set containing ∼1430 grains. The memory usage of the code is fairly lean. The active voxel positions and deformation components of a grain, in the sample reference, are stored as vectors of type 64-bit floating point. The peak shift derivatives $\partial\mathbf{u}/\partial\mathbf{d}$, indices of the 8 nearest neighbours and 6 interpolation coefficients for each voxel and each diffraction spot are also stored as vectors or (non-sparse) arrays throughout the iteration. The observed segmented and the simulated diffraction spots are stored as full 3D volumes of the same size, with a zero padding of 2 pixels in (u, v, w). Any forward simulated intensity that would fall outside the volume is accumulated on the edges of the volume.

6. Results

6.1. Observed reflections

The maximum observable 2θ angle for the experiment described here was $\sim 11.5^\circ$ at the edges of the detector, and $\sim 16^\circ$ in the detector corners, w.r.t. the sample centroid. The observed diffraction spots belonged to the first three lattice plane families: $\{110\}, \{200\}, \{211\}$ and occasionally to $\{220\}$. The maximum theoretically observable reflections during the 360° scan is 24, 12, 48, respectively, ignoring the limitation in the observable Bragg angle. The 3D diffraction spots of the first two families typically had enough signal-to-noise ratio to exhibit visually smooth gradients, while the third and fourth family appear noisy and much less smooth. The diffraction spots selected automatically for analysis are mostly free from large overlaps, although smaller overlaps are fairly common from small grains or sub-grains.

The scanned regions of the sample in the two scans were found to be offset vertically by 16 μm ($\sim$ 11.5 voxels). The reconstructed regions were both 406 voxels in Z (along the rotation/loading axis) and $\sim$ 420 voxels laterally (Fig. 23). The number of grains that were suitable for local deformation analysis was nearly the same, 1428 in the low load and 1437 in the high load data set. The number of active diffraction spots per grain available as input after outlier rejection for the local deformation analysis was rather low: between 20 and 35 for most of the grains (Fig. 8). The standard deviation of the discrepancy between the forward simulated and observed diffraction spot centroids were typically within one pixel in (u, v) and well within half an image in w (Fig. 23, Fig. 9).

The 3D intensity distribution in the observed diffraction spots appear smooth, continuous and connected. For grains with a small error, the resolved deformation fields reproduce most of the features and spatial frequencies that are present in the observed diffraction spots: intensity gradients, ridges, dips, valleys, holes, etc., which suggests that the deformation and diffraction model and its spatial accuracy is suitable (Fig. 6). Some diffraction spots exhibit extended "tails" in w, where only a small fraction of the grain volume diffracts, but which are still connected to the rest of the intensity cloud. These come from regions in the grain which have a distinct deformation state, although still connected to the majority of the volume via smooth deformation gradients. Although less relevant to this data set, we note that twins, subgrains and neighbours with a small-angle grain boundary which share a significant fraction of the reflections with the parent grain may be missed by the current indexing procedure, thus may not be reconstructed.

6.2. Deformation sensitivity

The deformation sensitivity χ (Equation (21)) and peak deformation sensitivity χ^+ (Equation (22)) to the orientation and strain tensor components in the sample reference were computed for each grain from its reflections used in the local deformation analysis. All the grain sensitivities were then combined into one mean value per deformation component, which refers to the entire data set and the specific experimental setup (Fig. 7). This mean sensitivity is in the range of $1.5...3 \times 10^{-3}$, for at least one (u, v, w) component, for each strain tensor component. The mean peak sensitivity is under 10^{-3}, for at least one (u, v, w) component, for each strain tensor component. These results indicate that inferring the deformation components at an accuracy in the order of 10^{-4} is theoretically feasible when fitting a high number of diffraction spots, if the simulated diffraction spot intensities at the solution match closely with the observed distributions. Regarding misorientation, the Rodrigues vector components around the X and Y axes have the highest mean peak sensitivity of 2.7×10^{-4} (5.4×10^{-4} rad, approximately double in radians), and it is w.r.t. ω. The misorientation Rodrigues vector component around the Z axis has the highest mean sensitivity w.r.t. ω of 8.7×10^{-4} (1.74×10^{-3} rad), the same as its peak sensitivity, which equals 0.05°, the rotational step interval ω_{step}. This is expected, as the step size in the ω rotation is a direct measure of the Z rotational direction of a plane normal.

6.3. Errors

The total absolute error in the pixel intensities of a diffraction spot (the $L1$ norm), normalised by the measured integrated intensity of the diffraction spot was averaged across all reflections

and all grains (yielding the sample mean of the $L1$ norm), and monitored during the iterations (Section 11 and Fig. 11). The results are plotted for all grains, as well as a smaller selection of grains which had an error with a mean $L1$ norm less than 0.6, i.e. a more reliable deformation solution. A monotonic decrease is visible in the combined $L1$ norm, and a steady increase in the pixel hit rate of diffraction spots. The larger diffraction spots have a significant halo around them, and often extended "tails" in ω, which is why the pixel hit rate may not go over 80...85%. The voxel hit rate increases only a few per cent, and plateaus after a small decline at ~ 1000 iterations. It is probably due to a significant number of weak diffraction spots that were tightly segmented from the background noise, hence some of the rays may hit empty pixels, even if projecting into the correct pixel. The combined error curve still shows some improvement at 5000 iterations, and it was not stabilised in a minority of the grains, which show good potential for reducing errors in further iterations.

The distribution of the number of indexed reflections and of the active reflections available per grain for deformation analysis are even across the cross-section. The following figures of merit were quantified to indicate the quality of the deformation solution for each grain and the ensemble of all grains (Section 11 and Fig. 11): mean $L1$ norm of the pixel intensity errors normalised with the total diffraction spot intensities, median voxel hit rate (see Section 3.3), median pixel hit rate (see Section 3.3), median deviation of measured and simulated ω spread. These quantities offer a way to classify the grains and relax the need of a manual evaluation of a large number of grains in a data set when optimising the solver parameters or validating the results. They seem to correlate well with each other and all indicate significantly higher errors in the grains on or close to the sample surface (Figs. 14 and 15). As apparent from the diffraction spots, the surface grains are much more deformed already in the low load state. Based on a visual comparison between observed and simulated diffraction spot intensities in the current results, the grains can be classified in the following groups according to their mean $L1$ norm of the pixel intensity error (e_{L1}) with the following approximate ranges:

$e_{L1} < 0.5$: good resemblance with nearly all features reproduced, mismatch in the tails with an error $w \leq 1$;

$e_{L1} < 0.6$: good resemblance for most of the volume, significant mismatch in smaller regions;

$e_{L1} < 0.8$: main features (lower spatial frequencies) reproduced, significant local differences;

$e_{L1} < 1$: variable resemblance, unreliable results;

$e_{L1} > 1$: main trends captured, local results not to be trusted.

The reconstructed grain maps are nearly 100% space filling with only a few grains in the bulk that did not qualify for deformation analysis. Most grain shapes look realistic, concave grain boundaries are reconstructed well, and the maps from the two load states match closely. The grain volumes tend to slightly overlap when assembled in the map. The thickness of the overlapping regions along the grain boundaries is typically 1...2 voxels (1.4...2.8 μm), occasionally 3 or 4. Half of the mean overlap thickness (roughly $\sim$1 voxel or $\sim 1.5\,\mu m$) can be regarded as the actual deviation from an expected grain boundary location, i.e. the spatial resolution of the measurement. In a small

number of cases protrusions from the grains are visible, and more frequent in the surface grains. These are most probably due to overlaps in the diffraction spots. As the surface grains are more spread out in w, there is a higher chance for an overlap to be included in the 2D spot integrated across w that is used for shape reconstruction.

6.4. Deformation field

A horizontal $X-Y$ slice of the 3D strain maps reconstructed by the ITF solver is shown in Fig. 17, which shows a realistic and reasonable strain distribution. The quantitative validation of the local deformation is not possible from this experiment. A quantitative assessment here is restricted to a comparison of the grain average strain values of the local fields with the grain average values fitted from the diffraction spot centroids, and of the overall elastic behaviour.

The mean of the local strain tensor components (all in the sample reference frame) in the low load ($\bar{\boldsymbol{\epsilon}}_{low}$) and high load ($\bar{\boldsymbol{\epsilon}}_{high}$) data sets of all voxels reconstructed with the ITF solver:

$$\bar{\boldsymbol{\epsilon}}_{low} = \begin{pmatrix} -1.39 & -0.06 & -0.12 \\ -0.06 & -2.69 & 0.04 \\ -0.12 & 0.04 & 1.8 \end{pmatrix} \times 10^{-4}\,, \tag{49}$$

$$\bar{\boldsymbol{\epsilon}}_{high} = \begin{pmatrix} -16.37 & -0.86 & -0.61 \\ -0.86 & -18.75 & 0.84 \\ -0.61 & 0.84 & 52.73 \end{pmatrix} \times 10^{-4}\,, \tag{50}$$

and their difference:

$$\bar{\boldsymbol{\epsilon}}_{high} - \bar{\boldsymbol{\epsilon}}_{low} = \begin{pmatrix} -14.89 & -0.80 & -0.49 \\ -0.80 & -16.06 & 0.79 \\ -0.49 & 0.79 & 50.93 \end{pmatrix} \times 10^{-4}\,. \tag{51}$$

The elongations in the normal directions correspond to a Poisson's ratio of 0.305 and a Young's modulus of 61.1GPa of the polycrystal aggregate, as computed from the difference in the external tensile forces.

From the diffraction spot centroids, the difference between the mean of all grain median strain tensors in the low load and high load data sets:

$$\bar{\boldsymbol{\epsilon}}^{cent}_{high} - \bar{\boldsymbol{\epsilon}}^{cent}_{low} = \begin{pmatrix} -16.12 & -0.82 & -0.59 \\ -0.82 & -16.50 & 0.48 \\ -0.59 & 0.48 & 51.47 \end{pmatrix} \times 10^{-4}\,, \tag{52}$$

where the elongations in the normal directions correspond to a Poisson's ratio of 0.317 and a Young's modulus of 60.4 GPa of the polycrystal aggregate.

Recalling that the specimen has a strong {110} texture, the two results compare very well with the Young's modulus measured for this alloy family in a single crystal tensile test in the $<110>$ direction: 60 GPa measured, $\sim$63 GPa calculated (Takesue et al., 2009) [85].

The histograms of the strain components from the centroids at the grain level (Fig. 12) and from the voxels at the sub-grain level (Fig. 13) both show the same expected behaviour from low to

high load: a widening of the distributions, and the Poisson effect. The plots include all measured grains and voxels, including those in which large errors are probable.

The mean values of the reconstructed local orientation and strain tensors were computed for each grain, and the local intragranular deviations from the mean were analysed in the sample reference frame (Fig. 16 and Fig. 18). Both the misorientation and the intragranular strain deviations are in the order of a few times 10^{-4} in the solution. The measured misorientation angle from the grain mean is typically within $\pm 10^{-3}$ rad (Fig. 19). The local misorientation around the Z loading axis, as opposed to X and Y, shows a wider intragranular distribution for surface grains at low load, and a larger change for all grains going from low to high load with no obvious clockwise or anticlockwise preference (Fig. 16). The intragranular deviations of the strain values increase from low to high load but remain small compared to the absolute values shown in Fig. 17 and Fig. 20. Strain components $\boldsymbol{\epsilon}_{XX}$ and $\boldsymbol{\epsilon}_{YY}$ show the largest deviations, while the deviations of components $\boldsymbol{\epsilon}_{ZZ}$ are within $\pm 1.5 \times 10^{-4}$. These results, where the Z loading axis shows distinctly different behaviour in local deviations compared to the lateral directions, may be due to a texture effect, or to an unwanted tendency of the deformation solver to suppress deviations in the $\boldsymbol{\epsilon}_{ZZ}$ components.

7. Discussion

7.1. Deformation solution and accuracy

The geometry calibration using the diffraction pattern of the sample itself provided sub-pixel accuracy and a Young's modulus close to the value reported in the literature. This is a prerequisite to also enable sub-pixel precision in the local deformation solver. The parameters of the solver were not fully optimised, and it appears that the solution could benefit from fine tuning of the settings. Reliable shape reconstructions would normally require at least 15...20 diffraction spots per grain, so for inferring deformation information in addition, the number of diffraction spots with a high signal-to-noise ratio in the current data sets is very low, and possibly a major limitation. This is in part due to the high self-absorption in the specimen. The weak diffraction spots often blend into the background, and their boundaries and intensity gradients are largely influenced by noise rather than the diffraction signal. Such spots, when numerous, break the consistency of the data and may significantly mislead the solver, at least locally.

It may be critical for the initial convergence of the solver that the grain average orientations and strains are known, as this assures that there is an overlap between the measured and the initial simulated state both in solution and in detector space. Since the deformation field is continuous, this overlapping region does exist and can start driving the solution towards the real values. On the other hand, when the initial deformation in the iteration is all zero, then, in a general case, there may not be an overlap between observed and measured spots. Given a parallel X-ray beam, a constant deformation field results in flat diffraction spots in (u, v), i.e. the voxels project into the same constant w. This flat profile may not be overlapping with the observed 3D spot in (u, v, w), if they are far from each other in w due to a large discrepancy in the initial deformation state. In order to interpret the deformation results, it is important to consider the deformation sensitivity of the setup (Fig. 7), which is approximately $1...2.5 \times 10^{-3}$. Those few diffraction spots per grain that provide the peak (highest) deformation sensitivity ($3...10 \times 10^{-4}$) were often fitted less well in

grains that exhibited higher deformations, i.e. the solver with the current settings failed to fully exploit the information in these reflections. It would be crucial for the solver to fit such reflections better in order to maximise the local deformation accuracy.

We conclude that the deformation results should be viewed as a possible solution to the measured data rather than the real solution. The deformation results obtained here are supposed to approach the minimum norm solution in terms of deviations from the robust grain average. The relatively low setup sensitivity, with potential inaccuracies of up to $1...2.5 \times 10^{-3}$, means that the setup is blind to deformation fields that are much below this limit and are practically in the null-space of the mapping operation. In other words, an error in one deformation component in the order of 10^{-4} would be compensated by the others with a similar magnitude, and most of the resulting deviations in (u, v, w) could still be below one pixel or image. From another perspective, a small deviation in the reconstructed diffraction spots translate into a relatively large error in some deformation components. In terms of the linear problem in Equation (29) this means that more equations, i.e. more active pixels in more detailed diffraction spots, are required to find a unique solution. One way to realise this is using a smaller angular step size.

In summary, the results demonstrate that: 1) the diffraction model can provide sufficient fidelity in reproducing the signal; 2) convergence can be realised by an iterative solver; 3) most of the observed diffraction spots can be reproduced to a high degree with a physically meaningful deformation field; 4) the implementation is efficient and feasible; 5) the grain average of the local deformation fields are reliable.

By adapting the acquisition parameters and possibly the diffraction model and solver, we expect that the true deformation fields can be inferred at the level of 10^{-4} – favourable and relevant for numerous applications.

7.2. Potential improvements of the experimental setup

An obvious way of improvement is exposing each image longer for a stronger diffraction signal. It is easily within reach, as the ongoing source upgrade at the ESRF will deliver ~ 20 times the current X-ray flux at ID11, i.e. a fraction of the current scanning times. State-of-the-art sCMOS sensors [86] have negligible read-out time and allow for continuous exposure during rotation, avoiding gaps or the need for repositioning before each image. Using smaller angular increments are the most effective way to improve deformation sensitivity, with a consequence of extended exposure times and potentially a need to decrease the photon energy bandwidth accordingly. Sensitivity in most components scales with the detector distance but a larger detector distance means a lower solid angle coverage. A larger detector area (more pixels) is clearly beneficial for detecting more diffraction spots. Positioning the detector laterally on each side of the optical axis for two scans altogether offers another simple way to extend the field of view.

An example of a realistic configuration with much increased orientation and strain resolution for the same measurement could have:

- double the rotation axis to detector distance (14 mm);
- double the sensor size (4096×4096 pixels) for the same angular coverage;

- the same 1.4 μm effective pixel size;
- 10 times smaller angular stepping ω_{step}.

The mean peak deformation sensitivity of such a configuration for the same sample would approach $5...6 \times 10^{-4}$ in the YZ, XZ shear strain components, $1...2 \times 10^{-4}$ in the other strain components, and below 10^{-4} in misorientation (Fig. 7). For the Gum Metal specimen, increasing the photon energy would reduce self-absorption, but its overall effect on the deformation accuracy is not obvious.

For light materials, a setup configuration using lower energies and higher 2θ Bragg angles, e.g. around 90°, can be realised by a horizontal rotation axis and a detector placed above or underneath the axis to account for the synchrotron beam polarisation while still benefiting from the Friedel pair based indexing [87, 29]. Higher Bragg angles increase the sensitivity to the d-spacings (proportionally to $tan(\theta)$), and also the azimuthal orientation sensitivity (which in turn has the adverse effect of increasing the risk that diffraction spots overlap). The higher diffracting power, higher photon flux from the source and higher detection efficiency in the scintillator at lower energies decrease scanning times. On the other hand, reduction of the photon energy would require smaller sample dimensions in order to compensate for the increased attenuation.

There are no obvious ways of optimising the setup geometry purely from theoretic considerations, as the number of irradiated grains, sample mosaicity and the overall background noise should all be considered. The goal of the optimisation should be maximising accuracy in grain boundary locations, local orientations or strains, or minimising total scanning time. The main parameters to be found are: beam height (size of the irradiated volume), beam energy, detector distance, pixel size, ω step size, and the beam energy bandwidth and settings of the X-ray monochromator and focusing optics.

Alternative scanning geometries and procedures can be considered in place of or as a follow-up of a DCT scan, targeting a small number of selected grains within the volume, e.g. using topo-tomography [88] or moving the detector to predicted diffraction spot positions at a much larger distance. If the positioning and calibration can be done with high precision, this could significantly improve the strain and orientation resolution. In terms of the maximum detectable strain level from a hardware perspective, there is no apparent limit other than increasing spot overlaps and diminishing signal-to-noise ratio. We do not expect that large absolute strain values alone would impede the solver, and the maximum elastic lattice strains of 1...2% encountered in metals can probably be resolved. It is the complexity of the strain and misorientation fields that would pose a challenge to the solver. Following plastic deformation of several degrees, the magnitude and complexity of the intragranular misorientation field dominate the projections and it might hinder strain retrieval with the proposed method. More simulation tests and experiments are required to judge the performance of the algorithm at high strains and/or high mosaicity.

The ITF reconstruction approach is a general imaging methodology for extracting complete local deformation tensors by combining several (hkl) reflections, and is adapted to a range of diffraction geometries. A smaller beam cross section naturally yields a better spatial definition of the mapping problem (though typically at the expense of scanning times), which in turn may

improve deformation sensitivity. For example, line beam illumination and collecting diffraction signal at high scattering angles would be an obvious way to increase strain sensitivity and the correlation of detector and sample space. This would be a step closer to conditions in section topography (Reischig et al., 2013)[29]. Appropriate 2D gratings or apertures can create a structured illumination pattern, i.e. an array of pencil beams with line footprints that can be detected simultaneously on an area detector, and much reduce the complexity of the 3D problem [87].

7.3. Potential improvements of the solver

The low signal-to-noise ratio could be compensated by pre-smoothing of the diffraction spots (e.g. by 2D or 3D splines, wavelets, etc.), which could significantly increase the smoothness of the intensity gradients in weak spots and the consistency of the backprojection corrections.

The grain shapes could be improved by a simultaneous reconstruction of the entire sample volume (the global ITF concept in Section 4.1), so that voxels in grain boundary regions are more reliably assigned the correct grain. More precise grain shapes should increase the deformation accuracy, and vice versa. Tails in the intensity distributions most probably originate from grain boundary regions, and their reproducibility would benefit from the whole-sample reconstructions. The deformation fields themselves may also be represented by potentially more effective ways, e.g. by splines or wavelets.

A hierarchic solution approach using gradually finer or adaptive grids in real space and in detector space could also improve robustness and the reproducibility of the intensity tails.

Additional physical effects can potentially be included in the forward model, if they are a continuous (and at least locally differentiable) function of time, real space, orientation and strain.

When overlaps are more prominent, indexing may not be feasible using spot centroids, and a preliminary orientation map may be obtained by the 6D approach [53, 55] or scanning orientation space for each voxel [48]. Such a map may then be refined by the presented methods to infer deformation. Alternatively, the reconstruction approach based on free elements (Section 4.6) may be attempted.

7.4. Verification and applicability

The validity of the presented approach and the alternative approaches should be confirmed with testing on simulated data sets. The robustness, reliability and uniqueness of the deformation solution should be verified. The background noise has a crucial effect on the consistency of the data and the effectiveness of the solver, hence the simulations should include noise that has been previously quantified in real experiments. The fulfilment of local static equilibrium is the most comprehensive way to obtain a figure of merit of the local solutions in real measurements.

The method or its alternative variants are potentially also applicable to single crystals utilising either diffracted beams or extinction contrast in the direct beam in X-ray topography, rocking curve imaging [56, 57] and related methods, as long as kinematical diffraction approximations are at least partially valid. While the complexity of the presented 3D algorithm and its limited spatial and deformation sensitivity may be a disadvantage versus other 3D polycrystal scanning methods using a line or pencil beam, the simple experimental setup and efficient scanning procedure offer major benefits.

8. Conclusions

A theory for the reconstruction of intragranular orientation and strain fields in polycrystalline samples in 3D using a near-field area detector and box beam illumination has been presented. Experimental results from a synchrotron-based X-ray diffraction experiment on a Gum Metal sample demonstrate the feasibility and potential of the proposed approach. A kinematical diffraction model is used in a vector field representation of the local deformations to simulate realistic diffraction spots. The convergence of the proposed non-linear solver using an adapted SIRT algorithm, named Iterative Tensor Field Reconstruction (ITF), was demonstrated, and it found realistic deformation solutions that were consistent with the expected elastic behaviour at the grain level. The solver employs Tikhonov regularisation and enforces smooth deformation gradients. The applied acquisition parameters limited the deformation sensitivity to $1...2 \times 10^{-3}$, and the number of available diffraction spots with sufficient signal-to-noise ratio was also a limiting factor.

Quantitative means and aspects of the data analysis and validation have been described. The study suggests that all necessary theoretical, experimental and algorithmic tools are available to resolve the strain fields from near-field diffraction images at an accuracy in the order of 10^{-4}, or the equivalent stress fields in the order of tens of MPa. Several improvements to the experimental setup and the solver are possible. A near-field detector with a pixel size of $1...2\,\mu$m and fine rotational stepping (in the range of $0.005...0.01^{\circ}$) in ω can provide adequate strain resolution. Scanning times can be in the order of hours or possibly minutes, depending on the specimen. Calibration of the near field setup is achievable from the data set itself or by scanning a calibration standard.

The model and solver algorithm allows for directly applying constraints of static equilibrium in the optimisation or coupling with CP-FEM solvers, if the single crystal elastic moduli of the material are known. With an optimised implementation, the computations can potentially be performed in a single computer within a day. A range of alternative ways of inferring the sub-grain orientation and deformation fields have been proposed, including indexing-based grain-by-grain and indexing-free methods. A quantitative validation of the local deformation solution requires simulation studies, evaluation of stress equilibrium or comparison to alternative scanning techniques, such as line and pencil beam scanning.

9. Supplementary material

Diffraction spots
(dct1_grain_*.avi)

The video files show all segmented 3D diffraction spots that were used for deformation reconstruction in the high load data set for selected grains, stacked along the w dimension. The measured intensities are on the left, the simulated equivalent is on the right. The 2D diffraction spots integrated along w are also shown in separate videos. One pixel in the video files corresponds to one detector pixel. The grey scale colour limits were set individually for each diffraction spot. Occasional overlaps from other diffraction spots are visible in the observed images.

3D map of strain components at high load
(dct1_absolute_strain.avi)

Video showing consecutive X-Y slices of the 3D strain maps of the high load data set reconstructed by the ITF solver. The RGB colours correspond to the strain scale in Fig. 17. From left to right, the order of the strain components is: ϵ_{xx}, ϵ_{yy}, ϵ_{zz} in the top row; ϵ_{yz}, ϵ_{xz}, ϵ_{xy} in the bottom row.

3D map of strain deviations from the grain mean (dct1_strain_deviation_from_grain_mean.avi)

Video showing consecutive X-Y slices of the 3D map of strain deviations from the grain mean of the high load data set reconstructed by the ITF solver. The RGB colours correspond to the strain scale in Fig. 18. From left to right, the order of the strain components is: ϵ_{xx}, ϵ_{yy}, ϵ_{zz} in the top row; ϵ_{yz}, ϵ_{xz}, ϵ_{xy} in the bottom row.

10. Acknowledgments

The authors would like to thank Nicola Viganò, Dimitris Karkoulis, Andrew King, Max Langer, Jose Baruchel, Jürgen Härtwig, Tilo Baumbach, Jon Wright and Shigeru Kuramoto for their input, support and fruitful discussions during the course of this study, and the ESRF for providing beamtime on beamline ID11. The authors would furthermore like to thank the reviewers for their careful reading and suggestions for improvement of the manuscript.

11. Figures

Appendix A. Crystallographic phase as an undeformed reference

The list of theoretical (hkl) reflections of the reference crystal phase can be obtained by, for example, computing the structure factors F_{hkl} (see [62]) for all (hkl) combinations from the atomic positions in the unit cell, and retaining those (hkl)-s for which the structure factor is non-zero and the Bragg angle is within the range covered by the experimental setup. Metal crystal lattices often exhibit one of the few common hexagonal or cubic crystallographic spacegroups with a known list of reflections. Three Cartesian coordinate reference frames are used in the processing: the crystal reference (also referred to as "grain" reference), the sample and the laboratory reference. The laboratory reference is fixed to the incident X-ray beam direction and the rotation axis direction. The sample reference is fixed to and rotates with the rotation table, and corresponds to the lab reference at $\omega = 0$ rotational position. The crystal reference frame is rotated in relation to the sample reference according to the grain orientation. Local misorientation and strain are defined in relation to an undeformed (stress free) crystal lattice, referred to as the reference lattice. The unit cells of the undeformed reference lattice is aligned with the crystal reference frame according to a suitable convention. For cubic lattices, we use the common convention that the cubic unit cell is aligned with the crystal reference. For a given (hkl) reflection, its corresponding scattering vector or plane normal $\mathbf{n}^b$ in direct space in the Cartesian crystal reference can be obtained via the reciprocal basis matrix $\boldsymbol{B}$ as described in [13]. The matrix $\boldsymbol{B}^0$ here refers to the unit cell of the undeformed reference crystal lattice, and it is a function of the lattice parameters $(a, b, c, \alpha, \beta, \gamma)$.

$$\mathbf{n}^b = \boldsymbol{B}^0 \begin{pmatrix} h \\ k \\ l \end{pmatrix} . \tag{A.1}$$

The d-spacing of this lattice plane in the undeformed reference state (|.| denotes the Euclidean vector norm)

$$\delta^0 = \frac{1}{|\mathbf{n}^b|} . \tag{A.2}$$

The corresponding Bragg angle θ^0 in the undeformed state considering the first harmonic of the reflection from Bragg's law:

$$\sin\theta^0 = \frac{\lambda}{2\delta^0} \qquad \lambda = \frac{hc}{E} . \tag{A.3}$$

where λ is the wavelength and E is the photon energy of the incident and diffracted X-ray beams, h is Planck's constant, c is speed of light. The unit plane normal of the reflection in the Cartesian crystal reference frame in an undeformed state

$$\mathbf{n}^c = \frac{\mathbf{n}^b}{|\mathbf{n}^b|} \tag{A.4}$$

The unit plane normal in an undeformed state with its coordinates in the sample reference frame

$$\mathbf{n}^0 = \boldsymbol{U}(\mathbf{r}^0)\, \mathbf{n}^c \tag{A.5}$$

where $\boldsymbol{U}^0$ is a rotation tensor representing crystal orientation, and it is computed from a 3D Rodrigues vector $\mathbf{r}^0$ that uniquely describes grain orientation, similar to Euler angles. As crystal symmetry is taken into account by the indexing procedure beforehand, $\mathbf{r}^0$ falls within the fundamental zone of Rodrigues space.

Appendix B. Representation of the deformation field

A set of plane normals $\mathbf{n}^0$ and their corresponding d-spacings δ^0, one from each indexed diffraction spot, serve as a basic input for the deformation solver. Having obtained this input upstream in the processing (see [29, 31]), the underlying crystallography is irrelevant as Bragg's law and the principles of solid mechanics prevail. The initial $\mathbf{n}^0$ values for the strain retrieval already describe a deformed state of the lattice (the *initial* state), with an initial strain tensor $\boldsymbol{\epsilon}^0$ (the mean grain strain). $\boldsymbol{\epsilon}^0$ is determined upstream in the processing from the diffraction spot centroids along with each plane normal $\mathbf{n}^0$. With a vector $\mathbf{v}^c$ indicating an arbitrary direction in the lattice

$$\mathbf{v}^0 = \boldsymbol{\epsilon}^0\, \boldsymbol{U}^0\, \mathbf{v}^c . \tag{B.1}$$

Note that this matrix product with the strain tensor does not apply directly to a plane normal, as it is not fixed to real material points: $\mathbf{n}^0 \neq \boldsymbol{\epsilon}^0 \boldsymbol{U}^0 \mathbf{n}^c$. Also note that all strain tensors and the deformation gradient tensor in the this description include the identity matrix.

The following relations are applicable to each voxel independently. The nine components $\mathbf{d} = d_m$ of the local deformation gradient tensor $\boldsymbol{D}(\mathbf{d})$ are the unknown parameters sought for a voxel.

They represent a combination of an additional misorientation and strain state relative to the initial grain state $(\boldsymbol{\epsilon}^0, \boldsymbol{U}^0)$. They refer to the mean value over the volume of the voxel, i.e. expected to have the least deviation from the true local values at the voxel centroid.

$$\boldsymbol{D}(\mathbf{d}) = \begin{pmatrix} d_1 + 1 & d_4 & d_7 \\ d_2 & d_5 + 1 & d_8 \\ d_3 & d_6 & d_9 + 1 \end{pmatrix} \tag{B.2}$$

Planes in the continuum remain planes after deformation according to the deformation gradient tensor. Curvature of the lattice cannot be interpreted from $\boldsymbol{D}$ of a single voxel but it is exhibited through a spatial gradient of $\boldsymbol{D}$ across the voxels. In case only misorientation is considered and no strain, the underlying three rotational parameters in the form of Rodrigues vectors (or Euler angles) are used instead of $\mathbf{d}$ (three components instead of nine) and an additional operation is required to generate the misorientation matrix. In a post-processing operation, after running the solver, the inferred $\boldsymbol{D}$ tensor is combined with the initial input strain and orientation tensor according to

$$\mathbf{v} = \boldsymbol{D}\,\boldsymbol{\epsilon}^0\,\boldsymbol{U}^0\,\mathbf{v}^c = (\boldsymbol{\epsilon}_d \boldsymbol{U}_d)\boldsymbol{U}^0\,\mathbf{v}^c \tag{B.3}$$

where $\mathbf{v}$ stands for the vector $\mathbf{v}^c$ in the observed state of the specimen in the sample reference frame. Polar decomposition is used to separate out the symmetric left stretch tensor $\boldsymbol{\epsilon_d}$ (left Cauchy-Green deformation tensor), so that the initial mean orientation and the local misorientation tensors can be unified into one orientation tensor $\boldsymbol{U} = \boldsymbol{U}_d\,\boldsymbol{U}^0$ (that is an orthogonal rotation matrix):

$$\boldsymbol{\epsilon}_d\,\boldsymbol{U}_d = \boldsymbol{D}\,\boldsymbol{\epsilon}^0\,. \tag{B.4}$$

It is common to have an uncertainty in the hydrostatic strain component due to an inaccuracy in the photon energy of the X-ray beam or the scaling of the unit cell parameters. These two discrepancies have the exact same effect on diffraction through Bragg's law, and they are indistinguishable. A hydrostatic strain correction $\boldsymbol{\epsilon}_{hyd}$ can be applied retrospectively and directly to the results from the solver. The final local orientation matrix $\boldsymbol{U}$ and strain tensor $\boldsymbol{\epsilon} = \boldsymbol{\epsilon}_{hyd}\,\boldsymbol{\epsilon}_d$ in the sample reference frame, with respect to the reference crystal:

$$\mathbf{v} = \boldsymbol{\epsilon}_{hyd}\,\boldsymbol{\epsilon}_d\,\boldsymbol{U}\,\mathbf{v}^c = \boldsymbol{\epsilon}\,\boldsymbol{U}\,\mathbf{v}^c\,. \tag{B.5}$$

Appendix C. Transformation from sample to crystal reference frame

The strain tensor in the crystal reference $\boldsymbol{\epsilon}^c$, and its inverse transform back to the sample reference:

$$\boldsymbol{\epsilon}^c = \boldsymbol{U}^T\,\boldsymbol{\epsilon}\,\boldsymbol{U} \qquad \boldsymbol{\epsilon} = \boldsymbol{U}\,\boldsymbol{\epsilon}^c\,\boldsymbol{U}^T\,. \tag{C.1}$$

The strain tensor in the crystal reference in Voigt notation and including a factor of 2 for the shear components

$$\boldsymbol{\epsilon}^V = \begin{pmatrix} \boldsymbol{\epsilon}^c_{11} - 1 & \boldsymbol{\epsilon}^c_{22} - 1 & \boldsymbol{\epsilon}^c_{33} - 1 & 2\boldsymbol{\epsilon}^c_{23} & 2\boldsymbol{\epsilon}^c_{13} & 2\boldsymbol{\epsilon}^c_{12} \end{pmatrix}^T\,. \tag{C.2}$$

In case of a linear elastic behaviour, the stress tensor components in the grain reference are obtained in Voigt notation from Hooke's law:

$$\boldsymbol{\sigma}^V = \boldsymbol{C}\,\boldsymbol{\epsilon}^V \tag{C.3}$$

$$\boldsymbol{\sigma}^V = \begin{pmatrix} \boldsymbol{\sigma}^c_{11} & \boldsymbol{\sigma}^c_{22} & \boldsymbol{\sigma}^c_{33} & \boldsymbol{\sigma}^c_{23} & \boldsymbol{\sigma}^c_{13} & \boldsymbol{\sigma}^c_{12} \end{pmatrix}^{\mathrm{T}} \tag{C.4}$$

which allows to construct $\boldsymbol{\sigma}^c$, the stress tensor in the crystal reference. $\boldsymbol{C}$ is the elastic stiffness tensor that contains the single crystal elastic moduli of the material in the grain reference. For example, for a cubic lattice with three distinct elastic moduli (c_{11}, c_{12}, c_{44})

$$\boldsymbol{C} = \begin{pmatrix} c_{11} & c_{12} & c_{12} & 0 & 0 & 0 \\ c_{12} & c_{11} & c_{12} & 0 & 0 & 0 \\ c_{12} & c_{12} & c_{11} & 0 & 0 & 0 \\ 0 & 0 & 0 & c_{44} & 0 & 0 \\ 0 & 0 & 0 & 0 & c_{44} & 0 \\ 0 & 0 & 0 & 0 & 0 & c_{44} \end{pmatrix}. \tag{C.5}$$

The stress tensor in the sample reference

$$\boldsymbol{\sigma} = \boldsymbol{U}\boldsymbol{\sigma}^c\boldsymbol{U}^T \tag{C.6}$$

and in the inverse transform

$$\boldsymbol{\sigma}^c = \boldsymbol{U}^T\boldsymbol{\sigma}\boldsymbol{U}\,. \tag{C.7}$$

The local divergence of the stress tensor field at a voxel j:

$$div(\boldsymbol{\sigma}^j) = \begin{pmatrix} \frac{\partial \boldsymbol{\sigma}^j_{11}}{\partial x} + \frac{\partial \boldsymbol{\sigma}^j_{12}}{\partial y} + \frac{\partial \boldsymbol{\sigma}^j_{13}}{\partial z} \\ \frac{\partial \boldsymbol{\sigma}^j_{21}}{\partial x} + \frac{\partial \boldsymbol{\sigma}^j_{22}}{\partial y} + \frac{\partial \boldsymbol{\sigma}^j_{23}}{\partial z} \\ \frac{\partial \boldsymbol{\sigma}^j_{31}}{\partial x} + \frac{\partial \boldsymbol{\sigma}^j_{32}}{\partial y} + \frac{\partial \boldsymbol{\sigma}^j_{33}}{\partial z} \end{pmatrix} \tag{C.8}$$

which can be approximated as a linear function of the stress components of the neighbouring voxel elements (with the voxel indices on a 3D grid):

$$div(\boldsymbol{\sigma}^{x,y,z}) \simeq \frac{1}{2}\begin{pmatrix} \boldsymbol{\sigma}^{x+1,y,z}_{11} - \boldsymbol{\sigma}^{x-1,y,z}_{11} + \boldsymbol{\sigma}^{x,y+1,z}_{12} - \boldsymbol{\sigma}^{x,y-1,z}_{12} + \boldsymbol{\sigma}^{x,y,z+1}_{13} - \boldsymbol{\sigma}^{x,y,z-1}_{13} \\ \boldsymbol{\sigma}^{x+1,y,z}_{21} - \boldsymbol{\sigma}^{x-1,y,z}_{21} + \boldsymbol{\sigma}^{x,y+1,z}_{22} - \boldsymbol{\sigma}^{x,y-1,z}_{22} + \boldsymbol{\sigma}^{x,y,z+1}_{23} - \boldsymbol{\sigma}^{x,y,z-1}_{23} \\ \boldsymbol{\sigma}^{x+1,y,z}_{31} - \boldsymbol{\sigma}^{x-1,y,z}_{31} + \boldsymbol{\sigma}^{x,y+1,z}_{32} - \boldsymbol{\sigma}^{x,y-1,z}_{32} + \boldsymbol{\sigma}^{x,y,z+1}_{33} - \boldsymbol{\sigma}^{x,y,z-1}_{33} \end{pmatrix}. \tag{C.9}$$

The L2 norm of the divergence as an objective function:

$$\Gamma(\mathbf{d}) = \|div(\boldsymbol{\sigma}(\mathbf{d}))\|_2^2 = \sum_j \left(\left(\frac{\partial \boldsymbol{\sigma}^j_{11}}{\partial x} + \frac{\partial \boldsymbol{\sigma}^j_{12}}{\partial y} + \frac{\partial \boldsymbol{\sigma}^j_{13}}{\partial z} \right)^2 + \left(\frac{\partial \boldsymbol{\sigma}^j_{21}}{\partial x} + \frac{\partial \boldsymbol{\sigma}^j_{22}}{\partial y} + \frac{\partial \boldsymbol{\sigma}^j_{23}}{\partial z} \right)^2 + \left(\frac{\partial \boldsymbol{\sigma}^j_{31}}{\partial x} + \frac{\partial \boldsymbol{\sigma}^j_{32}}{\partial y} + \frac{\partial \boldsymbol{\sigma}^j_{33}}{\partial z} \right)^2 \right). \tag{C.10}$$

Appendix D. Forward projection of diffraction peak positions

A plane normal $\mathbf{n}^0$ of an (hkl) reflection is represented by two arbitrary unit vectors $\mathbf{e}_1$ and $\mathbf{e}_2$, in a way that they form an orthonormal set.

$$\mathbf{n}^0 = \mathbf{e}_1^0 \times \mathbf{e}_2^0 \qquad \mathbf{e}_1^0 \perp \mathbf{e}_2^0 \qquad \left|\mathbf{e}_1^0\right| = 1 \qquad \left|\mathbf{e}_2^0\right| = 1 \tag{D.1}$$

The base vectors in the deformed state:

$$\mathbf{e}_1 = \boldsymbol{D}\,\mathbf{e}_1^0 \qquad \mathbf{e}_2 = \boldsymbol{D}\,\mathbf{e}_2^0\,. \tag{D.2}$$

The unit plane normal in the deformed state (not restricted to small strain theory)

$$\mathbf{n} = \frac{\mathbf{e}_1 \times \mathbf{e}_2}{|\mathbf{e}_1 \times \mathbf{e}_2|}\,. \tag{D.3}$$

The ratio of the d-spacing in the deformed (δ) and undeformed state (δ^0) can be derived by considering a plane P in the undeformed state at unit distance from the origin with plane normal $\mathbf{n}^0$ and unit d-spacing $\delta^0 = 1$. Let A^0 be a material point that lies in P at location $\mathbf{n}^0$. As a result of deformation gradient $\boldsymbol{D}$, A^0 is displaced to $A = \boldsymbol{D}\mathbf{n}^0$, the plane normal of P changes to $\mathbf{n}$, and its d-spacing to δ, where δ is the distance of P from the origin in the deformed state. As the origin has zero displacement, the relative d-spacing (not restricted to small strains)

$$\delta_{rel} = \frac{\delta}{\delta_0} = \mathbf{n}\,\boldsymbol{D}\,\mathbf{n}^0 \tag{D.4}$$

From the relative d-spacing, the sine of the Bragg-angle θ in the deformed state is computed as:

$$\sin\theta = \frac{1}{\delta_{rel}}\sin\theta^0 \tag{D.5}$$

For a given plane normal $\mathbf{n}$ and Bragg angle θ, a maximum of four reflections can be observed during a 360° rotational scan of the sample. The four ω rotation angles of the sample stage where diffraction occurs from $\mathbf{n}$ can be computed from a quadratic equation knowing the incident beam and rotation axis directions (see, for example, Moscicki et al., 2009 [89]):

$$\begin{aligned}
\omega_1 &= \omega_1(\sin\theta, \mathbf{n}, \Omega)\\
\omega_2 &= \omega_2(\sin\theta, \mathbf{n}, \Omega)\\
\omega_3 &= \omega_3(\sin\theta, \mathbf{n}, \Omega)\\
\omega_4 &= \omega_4(\sin\theta, \mathbf{n}, \Omega)
\end{aligned} \tag{D.6}$$

where Ω represents all constant parameters of the setup geometry. The rotation angles w expressed in images, rather than degrees, with ω_{step} being the width of the rotational interval covered by an image:

$$w = \frac{\omega}{\omega_{step}} \tag{D.7}$$

The (u, v) detector pixel coordinates where a ray projects, that was diffracted by a voxel at position $\mathbf{x}^0$ in the sample reference, is computed as the intersection of the diffracted beam path with the detector plane:

$$(u, v, w) = \mathbf{u}(\mathbf{n}, \mathbf{x}^0, \omega, \Omega)\,. \tag{D.8}$$

References

[1] P. A. Shade, W. D. Musinski, M. Obstalecki, D. C. Pagan, A. J. Beaudoin, J. V. Bernier, T. J. Turner, Exploring new links between crystal plasticity models and high-energy X-ray diffraction microscopy, Current Opinion in Solid State and Materials Science 23 (5) (2019) 100763. doi:10.1016/j.cossms.2019.07.002.
URL https://doi.org/10.1016/j.cossms.2019.07.002

[2] M. D. Sangid, Coupling in situ experiments and modeling – Opportunities for data fusion, machine learning, and discovery of emergent behavior, Current Opinion in Solid State and Materials Science (2019). doi:10.1016/j.cossms.2019.100797.

[3] E. Maire, P. J. Withers, Quantitative X-ray tomography (jan 2014). doi:10.1179/1743280413Y.0000000023.

[4] M. A. Sutton, F. Hild, Recent Advances and Perspectives in Digital Image Correlation, Experimental Mechanics 55 (1) (2015) 1–8. doi:10.1007/s11340-015-9991-6.

[5] L. Mao, H. Liu, Y. Zhu, Z. Zhu, R. Guo, F. pen Chiang, 3D strain mapping of opaque materials using an improved digital volumetric speckle photography technique with X-ray microtomography, Applied Sciences (Switzerland) 9 (7) (2019). doi:10.3390/app9071418.

[6] P. J. Withers, P. J. Webster, Neutron and synchrotron X-ray strain scanning, Strain 37 (1) (2001) 19–33. doi:10.1111/j.1475-1305.2001.tb01216.x.

[7] P. Staron, A. Schreyer, H. Clemens, S. Mayer, Neutrons and synchrotron radiation in engineering materials science: From fundamentals to applications: Second edition, Wiley-VCH Verlag GmbH & Co. KGaA, 2017. doi:10.1002/9783527684489.

[8] M. Álvarez-Murga, P. Bleuet, J.-L. Hodeau, Diffraction/scattering computed tomography for three-dimensional characterization of multi-phase crystalline and amorphous materials, Journal of Applied Crystallography 45 (6) (2012) 1109–1124. doi:10.1107/S0021889812041039.
URL http://scripts.iucr.org/cgi-bin/paper?S0021889812041039

[9] J. Hendriks, A. Gregg, C. Wensrich, A. Wills, Implementation of traction constraints in Bragg-edge neutron transmission strain tomography, Strain 55 (5) (oct 2019). doi:10.1111/str.12325.
URL https://onlinelibrary.wiley.com/doi/abs/10.1111/str.12325

[10] A. W. Gregg, J. N. Hendriks, C. M. Wensrich, V. Luzin, A. Wills, Neutron diffraction strain tomography: Demonstration and proof-of-concept, Review of Scientific Instruments 91 (1) (2020). doi:10.1063/1.5120422.
URL https://doi.org/10.1063/1.5120422

[11] W. R. Lionheart, P. J. Withers, Diffraction tomography of strain, Inverse Problems 31 (4) (2015). doi:10.1088/0266-5611/31/4/045005.

[12] E. M. Lauridsen, S. Schmidt, R. M. Suter, H. F. Poulsen, Tracking: A method for structural characterization of grains in powders or polycrystals, Journal of Applied Crystallography 34 (6) (2001) 744–750. doi:10.1107/S0021889801014170.
URL http://scripts.iucr.org/cgi-bin/paper?S0021889801014170

[13] H. F. Poulsen, Three-Dimensional X-Ray Diffraction Microscopy, Springer, 2004.

[14] S. Schmidt, N. F. Gade-Nielsen, M. Høstergaard, B. Dammann, I. G. Kazantsev, High Resolution Orientation Distribution Function, Materials Science Forum 702-703 (2011) 536–539. doi:10.4028/www.scientific.net/MSF.702-703.536.
URL http://www.scientific.net/MSF.702-703.536

[15] H. O. Sørensen, S. Schmidt, J. P. Wright, G. B. Vaughan, S. Techert, E. F. Garman, J. Oddershede, J. Davaasambu, K. S. Paithankar, C. Gundlach, H. F. Poulsen, Multigrain crystallography, Zeitschrift fur Kristallographie 227 (1) (2012) 63–78. doi:10.1524/zkri.2012.1438.

[16] H. Sharma, R. M. Huizenga, S. E. Offerman, A fast methodology to determine the characteristics of thousands of grains using three-dimensional X-ray diffraction. I. Overlapping diffraction peaks and parameters of the experimental setup, Journal of Applied Crystallography 45 (4) (2012) 693–704. doi:10.1107/S0021889812025563.

[17] D. J. Jensen, H. Poulsen, The three dimensional X-ray diffraction technique, Materials Characterization 72 (2012) 1–7. doi:10.1016/j.matchar.2012.07.012.
URL https://linkinghub.elsevier.com/retrieve/pii/S104458031200188X

[18] U. Lienert, S. F. Li, C. M. Hefferan, J. Lind, R. M. Suter, J. V. Bernier, N. R. Barton, M. C. Brandes, M. J. Mills, M. P. Miller, B. Jakobsen, W. Pantleon, High-energy diffraction microscopy at the advanced photon source, JOM 63 (7) (2011) 70–77. doi:10.1007/s11837-011-0116-0.
URL http://link.springer.com/10.1007/s11837-011-0116-0

[19] J. V. Bernier, N. R. Barton, U. Lienert, M. P. Miller, Far-field high-energy diffraction microscopy: A tool for intergranular orientation and strain analysis, Journal of Strain Analysis for Engineering Design 46 (7) (2011) 527–547. doi:10.1177/0309324711405761.

[20] N. R. Barton, J. V. Bernier, A method for intragranular orientation and lattice strain distribution determination, Journal of Applied Crystallography 45 (6) (2012) 1145–1155. doi:10.1107/S0021889812040782.

[21] W. A. Paciorek, M. Meyer, G. Chapuis, On the geometry of a modern imaging diffractometer, Acta Crystallographica Section A: Foundations of Crystallography 55 (3) (1999) 543–557. doi:10.1107/S0108767398015037.

[22] H. F. Poulsen, S. F. Nielsen, E. M. Lauridsen, S. Schmidt, R. M. Suter, U. Lienert, L. Margulies, T. Lorentzen, D. Juul Jensen, Three-dimensional maps of grain boundaries and the stress state of individual grains in polycrystals and powders, Journal of Applied Crystallography 34 (6) (2001) 751–756. doi:10.1107/S0021889801014273.

[23] J. Oddershede, S. Schmidt, H. F. Poulsen, H. O. Srensen, J. Wright, W. Reimers, Determining grain resolved stresses in polycrystalline materials using three-dimensional X-ray diffraction, Journal of Applied Crystallography 43 (3) (2010) 539–549. doi:10.1107/S0021889810012963.

[24] J. K. Edmiston, N. R. Barton, J. V. Bernier, G. C. Johnson, D. J. Steigmann, Precision of lattice strain and orientation measurements using high-energy monochromatic X-ray diffraction, Journal of Applied Crystallography (2011). doi:10.1107/S0021889811002123.

[25] J. K. Edmiston, J. V. Bernier, N. R. Barton, G. C. Johnson, Lattice refinement strategies, Acta Crystallographica Section A: Foundations of Crystallography (2012). doi:10.1107/S010876731105598X.

[26] A. Borbely, L. Renversade, P. Kenesei, J. Wright, On the calibration of high-energy X-ray diffraction setups. I. Assessing tilt and spatial distortion of the area detector, Journal of Applied Crystallography (2014). doi:10.1107/S160057671400898X.

[27] P. Sedmák, J. Pilch, L. Heller, J. Kopeček, J. Wright, P. Sedlák, M. Frost, P. Šittner, Grain-resolved analysis of localized deformation in nickel-titanium wire under tensile load, Science 353 (6299) (2016) 559–562. doi:10.1126/science.aad6700.

[28] P. Reischig, Determination of elastic strain tensors of individual grains in polycrystals by means of diffraction contrast tomography, MSc Graduation Report, Delft University of Technology, 2008.

[29] P. Reischig, A. King, L. Nervo, N. Viganó, Y. Guilhem, W. J. Palenstijn, K. J. Batenburg, M. Preuss, W. Ludwig, Advances in X-ray diffraction contrast tomography: Flexibility in the setup geometry and application to multiphase materials, Journal of Applied Crystallography 46 (2) (2013) 297–311. doi:10.1107/S0021889813002604.

[30] H. Proudhon, J. Li, P. Reischig, N. Guéninchault, S. Forest, W. Ludwig, Coupling Diffraction Contrast Tomography with the Finite Element Method, Advanced Engineering Materials 18 (6) (2016) 903–912. doi:10.1002/adem.201500414.
URL http://doi.wiley.com/10.1002/adem.201500414

[31] P. Reischig, W. Ludwig, Three-dimensional sub-grain mapping of elastic strain state and orientations in the bulk of polycrystals, Proceedings of the 40th Risø International Symposium on Materials Science (2019).

[32] B. C. Larson, W. Yang, G. E. Ice, J. D. Budai, J. Z. Tischler, Three-dimensional X-ray structural microscopy with submicrometre resolution, Nature 415 (6874) (2002) 887–890.
URL http://dx.doi.org/10.1038/415887a

[33] L. E. Levine, B. E. Larson, W. Yang, M. E. Kassner, J. Z. Tischler, D.-R. M.A., R. J. Fields, W. Liu, X-ray microbeam measurements of individual dislocation cell elastic strains in deformed single-crystal copper, Nature Materials 5 (2006) 619–622.

[34] O. Robach, J.-S. Micha, O. Ulrich, O. Geaymond, O. Sicardy, J. Härtwig, F. Rieutord, A tunable multicolour 'rainbow' filter for improved stress and dislocation density field mapping in polycrystals using X-ray Laue microdiffraction, Acta Crystallographica Section A Foundations of Crystallography 69 (2) (2013) 164–170. doi:10.1107/S0108767313000172.
URL http://scripts.iucr.org/cgi-bin/paper?S0108767313000172

[35] S. Tardif, A. Gassenq, K. Guilloy, N. Pauc, G. Osvaldo Dias, J. M. Hartmann, J. Widiez, T. Zabel, E. Marin, H. Sigg, J. Faist, A. Chelnokov, V. Reboud, V. Calvo, J. S. Micha, O. Robach, F. Rieutord, Lattice strain and tilt mapping in stressed Ge microstructures using X-ray Laue micro-diffraction and rainbow filtering, Journal of Applied Crystallography (2016). arXiv:1603.06370, doi:10.1107/S1600576716010347.

[36] J. Wright, ImageD11 (2017).
URL https://github.com/FABLE-3DXRD

[37] J. Hektor, S. A. Hall, N. A. Henningsson, J. Engqvist, M. Ristinmaa, F. Lenrick, J. P. Wright, Scanning 3DXRD measurement of grain growth, stress, and formation of Cu 6 Sn 5 around a tin whisker during heat treatment, Materials 12 (3) (2019) 1–16. doi:10.3390/ma12030446.

[38] Y. Hayashi, D. Setoyama, Y. Hirose, T. Yoshida, H. Kimura, Intragranular three-dimensional stress tensor fields in plastically deformed polycrystals., Science (New York, N.Y.) 366 (6472) (2019) 1492–1496. doi:10.1126/science.aax9167.
URL http://www.ncbi.nlm.nih.gov/pubmed/31857480

[39] H. Simons, A. King, W. Ludwig, C. Detlefs, W. Pantleon, S. Schmidt, F. Stöhr, I. Snigireva, A. Snigirev, H. F. Poulsen, Dark-field X-ray microscopy for multiscale structural characterization, Nature Communications 6 (2015). doi:10.1038/ncomms7098.

[40] H. F. Poulsen, A. C. Jakobsen, H. Simons, S. R. Ahl, P. K. Cook, C. Detlefs, X-ray diffraction microscopy based on refractive optics, Journal of Applied Crystallography 50 (5) (2017) 1441–1456. doi:10.1107/S1600576717011037.

[41] H. Simons, A. B. Haugen, A. C. Jakobsen, S. Schmidt, F. Stöhr, M. Majkut, C. Detlefs, J. E. Daniels, D. Damjanovic, H. F. Poulsen, Long-range symmetry breaking in embedded ferroelectrics, Nature Materials 17 (9) (2018) 814–819. doi:10.1038/s41563-018-0116-3.

[42] T. U. Schulli, S. J. Leake, X-ray nanobeam diffraction imaging of materials (2018). doi:10.1016/j.cossms.2018.09.003.

[43] M. C. Newton, S. J. Leake, R. Harder, I. K. Robinson, Three-dimensional imaging of strain in a single ZnO nanorod, Nature Materials 9 (2) (2010) 120–124. doi:10.1038/nmat2607.

[44] M. J. Cherukara, R. Pokharel, T. S. O'Leary, J. K. Baldwin, E. Maxey, W. Cha, J. Maser, R. J. Harder, S. J. Fensin, R. L. Sandberg, Three-dimensional X-ray diffraction imaging of dislocations in polycrystalline metals under tensile loading, Nature Communications 9 (1) (dec 2018). doi:10.1038/s41467-018-06166-5.

[45] F. Hofmann, N. W. Phillips, S. Das, P. Karamched, G. M. Hughes, J. O. Douglas, W. Cha, W. Liu, Nanoscale imaging of the full strain tensor of specific dislocations extracted from a bulk sample, Physical Review Materials 4 (1) (2020) 013801. arXiv:1903.04079, doi:10.1103/PhysRevMaterials.4.013801.
URL https://link.aps.org/doi/10.1103/PhysRevMaterials.4.013801

[46] H. F. Poulsen, An introduction to three-dimensional X-ray diffraction microscopy, Journal of Applied Crystallography 45 (6) (2012) 1084–1097. doi:10.1107/S0021889812039143.

[47] R. M. Suter, D. Hennessy, C. Xiao, U. Lienert, Forward modeling method for microstructure reconstruction using x-ray diffraction microscopy: Single-crystal verification, Review of Scientific Instruments 77 (12) (2006). doi:10.1063/1.2400017.

[48] S. F. Li, R. M. Suter, Adaptive reconstruction method for three-dimensional orientation imaging, Journal of Applied Crystallography (2013). doi:10.1107/S0021889813005268.

[49] L. Renversade, R. Quey, W. Ludwig, D. Menasche, S. Maddali, R. M. Suter, A. Borbély, Comparison between diffraction contrast tomography and high-energy diffraction microscopy on a slightly deformed aluminium alloy, IUCrJ 3 (1) (2016) 32–42. doi:10.1107/S2052252515019995.
URL http://scripts.iucr.org/cgi-bin/paper?S2052252515019995

[50] D. B. Menasche, P. A. Shade, R. M. Suter, Accuracy and precision of near-field high-energy diffraction microscopy forward-model-based microstructure reconstructions, Journal of Applied Crystallography 53 (1) (2020) 107–116. doi:10.1107/S1600576719016005.
URL http://scripts.iucr.org/cgi-bin/paper?S1600576719016005

[51] H. F. Poulsen, A six-dimensional approach to microtexture analysis, Philosophical Magazine 83 (24) (2003) 2761–2778. doi:10.1080/1478643031000147308.

[52] N. Viganò, W. Ludwig, K. J. Batenburg, Reconstruction of local orientation in grains using a discrete representation of orientation space, Journal of Applied Crystallography 47 (6) (2014) 1826–1840. doi:10.1107/S1600576714020147.

[53] N. Viganò, A. Tanguy, S. Hallais, A. Dimanov, M. Bornert, K. J. Batenburg, W. Ludwig, Three-dimensional full-field X-ray orientation microscopy, Scientific Reports 6 (February) (2016) 1–9. doi:10.1038/srep20618.
URL http://dx.doi.org/10.1038/srep20618

[54] N. Viganò, L. Nervo, L. Valzania, G. Singh, M. Preuss, K. J. Batenburg, W. Ludwig, A feasibility study of full-field X-ray orientation microscopy at the onset of deformation twinning, Journal of Applied Crystallography 49 (2) (2016) 544–555. doi:10.1107/S1600576716002302.
URL http://scripts.iucr.org/cgi-bin/paper?S1600576716002302

[55] N. Viganò, W. Ludwig, Advances in 6d diffraction contrast tomography, in: Journal of Instrumentation, 2018. doi:10.1088/1748-0221/13/04/C04017.

[56] D. Hänschke, L. Helfen, V. Altapova, A. Danilewsky, T. Baumbach, Three-dimensional imaging of dislocations by X-ray diffraction laminography, Applied Physics Letters 101 (24) (2012). doi:10.1063/1.4769988.

[57] Z. J. Li, A. N. Danilewsky, L. Helfen, P. Mikulik, D. Haenschke, J. Wittge, D. Allen, P. McNally, T. Baumbach, Local strain and defects in silicon wafers due to nanoindentation revealed by full-field X-ray microdiffraction imaging, Journal of Synchrotron Radiation 22 (4) (2015) 1083–1090. doi:10.1107/S1600577515009650.

[58] A. King, P. Reischig, J. Adrien, W. Ludwig, First laboratory X-ray diffraction contrast tomography for grain mapping of polycrystals, Journal of Applied Crystallography 46 (6) (2013) 1734–1740. doi:10.1107/S0021889813022553.
URL http://scripts.iucr.org/cgi-bin/paper?S0021889813022553

[59] S. A. McDonald, P. Reischig, C. Holzner, E. M. Lauridsen, P. J. Withers, A. P. Merkle, M. Feser, Non-destructive mapping of grain orientations in 3D by laboratory X-ray microscopy, Scientific Reports (2015). doi:10.1038/srep14665.

[60] J. Sun, C. Holzner, H. Bale, M. Tomita, N. Gueninchault, F. Bachmann, E. Lauridsen, T. Inaguma, M. Kimura, 3D Crystal Orientation Mapping of Recrystallization in Severely Cold-rolled Pure Iron Using Laboratory Diffraction Contrast Tomography, ISIJ International (2019). doi:10.2355/isijinternational.isijint-2019-405.

[61] F. Bachmann, H. Bale, N. Gueninchault, C. Holzner, E. M. Lauridsen, 3D grain reconstruction from laboratory diffraction contrast tomography, Journal of Applied Crystallography 52 (3) (2019) 643–651. doi:10.1107/S1600576719005442.

[62] B. E. Warren, X-Ray Diffraction, Dover Publications, New York, 1990.

[63] A. V. der Sluis, H. V. der Vorst, SIRT-and CG-type methods for the iterative solution of sparse linear least-squares problems (1990).
URL http://www.sciencedirect.com/science/article/pii/002437959090215X

[64] J. Gregor, J. A. Fessler, Comparison of SIRT and SQS for Regularized Weighted Least Squares Image Reconstruction, IEEE Transactions on Computational Imaging 1 (1) (2015) 44–55. doi:10.1109/tci.2015.2442511.

[65] W. Ludwig, P. Reischig, A. King, M. Herbig, E. M. Lauridsen, T. J. Marrow, J. Y. Buffière, Three-dimensional Grain Mapping by X-ray Diffraction Contrast Tomography and the Use of Friedel Pairs in Diffraction Data Analysis, Rev Scient Inst 2009 80 (2009) 33905.

[66] K. J. Batenburg, J. Sijbers, H. F. Poulsen, E. Knudsen, DART: a robust algorithm for fast reconstruction of three-dimensional grain maps, Journal of Applied Crystallography 43 (6) (2010) 1464–1473. doi:10.1107/S0021889810034114.
URL http://scripts.iucr.org/cgi-bin/paper?S0021889810034114

[67] P. C. Hansen, H. O. Sørensen, Z. Sükösd, H. F. Poulsen, Reconstruction of single-grain orientation distribution functions for crystalline materials, SIAM Journal on Imaging Sciences

2 (2) (2009) 593–613. doi:10.1137/080726021.
URL http://epubs.siam.org/doi/abs/10.1137/080726021

[68] A. Chambolle, T. Pock, A first-order primal-dual algorithm for convex problems with applications to imaging, Journal of Mathematical Imaging and Vision 40 (1) (2011) 120–145. doi:10.1007/s10851-010-0251-1.

[69] E. Y. Sidky, J. H. Jorgensen, X. Pan, Convex optimization problem prototyping for image reconstruction in computed tomography with the ChambollePock algorithm, Physics in Medicine and Biology 57 (10) (2012) 3065–3091. arXiv:1111.5632, doi:10.1088/0031-9155/57/10/3065.

[70] A. C. Kak, M. Slaney, Principles of Computerized Tomographic Imaging, Society for Industrial and Applied Mathematics, 2001. doi:10.1137/1.9780898719277.
URL http://epubs.siam.org/doi/book/10.1137/1.9780898719277

[71] H. Der Sarkissian, N. Viganó, K. J. Batenburg, A Data Consistent Variational Segmentation Approach Suitable for Real-time Tomography, Fundamenta Informaticae 163 (1) (2018) 1–20. doi:10.3233/FI-2018-1729.

[72] G. Johnson, A. King, M. G. Honnicke, J. Marrow, W. Ludwig, X-ray diffraction contrast tomography: a novel technique for three-dimensional grain mapping of polycrystals. II. The combined case, Journal of Applied Crystallography 41 (2) (2008) 310–318. doi:10.1107/S0021889808001726.
URL http://scripts.iucr.org/cgi-bin/paper?S0021889808001726

[73] W. Ludwig, S. Schmidt, E. M. Lauridsen, H. F. Poulsen, X-ray diffraction contrast tomography: A novel technique for three-dimensional grain mapping of polycrystals. I. Direct beam case, Journal of Applied Crystallography 41 (2) (2008) 302–309. doi:10.1107/S0021889808001684.

[74] A. Ben-Israel, T. N. Greville, Generalized Inverses, 2nd Edition, Springer, New York, 2003. doi:10.1007/b97366.

[75] R. A. Lebensohn, N-site modeling of a 3D viscoplastic polycrystal using Fast Fourier Transform, Acta Materialia 49 (14) (2001) 2723–2737. doi:10.1016/S1359-6454(01)00172-0.
URL https://linkinghub.elsevier.com/retrieve/pii/S1359645401001720

[76] I. G. Kazantsev, S. Schmidt, H. F. Poulsen, A discrete spherical x-ray transform of orientation distribution functions using bounding cubes, Inverse Problems 25 (10) (2009). doi:10.1088/0266-5611/25/10/105009.

[77] Y. Kamimura, S. Katakura, K. Edagawa, S. Takeuchi, S. Kuramoto, T. Furuta, Basic Deformation Mechanism of Bcc Titanium-Based Alloy of Gum Metal, MATERIALS TRANSACTIONS 57 (9) (2016) 1526–1534. doi:10.2320/matertrans.M2016191.
URL https://www.jstage.jst.go.jp/article/matertrans/57/9/57{_}M2016191/{_}article

[78] T. Furuta, S. Kuramoto, J. W. Morris, N. Nagasako, E. Withey, D. C. Chrzan, The mechanism of strength and deformation in Gum Metal, Scripta Materialia 68 (10) (2013) 767–772. doi:10.1016/j.scriptamat.2013.01.027.
URL http://dx.doi.org/10.1016/j.scriptamat.2013.01.027

[79] R. Talling, R. Dashwood, M. Jackson, D. Dye, On the mechanism of superelasticity in Gum metal, Acta Materialia 57 (4) (2009) 1188–1198. doi:10.1016/j.actamat.2008.11.013.
URL http://dx.doi.org/10.1016/j.actamat.2008.11.013https://linkinghub.elsevier.com/retrieve/pii/S1359645408008082

[80] M. Hara, Y. Shimizu, T. Yano, N. Takesue, T. Furuta, S. Kuramoto, Mechanical anisotropy and ideal strength in a multifunctional Ti-Nb-Ta-Zr-O alloy (Gum Metal), International Journal of Materials Research 100 (3) (2009) 345–348.

[81] R. J. Talling, R. J. Dashwood, M. Jackson, S. Kuramoto, D. Dye, Determination of (C11 - C12) in Ti-36Nb-2Ta-3Zr-0.3O (wt.%) (Gum metal), Scripta Materialia 59 (6) (2008) 669–672. doi:10.1016/j.scriptamat.2008.05.022.

[82] N. Gueninchault, H. Proudhon, W. Ludwig, Nanox: a miniature mechanical stress rig designed for near-field X-ray diffraction imaging techniques, Journal of Synchrotron Radiation 23 (6) (2016) 1474–1483. doi:10.1107/S1600577516013850.
URL http://scripts.iucr.org/cgi-bin/paper?S1600577516013850

[83] G. B. M. Vaughan, J. P. Wright, A. Bytchkov, M. Rossat, H. Gleyzolle, I. Snigireva, A. Snigirev, X-ray transfocators: Focusing devices based on compound refractive lenses, Journal of Synchrotron Radiation 18 (2) (2011) 125–133. doi:10.1107/S0909049510044365.

[84] A. F. Siegel, Robust regression using repeated medians, Biometrika 69 (1) (1982) 242–244. doi:10.1093/biomet/69.1.242.

[85] N. Takesue, Y. Shimizu, T. Yano, M. Hara, S. Kuramoto, Single-crystal growth of Ti-Nb-Ta-Zr-O alloys and measurement of elastic properties, Journal of Crystal Growth 311 (12) (2009) 3319–3324. doi:10.1016/j.jcrysgro.2009.03.052.

[86] S. Annett, S. Morelhao, D. Dale, S. Kycia, Novel near field detector for three-dimensional X-ray diffraction microscopy, in: MRS Advances, Vol. 3, Materials Research Society, 2018, pp. 2341–2346. doi:10.1557/adv.2018.487.

[87] W. Ludwig, P. Reischig, A. King, M. Herbig, H. Proudhon, S. Rutishauser, C. David, Thoughts about the optimum data acquisition geometry and time resolution of monochromatic beam X-ray diffraction microscopy experiments, in: 31st Ris{ø} International Symposium on Materials Science: Challenges in materials science and possibilities in 3D and 4D characterization techniques, Vol. 31, 2010.

[88] W. Ludwig, E. M. Lauridsen, S. Schmidt, H. F. Poulsen, J. Baruchel, High-resolution three-dimensional mapping of individual grains in polycrystals by topotomography, Journal of Applied Crystallography 40 (5) (2007) 905–911. doi:10.1107/S002188980703035X.

[89] M. Moscicki, P. Kenesei, J. Wright, H. Pinto, T. Lippmann, A. Borbély, A. Pyzalla, Friedel-pair based indexing method for characterization of single grains with hard X-rays, Materials Science and Engineering: A 524 (1-2) (2009) 64–68. doi:10.1016/j.msea.2009.05.002. URL https://linkinghub.elsevier.com/retrieve/pii/S0921509309005760

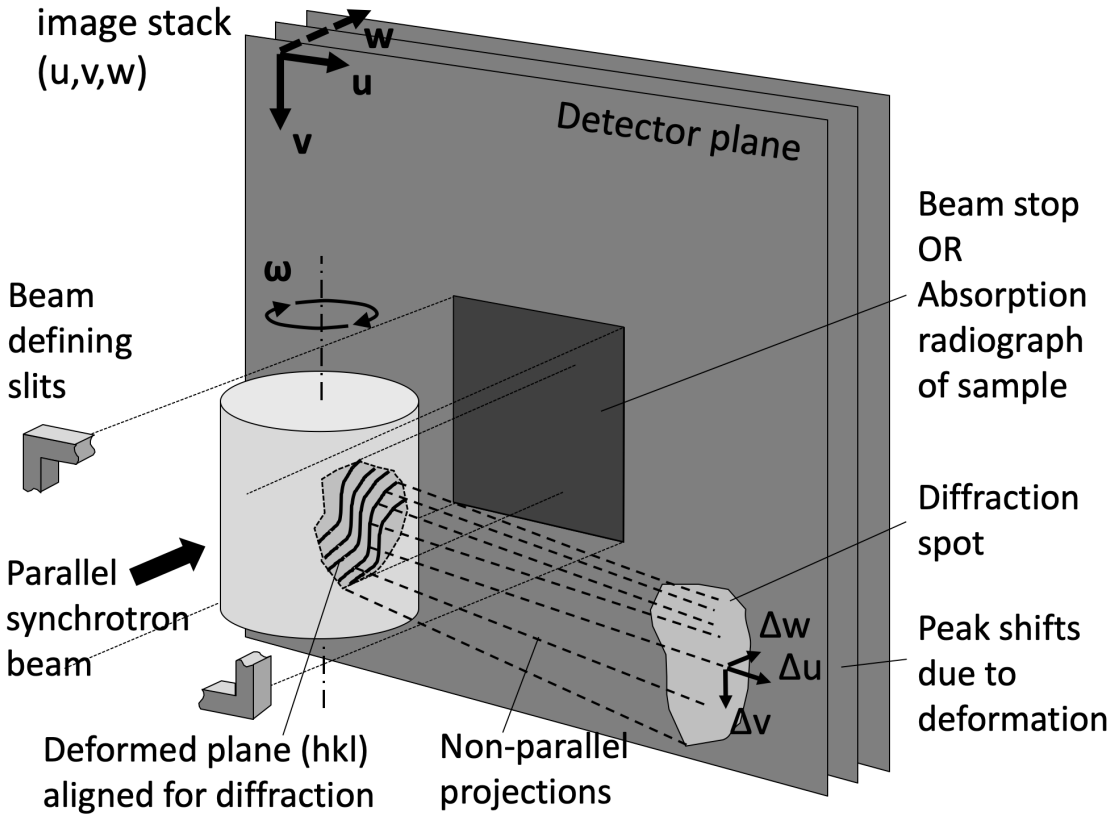

Figure 1: Diffraction Contrast Tomography (DCT) setup. The beamstop is removable to record the absorption radiographs in the direct beam that are used in a tomographic reconstruction.

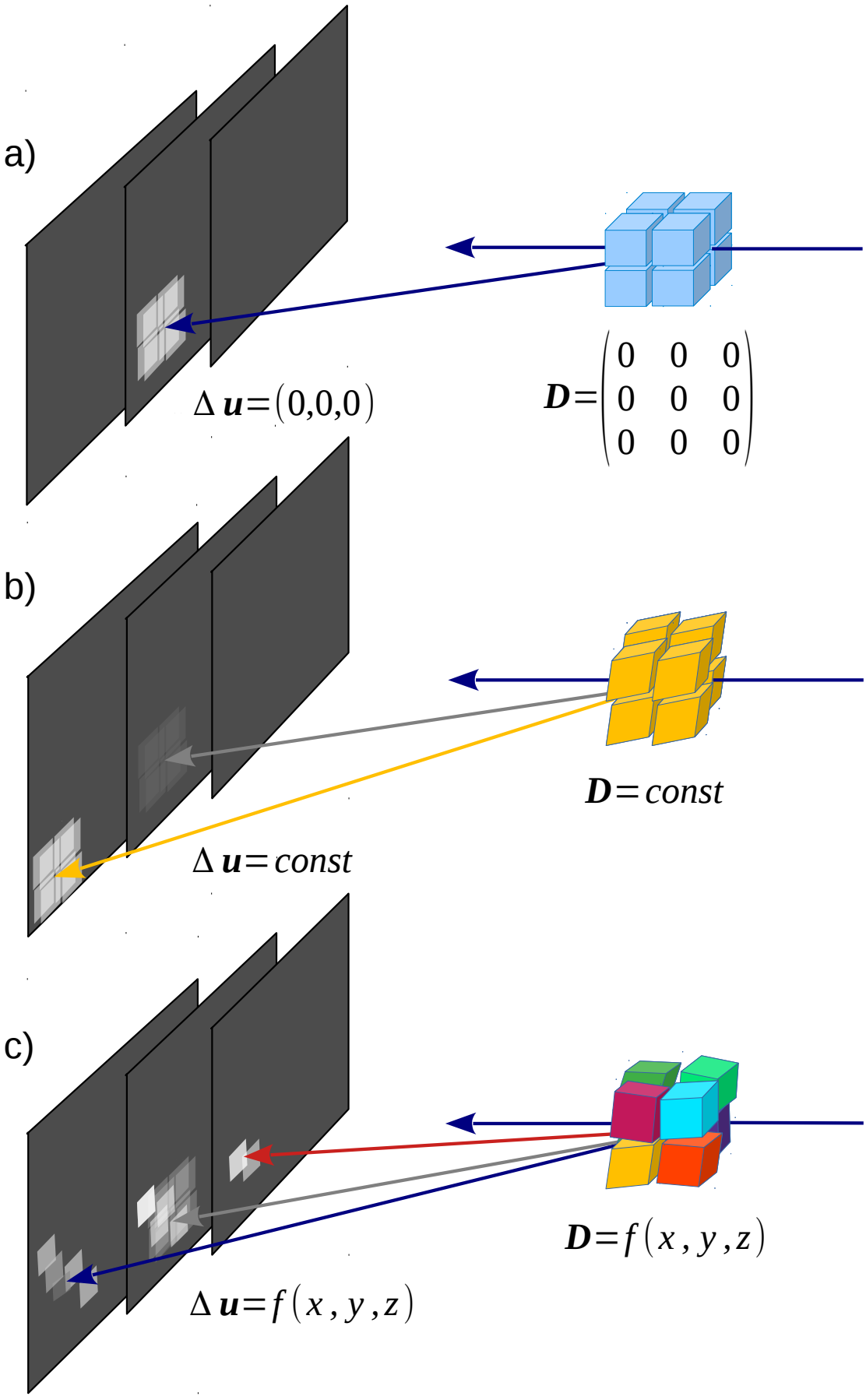

Figure 2: Schematic representation of the effect of the local deformation state on the projection geometry. (a) Zero deformation. (b) Uniform deformation state. (c) Non-uniform deformation distribution.

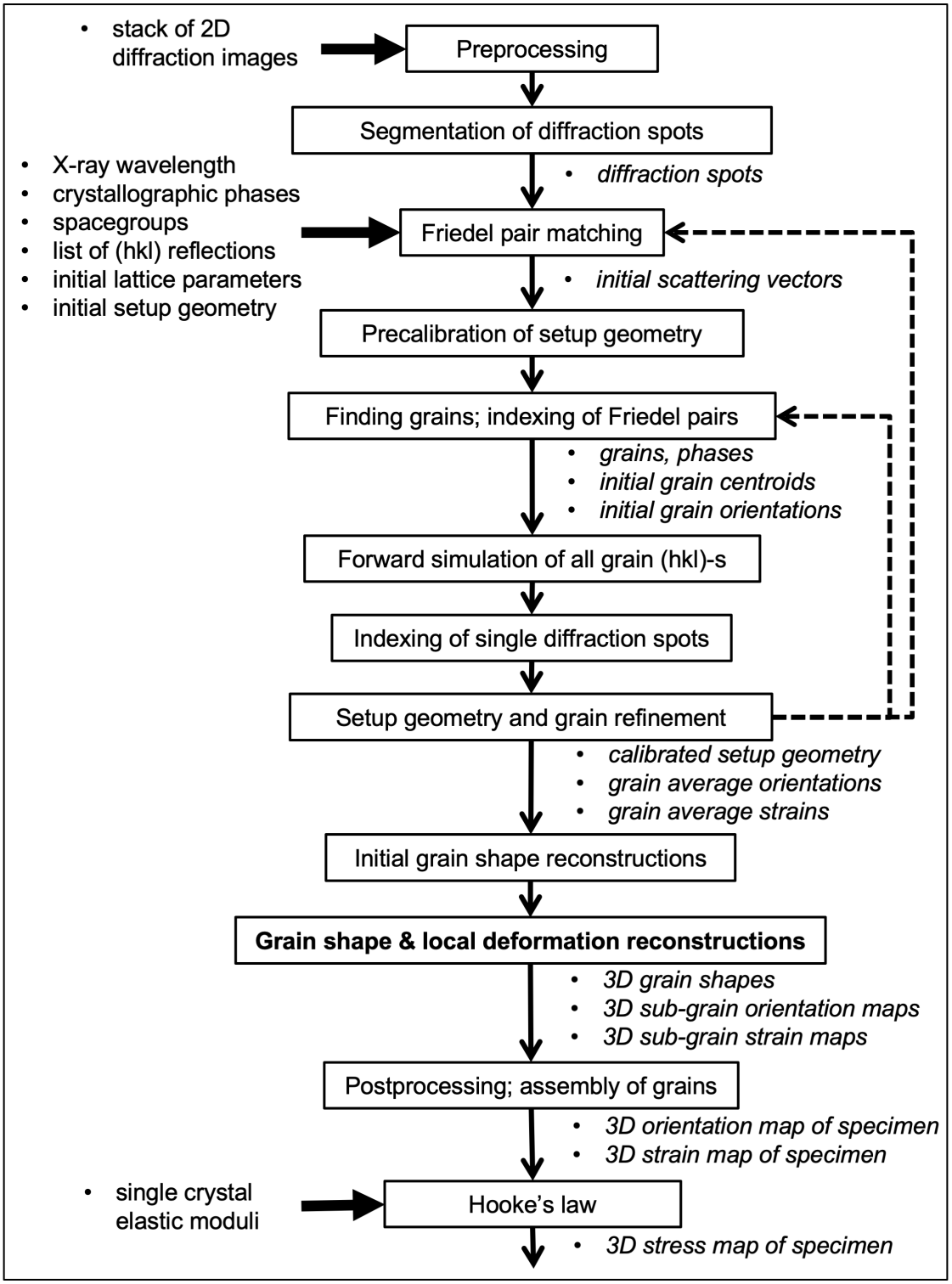

Figure 3: Flow chart of the complete DCT processing including deformation reconstruction by the Iterative Tensor Field solver.

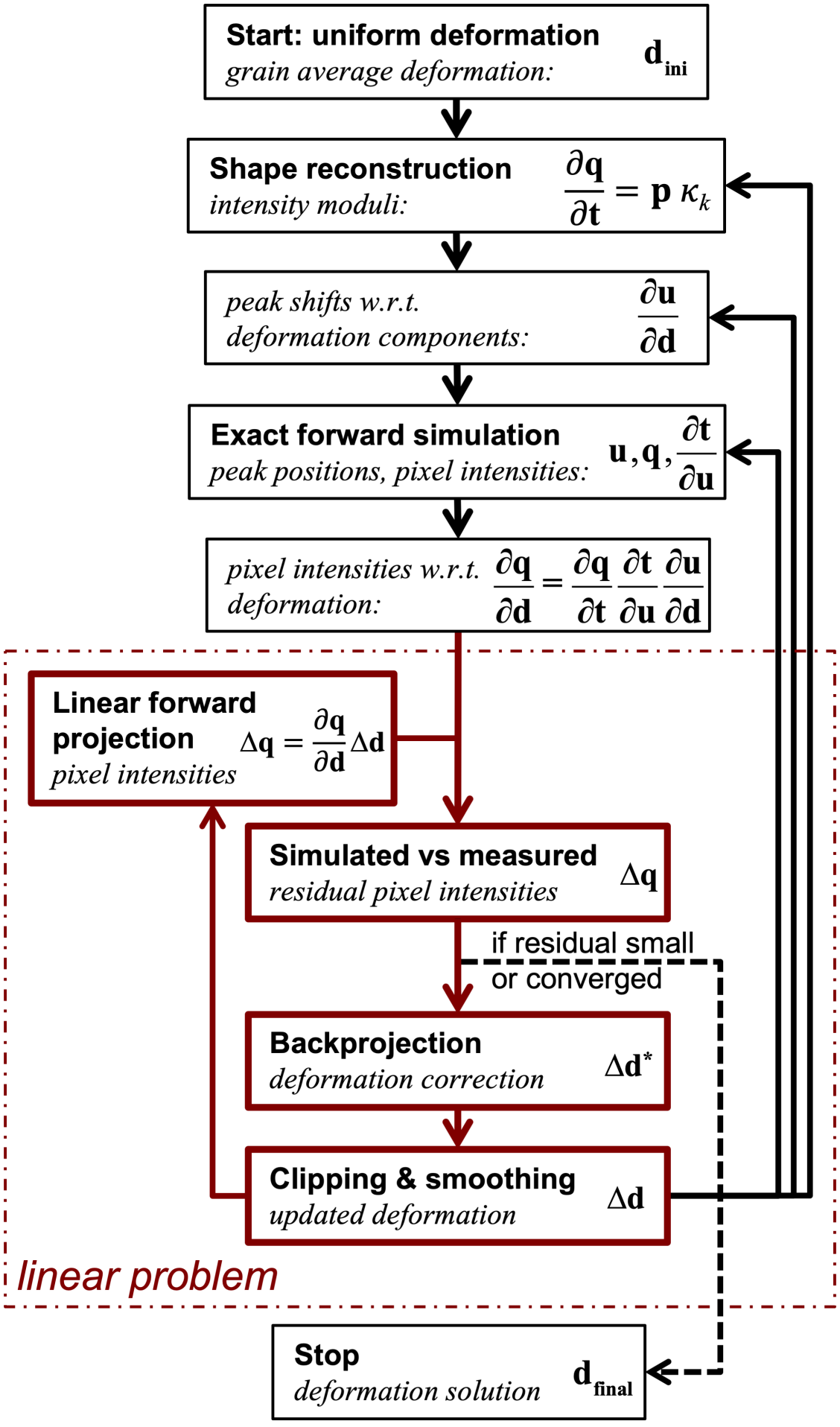

Figure 4: Flow chart of the Iterative Tensor Field (ITF) reconstruction algorithm.

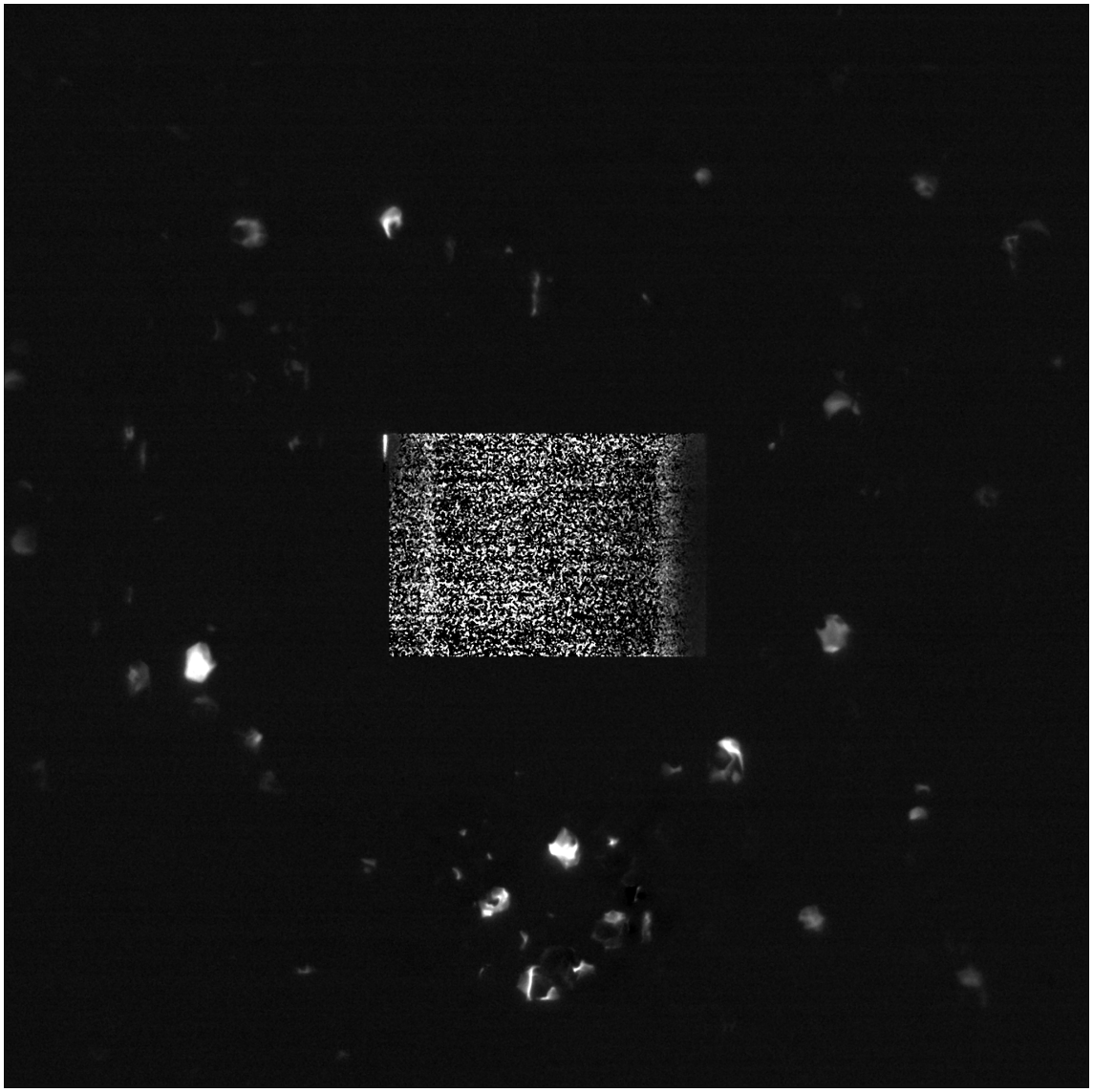

Figure 5: Example of a preprocessed detector image showing the diffraction signal in the dark field area in the high load data set (2048×2048 pixels or 2.87×2.87 mm^2 effective area).

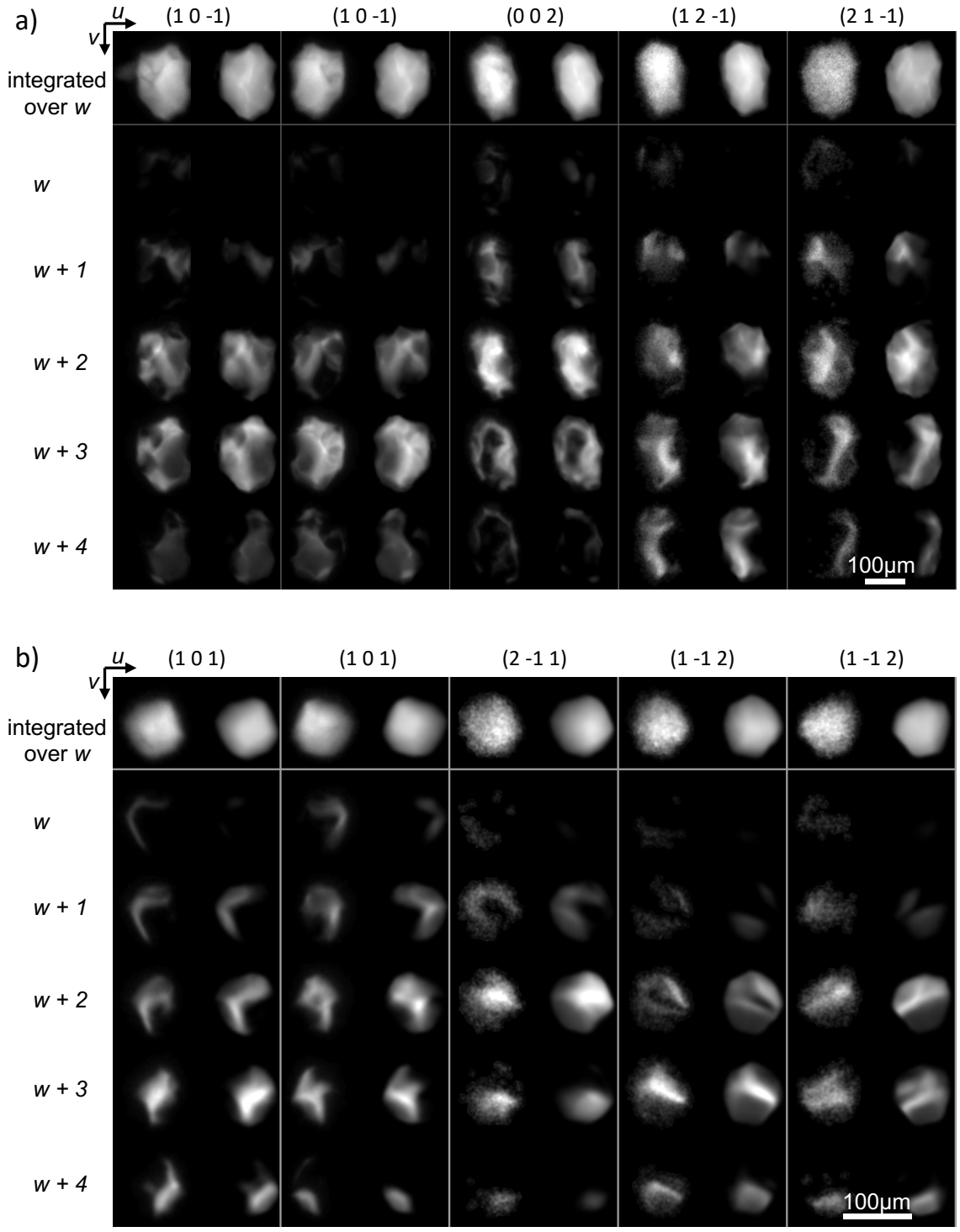

Figure 6: Five examples of segmented 3D diffraction spots showing the intensity distribution in (u, v, w) in the high load data set. Measured (left columns) and simulated equivalents at the solution (right columns) across consecutive w images, and the resulting 2D diffraction spots integrated in w are shown. The intensity "tails" extend beyond the w ranges shown here. (a) Grain #1 (the largest detected grain, mean L1 error 0.316). (b) Grain #269 (mean L1 error 0.364).

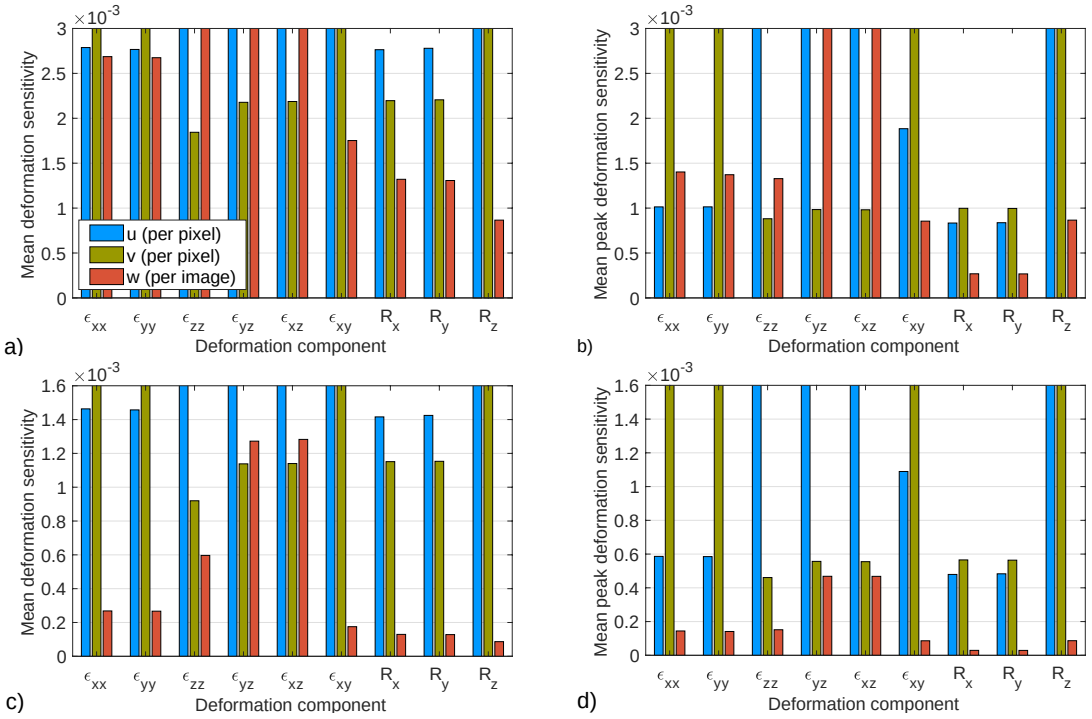

Figure 7: Mean deformation sensitivity of all grains in the high load data set, w.r.t. strain tensor and Rodrigues vector components in the sample reference frame. (a) Mean sensitivity χ in the experimental setup used. (b) Mean peak sensitivity χ^+ in the experimental setup used. (c) Mean sensitivity χ in an optimised experimental setup. (d) Mean peak sensitivity χ^+ in an optimised experimental setup. Values are clipped at the top of the plots.

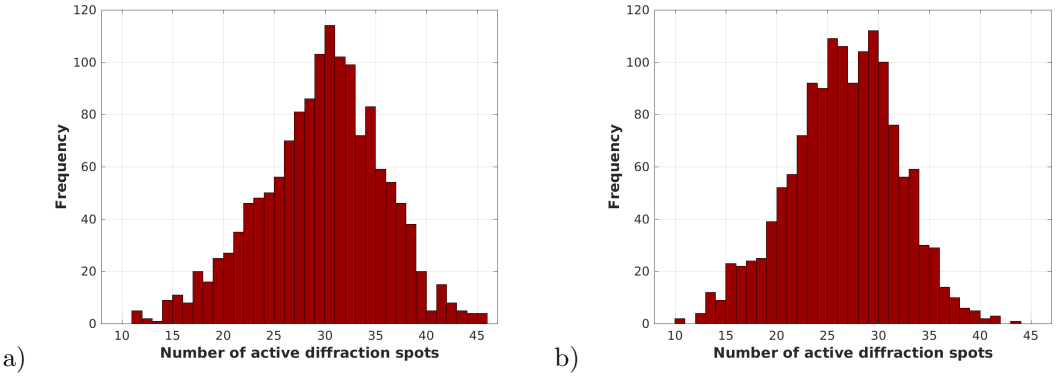

Figure 8: Number of active diffraction spots used for the reconstruction per grain in the low load data set (a) and in the high load data set (b).

a)

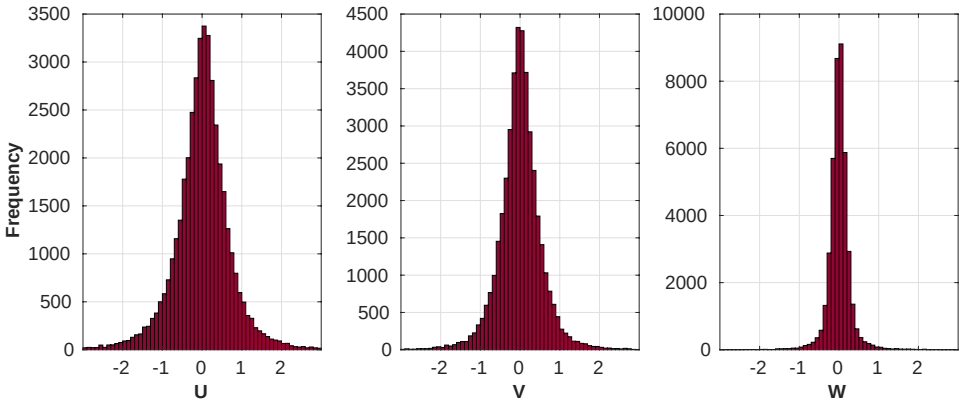

b)

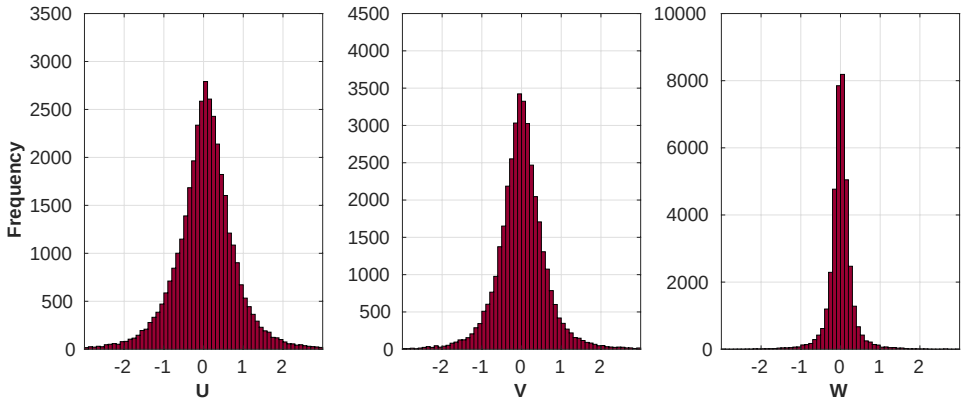

Figure 9: Histograms of discrepancies between the measured and simulated diffraction spot centroid positions in the low load data set (a) and in the high load data set (b).

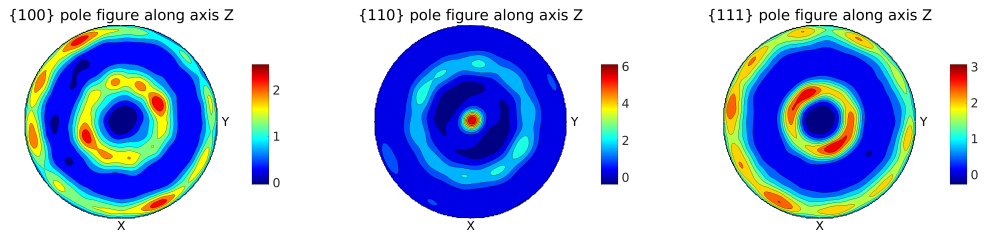

Figure 10: Pole figures of the Gum Metal specimen along the rotation (and tensile loading) axis as created from the indexed reflections in the low load data set.

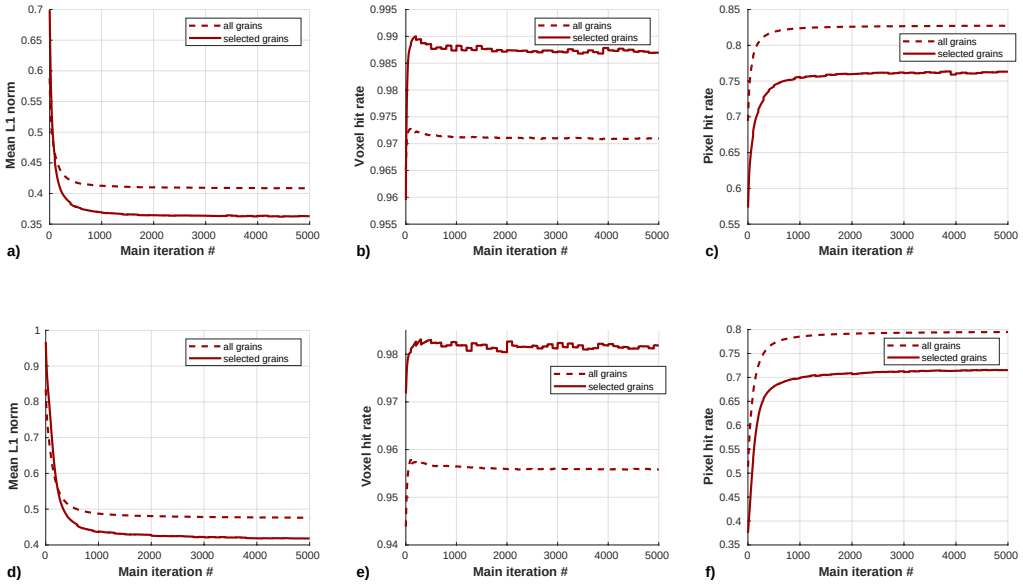

Figure 11: Convergence plots of error metrics combining the active diffraction spots of all grains, and of a selected set of grains with a mean L1 norm under the threshold. Mean L1 norm of the pixel intensity errors normalised with the total diffraction spot intensities in the low load (a) and high load (d) data set. Voxel hit rate at low load (b), and at high load (e). Pixel hit rate at low load (c), and at high load (f).

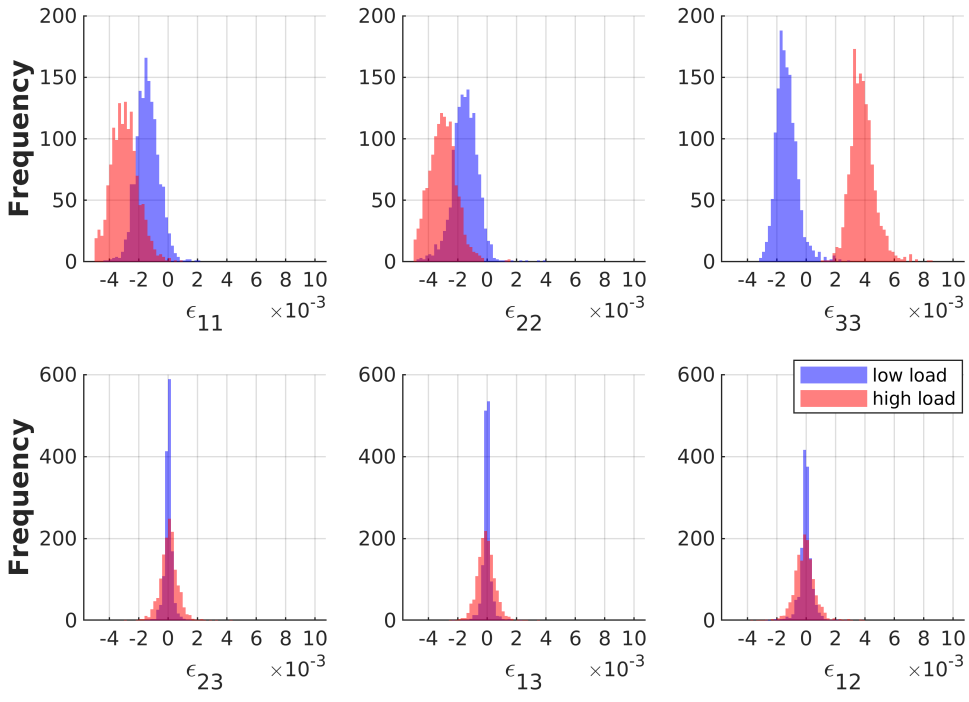

Figure 12: Histograms of the grain average strain tensor components in the sample reference frame, obtained by robust median fitting before hydrostatic strain correction.

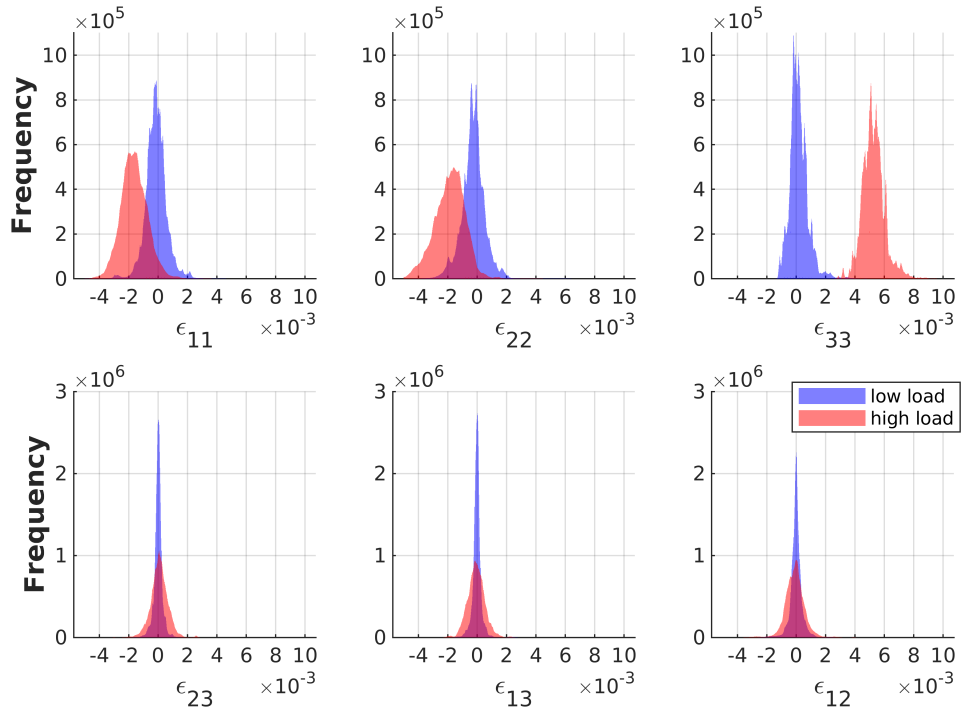

Figure 13: Histograms of the strain tensor components of all grain voxels in the grain map, in the sample reference frame after hydrostatic strain correction.

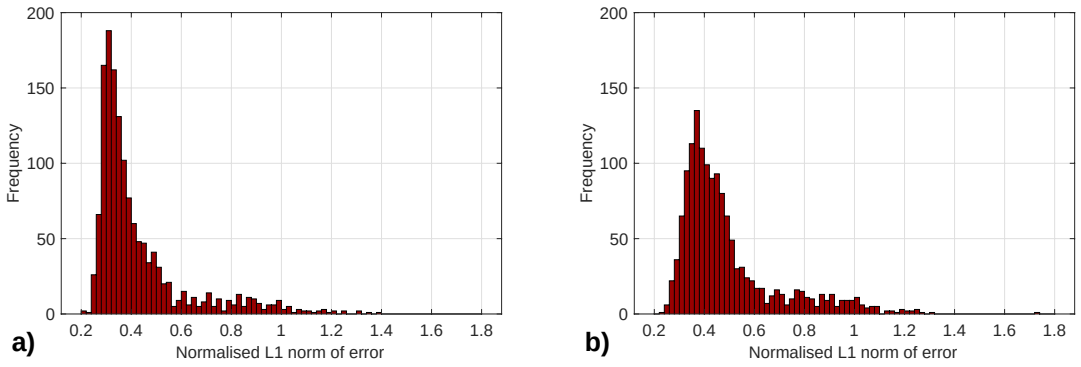

Figure 14: Histograms of the mean L1 norm of the pixel intensity errors normalised with the total diffraction spot intensities for each grain, in the low load (a) and high load (b) data set.

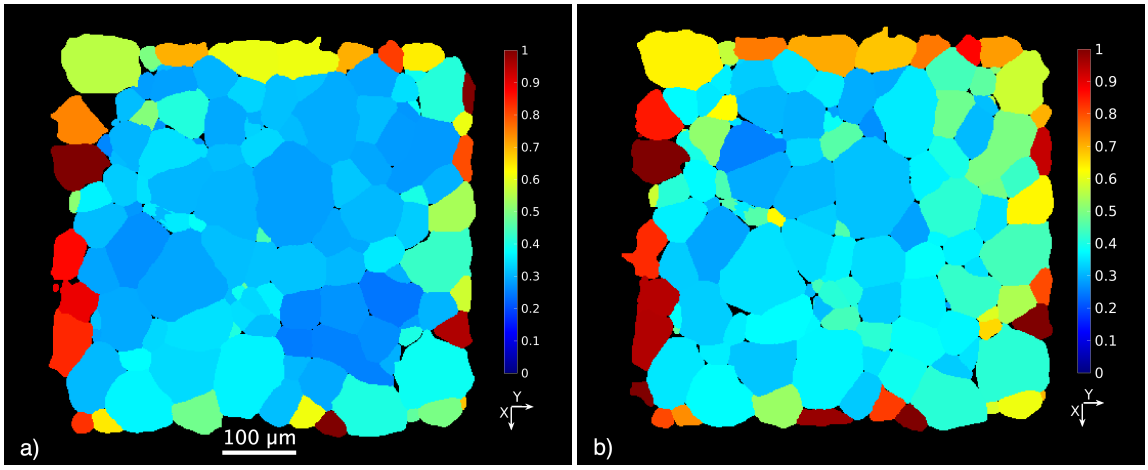

Figure 15: Mean L1 norm of the pixel intensity errors normalised with the total diffraction spot intensities for each grain in a X-Y section at low load (a) and at high load (b).

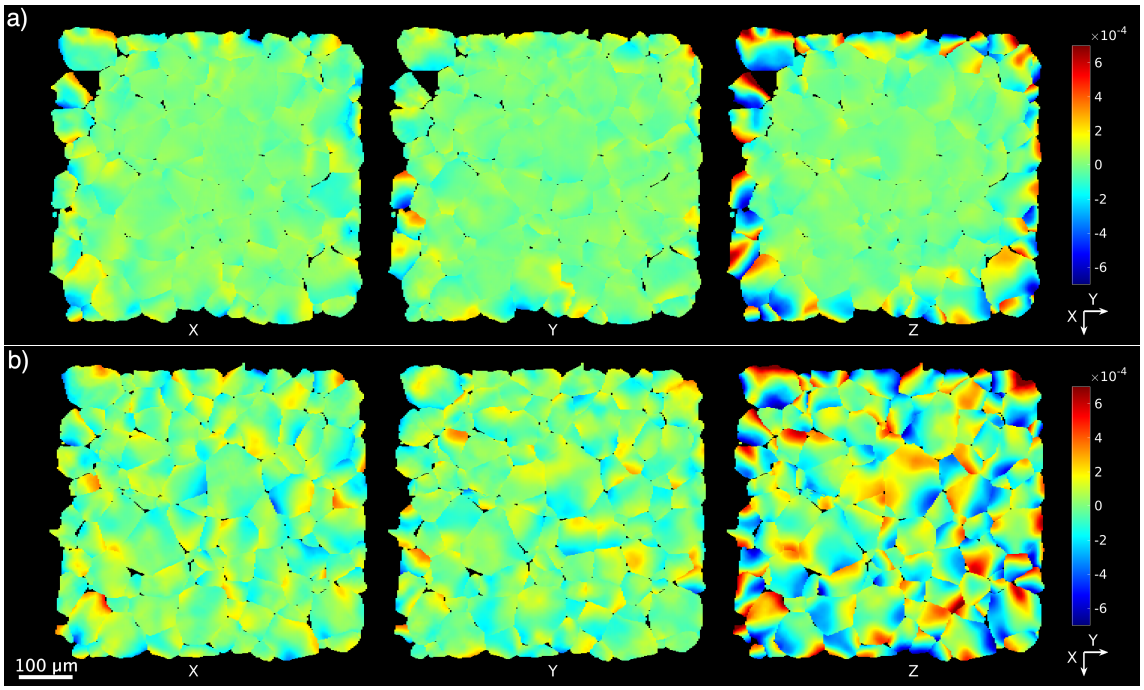

Figure 16: Rodrigues vector components of the orientation deviation from the grain mean in the sample reference frame in a X-Y section, at low load (a) and at high load (b).

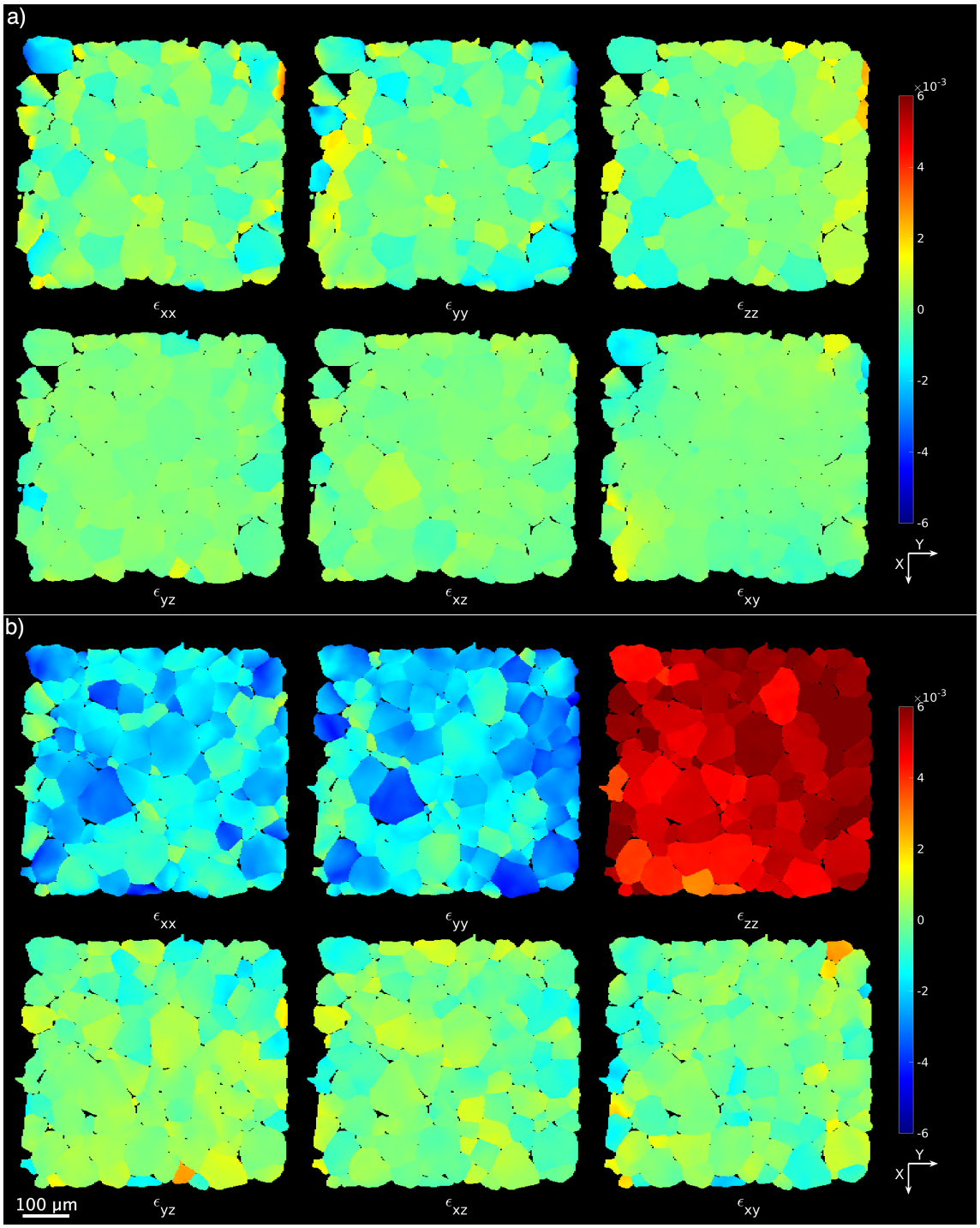

Figure 17: Lattice strain tensor components in the sample reference frame in a X-Y section at low load (a) and at high load (b).

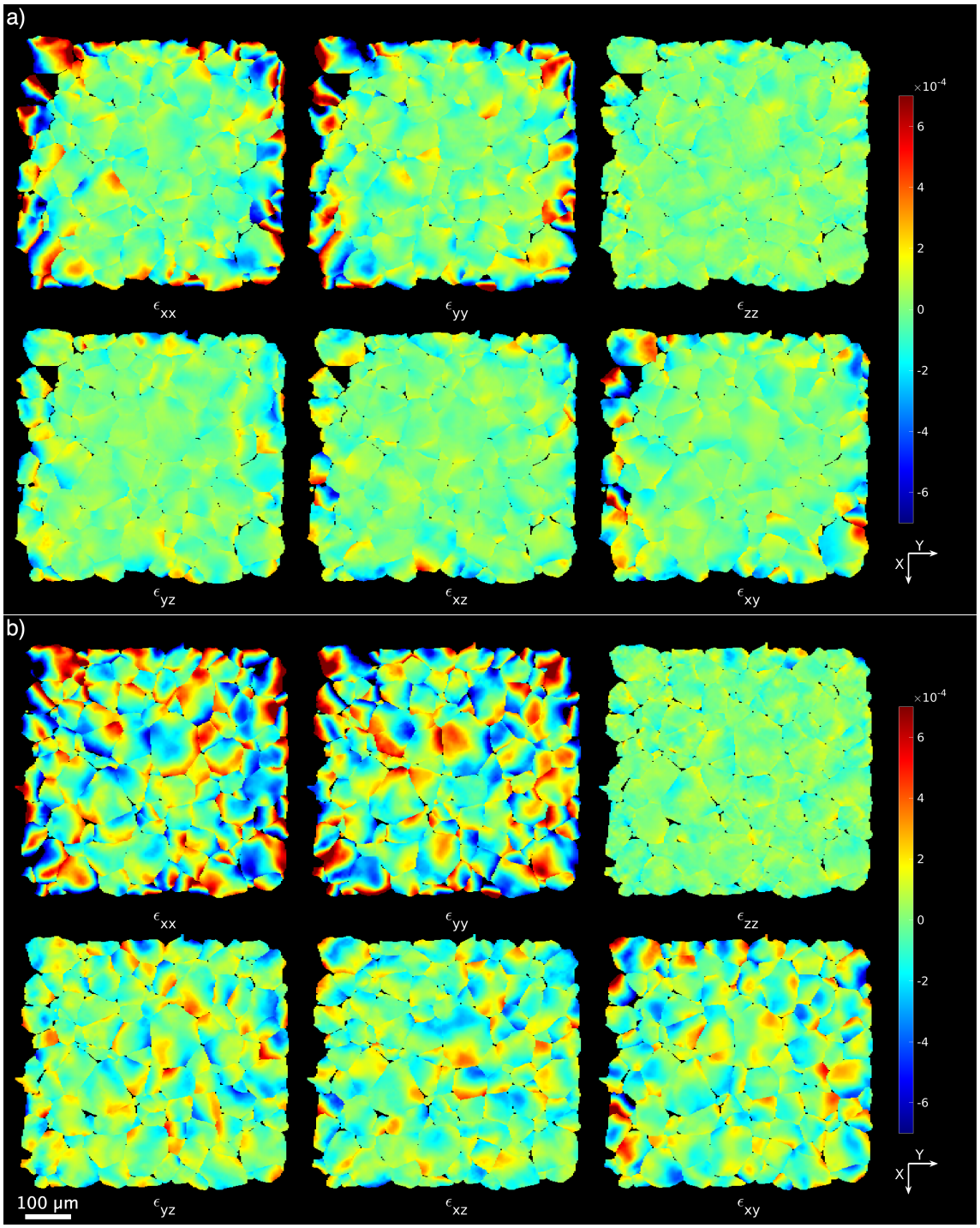

Figure 18: Deviation of lattice strain tensor components from the grain mean in the sample reference frame in a X-Y section, at low load (a) and at high load (b).

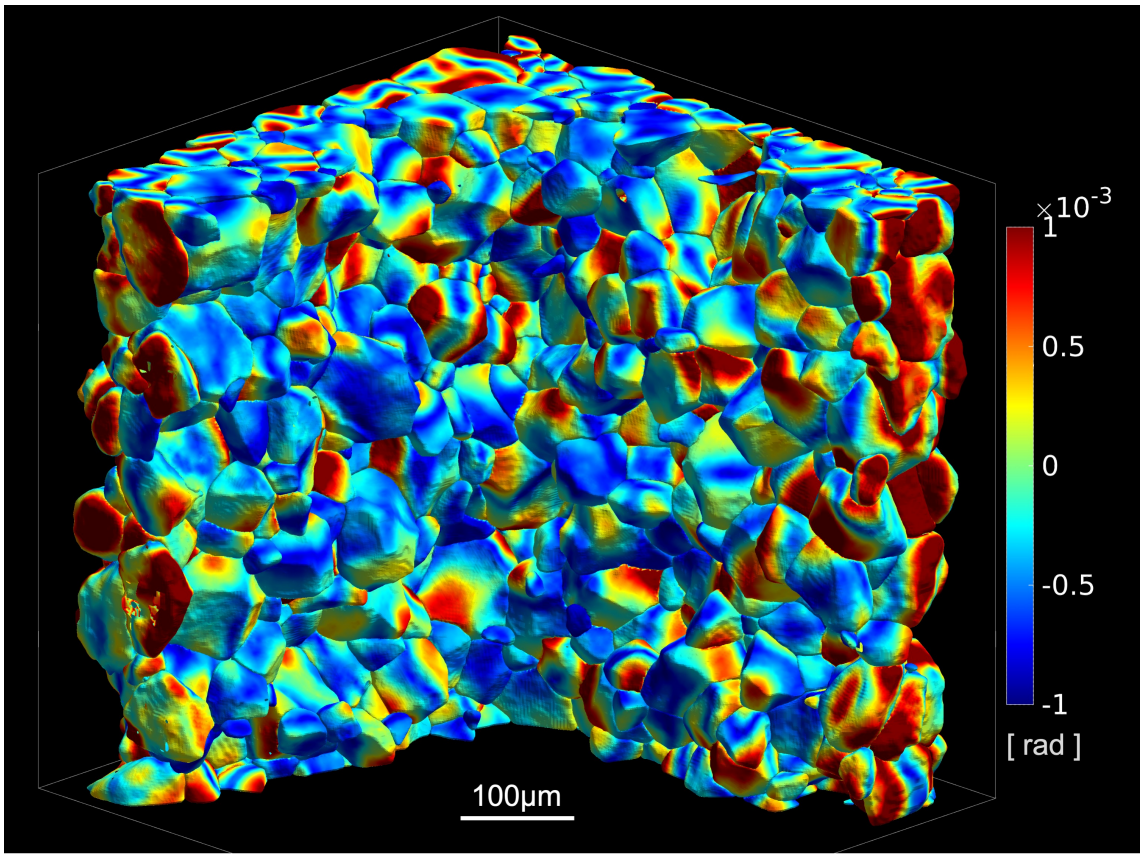

Figure 19: 3D rendering of the local misorientation angle from the grain mean orientation at high load. The front section was rendered transparent to show grains in the bulk.

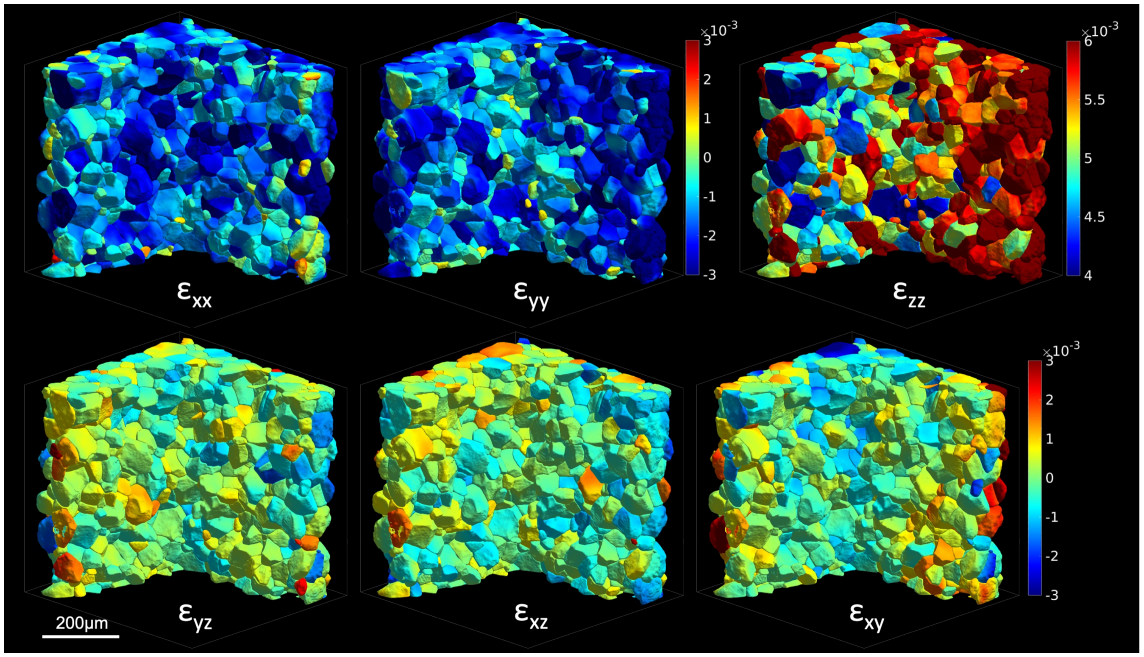

Figure 20: 3D rendering of the local strain tensor components in the sample reference frame at high load. The front section was rendered transparent to show grains in the bulk.

Algorithm	Representation			Mapped dimensions	Memory need per voxel (bit) *	Total memory need (GB)	
	Diffracting power	Orientation	Strain			32^3 voxels	512^3 voxels
6D solver	solution	3D discrete	-	6D discrete to scalar	$16^3 \times 32\text{bit} = 1.3 \times 10^5$	0.54	2200
12D solver (theoretical)	solution	3D discrete	6D discrete	12D discrete to scalar	$16^9 \times 32\text{bit} = 2.2 \times 10^{12}$	9×10^6	3.7×10^{10}
ITF-DCT	1D	3D	6D	3D discrete to 10D	$10 \times 32\text{bit} = 320$	0.001	5.4

Figure 21: TABLE 1. Representation of deformation in a 3D volume and the corresponding memory requirements (data storage for the solution only, excluding processing). () For comparing the discrete representation, the number of distinct orientation or strain values was assumed to be 16.

Incident beam profile	Irradiated volume	Detector	Beam chromaticity	Axes scanned for 3D map	Dimensions of solution		
					Real space	Orientation	Strain
Pencil beam	1D line	far-field	polychromatic	3 translations (+1 energy)	0	3	5 (6)
Pencil beam	1D line	far-field	monochromatic	2 translations + 1 rotation	0 / 2	3	6
Line beam	2D section	near-field	monochromatic	1 translation +1 rotation	2	3	6
Box beam	3D volume	near-field	monochromatic	1 rotation	3	3	6

Figure 22: TABLE 2. Acquisition modes for reconstruction of deformation fields in a 3D sample volume.

		Low load	High load
Average tensile stress from load cell		~34 MPa	~345 MPa
Reconstructed volume size in (x,y,z)		410 × 440 × 406 voxels	
No. of grains analysed for deformation		1428	1437
No. of diffraction spots analysed per grain		11 … 47	10 ... 43
Mean no. of diffraction spots analysed per grain		29	26
Standard deviation of error between measured and simulated diffraction spot centroids	u:	0.731 pixel	0.813 pixel
	v:	0.577 pixel	0.668 pixel
	w:	0.303 image	0.350 image

Figure 23: TABLE 3. Results of the indexing, shape reconstruction and fitting of grain average properties.